Spin quantum dynamics in hybrid circuits

Matthieu Delbecq

Mémoire pour l'habilitation à diriger des recherches

Spin quantum dynamics in hybrid circuits

Matthieu Delbecq

Soutenue le 26 Juin 2020 devant le jury composé de

Hélène Bouchiat	Université d'Orsay	Rapporteur
Silvano DeFranceschi	CEA	Examinateur
Jelena Klinovaja	Basel University	Rapporteur
Dimitri Roditchev	ESPCI	Examinateur
Gary Steele	TU Delft	Rapporteur
Valia Voliotis	Sorbonne Université	Présidente du jury

Sorbonne Université

Contents

Introduction

This manuscript presents the research activity I have conducted during the last seven years. Since my PhD my research activity focused either directly or indirectly on the manipulation the electron spin. The spin of the electron (and other particles) is a purely quantum mechanical property arising in the Dirac equation for relativistic particles which Pauli extended to non-relativistic quantum theory. By isolating a spin 1/2, it is possible to realize close to a true and ideal two-level system which is the simplest quantum system to manipulate and investigate. It is probably the reason why historically many experimental observations of the spin where made before the theory was drawn, including the seminal Stern-Gerlach experiment. Addressed by the magnetic field, ensembles of electron and atom spins were exploited as a powerful resource to characterize and explore condensed matter, with nuclear magnetic resonance (NMR) and electron spin resonance (ESR). The former lead to one of the key technologies of the now called *first quantum revolution*, namely magnetic resonance imaging (MRI).

With the advent of sophisticated micro-fabrication techniques in research laboratories in the 80's, coming from the semiconductor industry, the field of mesoscopic physics could emerge. It made it possible to isolate and manipulate quantum phenomena and single quantum excitations in macroscopic size circuits (to be understood as circuits containing a huge number of atoms, comparable to condensed matter systems and to be compared to atomic physics). It was quickly realized that the quantum two-level system –which by essence is the definition of a qubit– formed by a single electron spin isolated in a quantum dot could be an ideal system to manipulate quantum information. Any quantum system encodes *quantum* information but spins are particularly simple systems to address and manipulate. Beyond being individually used as qubits, the spin texturing of electrons in conductors can lead, in particular in low dimensional systems, to exotic states of matter which can also encode quantum information, topologically protected from decoherence. To isolate individual spins or to shape the spin texture of electrons in low dimensional conductors, one needs to exploit the combination of various materials presenting different electronic degrees of freedom and different dimensions. This is my definition of *hybrid* –quantum– circuits.

During my postdoctoral stay in RIKEN, Japan, I have worked on the development of spin qubits devices for quantum information manipulation. These are made in quantum dots, formed in a semiconducting heterostructure hosting a two-dimensional electron gas (2DEG), by electrostatic gating with normal metal electrodes. A cobalt micromagnet generates a local slanted magnetic field which induces a spin-electric-coupling (SEC), allowing for electrically controlling individual spins. While very attractive qubit candidates for the long coherence and lifetime of the electron spin as well as for the scalability potential offered by the semiconductor industry, these kind of spin qubits have long suffered from the

presence of fluctuating nuclear spins in the host material, which induce strong dephasing. Fighting against this nuclear spin noise was thus a major task to undertake. With my colleagues in RIKEN, we exploited the slow dynamics of the nuclear spin bath, which I previously investigated in detail, to perform real time Hamiltonian estimation with a spin qubit in GaAs, which host 100% nuclear spins. We also developed spin qubit devices in host materials containing less (natural Si) to almost no (purified ^{28}Si) nuclear spins, ultimately demonstrating the most promising spin qubit so far. In all three platforms, we reached the fault tolerance threshold of quantum error correction. Carbon is another promising host material for spin qubits because it contains even fewer nuclear spins than silicon and can also be isotopically purified. In particular carbon nanotubes are promising host materials, however the promises have not been fulfilled yet, mainly because of the lack of electronically clean carbon nanotubes compared to GaAs or Si wafers, the difference coming from decades of industrial research and development on semiconductors. After developing an ultra-clean carbon nanotube platform at the ENS, we demonstrated highly coherent spin states in a microwave cavity competing with silicon devices in similar architectures.

Besides continuing an activity on spin qubits in carbon nanotubes at the ENS, I am also investigating the realization of exotic *topological* states of matter in low dimensional conductors. The most sought for of these excitations are Majorana zero modes, which are expected to be their own anti-particle and to possess non-abelian exchange statistics that could be used to encode information through topologically protected operations known as braiding. The intense worldwide research activity in this field is mainly focusing on using semiconducting nanowires having a strong intrinsic spin-orbit interaction with superconducting correlations induced by an epitaxial superconducting layer, the whole being subject to a large external magnetic field. These are the necessary ingredients to realize the topological phase in which the Majorana zero modes can emerge. Rather, I am adopting a different strategy in which a strong spin-orbit interaction is synthetically induced in the low dimensional conductor, concomitantly to an autonomous local magnetic field, with the use of a patterned magnetic texture. With this Hamiltonian engineering, we demonstrated a large spin-orbit interaction in a carbon nanotube, stronger than in semiconducting nanowires and we observed a possible signature of Majorana zero modes at zero external magnetic field.

The manuscript is organized as follows. In chapter 1, I briefly discuss the theoretical aspects of spin-electric-coupling using local magnets as well as spin texturing using a magnetic texture. We will see that all approaches essentially reduce to implementing a synthetic or artificial spin-orbit interaction. In chapter 2, I discuss spin qubits in nuclear spins environment. The first section will theoretically describe the hyperfine interaction leading to an equation for nuclear spin dephasing that is usually missing in the literature. Then the chapter will summarize my work on spin qubits in GaAs, SiGe, ^{28}Si and carbon nanotube as published in Refs. [1–5]. Finally in chapter 3 I will discuss the experimental results on the synthetic spin-orbit interaction in carbon nanotubes published in Ref. [6] as well as some preliminary unpublished results on the sensing of the induced spin texture with microwave photons. Both chapters 2 and 3 conclude with a *perspective* section in which I present my research projects for the coming years in these two activities.

Chapter 1

Controlled spin-orbit interaction

Spin or intrinsic angular momentum is a purely quantum property that is particularly attractive to encode quantum information. It generally induces a "spin" magnetic dipole moment which makes it addressable by a magnetic field. An external constant magnetic field is generally used to control the spectrum of electronic systems, lifting the spin degeneracy, on time scales much longer than the individual spins dynamics. Radio frequency external magnetic fields work well for manipulating ensemble of spins as in NMR or ESR [7]. Local magnetic fields from ferromagnets in combination with external magnetic fields or local electric fields can be used to generate and control spin currents [8]. When it comes to dynamically controlling individual spins, it becomes more challenging as the direct coupling to the magnetic field of a single spin is very weak (and typically grows as the square root of the number of spins). Sticking to a magnetic field drive, it is thus necessary to apply locally, close to the isolated electron spin, large currents of the order of several mA at the gigahertz frequency, which in turn heat up the device that is at a typical sub kelvin temperature. Despite these difficulties, the first demonstration of the manipulation of a single electron spin in a quantum dot was realized using this technique in GaAs [9]. The major drawback of this technique (heating due to large currents) comes from the fact that it is needed to reach high Rabi frequencies in GaAs spin qubits to observe the estimated qubit state evolution as oscillations, because of the large dephasing due to nuclear spins (this will be extensively detailed in chapter 2). In isotopically purified ^{28}Si where the dephasing time of spin qubits is orders of magnitude larger than in GaAs, much smaller Rabi frequencies are enough, which explains why this technique was still successfully employed until recently by some groups [10–12] although it might not be good enough any more for recent architecture development at the Kelvin range [13]. Standard ESR drive was not suitable at the time for developing spin qubits in GaAs (which was then the main working horse) and it does not provide an easy scheme to develop scalability.

The idea then arose that a specifically designed magnetic field, local to the electron spin, could be used to control it electrically through a so called spin-electric-coupling (SEC) [14], lifting the hindrances of the pure magnetic control. As we will discuss in this chapter, it turns out that such a spin-electric-coupling is equivalent to inducing an artificial spin-orbit coupling or interaction (SOC or SOI). Spin-orbit coupling is a relativistic effect initially described in the context of atomic physics with electrons moving in the electric field of the nucleus[1]. It can also arise in crystals with broken space inversion symmetry, thus becoming

[1]Initially spin-orbit coupling was thought to be a purely relativistic quantum effect described in the context of Dirac equation. However L. Thomas found an explanation without relying on the Dirac equation which "pushed Pauli to admit that relativistic quantum theory is not the only way to handle the spin

a material property. It shapes the electronic band structure (see Figure 1.1), lifting spin degeneracy at zero external magnetic field, except at zero momentum. Adding an external magnetic field (external or intrinsic, the latter usually being the case with topological insulators) can lead (in the case of Rashba spin-orbit) to the opening of an helical gap which results in spin-momentum locking. Such helical gaps are highly sought for because they are a key signature and ingredient for the realization of non trivial topological phases of matter. The number of materials with the right and strong enough intrinsic spin-orbit interaction is limited and it is therefore attractive to synthetically shape it in other materials where it is weak or absent. Spin-orbit coupling being equivalent to an oscillating magnetic field [16], it can be synthetically realized using a strong and inhomogeneous, on short distances, electric field (which is very challenging) or by using a spatially oscillating local magnetic field which is the approach that we chose and that we will discuss in this chapter.

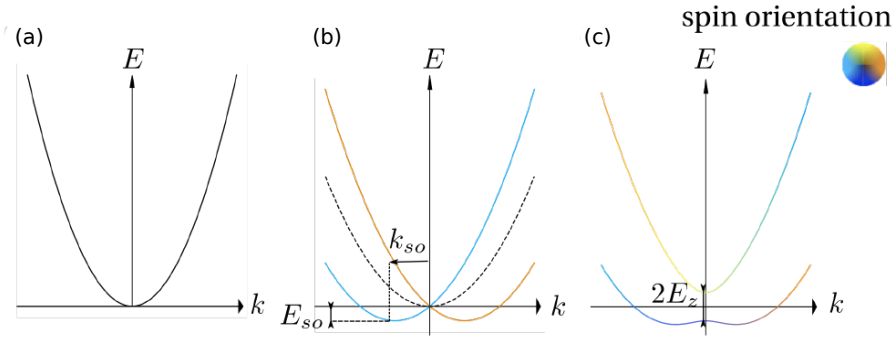

Figure 1.1: Evolution of the electronic bands of a 1D semiconductor (a) when adding first a Rashba type spin-orbit energy (b) and an additional magnetic field (c). The color-code represent the spin eigenvalue, except when the bands are degenerate in spin with no favored orientation (black). Figure taken from Ref. [17].

1.1 Electrical control of individual spins

1.1.1 Electron spin in a slanted magnetic field

In this subsection, we will discuss single spin (spin-1/2) qubits defined in a single quantum dot. The discussion is based on Ref. [14] where technical details can be found.

An efficient spin-electric-coupling scheme was first proposed in 2006 based on a local slanting, or slanted, magnetic field [14]. It was experimentally realized in 2008 in the group of S. Tarucha with the electrical control of a single electron spin-1/2 in a GaAs quantum dot [18]. The slanted magnetic field is created by a ferromagnet, usually in cobalt, deposited on top of the spin qubit quantum dot device. Its working principle is presented in Figure 1.2(a) and a design for optimal field gradients [19] is shown in Figure 1.2(b). An external magnetic field B_{ext} defines the spin quantization axis and the longitudinal direction z. The transverse component of the micromagnet field, along the x direction, is designed to have a constant gradient along z which is referred to as the transverse slanted

properly". The interested reader can find a detailed and clear demonstration of Thomas' reasoning in appendix A of Ref. [15]

term $b_t = (\boldsymbol{\nabla} \cdot \boldsymbol{B}_{\mathrm{MM}})_x$ with the subscript MM referring to micromagnet. Such a constant gradient can be realized by the micromagnet design presented in Figure 1.2(b), whose simulated magnetic field is shown in Figure 1.3(a). Around the center of the micromagnet with respect to the z axis, B^x_{MM} noted b_t in further is linear. Now, considering this term only, the magnetic field at the quantum dot position is $\boldsymbol{B} = b_t z \boldsymbol{u}_x + B_{\mathrm{ext}} \boldsymbol{u}_z$ with $\boldsymbol{u}_x$ and $\boldsymbol{u}_z$ unit vectors along x and z respectively. The Hamiltonian of the system writes

$$H = \frac{\hat{p}_z^2}{2m} + V(\hat{z}) - \frac{1}{2} g \mu_B \left(B_{\mathrm{ext}} \hat{\sigma}_z + b_t \hat{z} \hat{\sigma}_x \right), \tag{1.1}$$

with V the confinement potential assumed to be symmetric for simplicity, g the electron g-factor, μ_B the Bohr magneton and $\hat{\boldsymbol{\sigma}}$ the Pauli matrices for the spin. We see that the slanted term of the Hamiltonian couples position and spin and is therefore suggestive of a spin-orbit coupling. It is the general term that we will encounter in this chapter for artificial spin-orbit interaction. However, it is not similar to any spin-orbit coupling Hamiltonian like Rashba or Dresselhaus spin-orbit terms which explicitly couple spin and momentum. It is needed to do perturbation theory or (not exclusive) to restrict the Hilbert space to reveal the spin-orbit character of this term. Here second order perturbation with respect to the slanting field energy $E_{\mathrm{SL}} = -g\mu_B b_t L$, with L the potential confinement characteristics length, yields a restricted two-state Hilbert space defining the spin qubit. By periodically displacing the quantum dot in space along the z direction using an electric field, the confined electron spin will experience an oscillating transverse magnetic field. The time dependent perturbation Hamiltonian $H_{ac}(t) = eV_0 f(t)\hat{z}/L$ is an odd function of space and is spin independent, with $f(t)$ usually a cosine function. It therefore couples off-diagonal terms, which are in this case the two spin states of the qubit, leading to the effective Hamiltonian

$$H_{eff} = \frac{1}{2}\epsilon_z \hat{\sigma}_z + \frac{1}{2}\epsilon_x f(t) \hat{\sigma}_x, \tag{1.2}$$

which is the Hamiltonian of ESR that is now called within this scheme electron dipole spin resonance (EDSR) [14]. A key aspect here is that due to second order perturbation theory, the two states defining the qubit are combinations of the quantum dot orbitals. Therefore the reduced Hamiltonian (1.2) effectively hybridizes spin and orbital degrees of freedom and EDSR can be interpreted as an artificial spin-orbit coupling which adds to any intrinsic spin-orbit coupling.

To complete the picture of the micromagnet inhomogeneous magnetic field attractive features, we also note that there is a finite gradient of the z component of the field along the y direction. This gradient is provided by the asymmetry of the magnet with respect to the z axis through the "bridge" that connects its two large parts. This results in a y dependent $B^z_{\mathrm{MM}}(y)$ which allows for selectively addressing several spin qubits located at various positions along the y axis. Indeed, to first order, $\epsilon_z = \frac{1}{2} g \mu_B [B_{\mathrm{ext}} + B^z_{\mathrm{MM}}(y)]$ and EDSR is performed by applying $f(t) = \cos(\omega_{\mathrm{EDSR}} t)$ with $\omega_{\mathrm{EDSR}} = \epsilon_z/\hbar$. It is therefore possible to control selectively several spin qubits with the same micromagnet which has already been successfully done with 3 and 4 spin qubits [20, 21]. This makes the micromagnet a versatile and instrumental element of spin qubit devices in semiconducting materials which is at the heart of the discussion of chapter 2.

1.1.2 Two-site spin-orbit interaction

In this subsection, we will discuss spin-1/2 qubits defined in a double quantum dot. The discussion is mostly based on Refs. [22, 23] where technical details can be found.

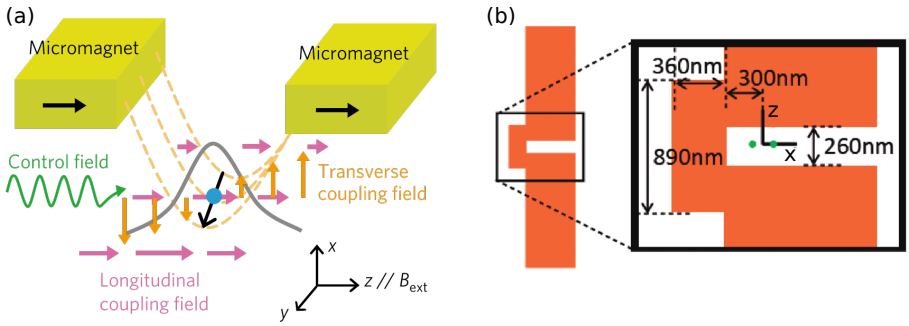

Figure 1.2: (a) Micromagnet spin–electric-coupling fields. The magnet is designed to induce a spatially inhomogeneous stray field $\boldsymbol{B}_{\mathrm{MM}}$ at the quantum-dot position when magnetized along $\boldsymbol{B}_{\mathrm{ext}} \parallel z$. The transverse coupling is produced by the inhomogeneous component perpendicular to $\boldsymbol{B}_{\mathrm{ext}}$ and is proportional to the field slope $b_t = (\boldsymbol{u}\cdot\boldsymbol{\nabla})B^{\perp}_{\mathrm{MM}}$ where $\boldsymbol{u}$ is the unit vector along an in-plane (yz) electric field, $\boldsymbol{\nabla}$ denotes the vector differential operator and $\perp$ indicates the component perpendicular to $\boldsymbol{B}_{\mathrm{ext}}$. The longitudinal coupling is, in contrast, mediated by the gradient of the parallel component $b_l = (\boldsymbol{u}\cdot\boldsymbol{\nabla})B^{z}_{\mathrm{MM}}$. The quantum-dot confinement is assumed to be strong vertically (along x) and symmetric laterally. (b) Typical design of a micro magnet which is optimizing the slanted field b_l at the location of the quantum dots for the situation of a modulation-doped GaAs/AlGaAs wafer with a 2DEG 57 nm below the surface with a 100 nm insulating layer on top. Figures are taken and adapted from Refs. [4, 19].

In the previous subsection, we have seen how a periodic displacement in continuous coordinates of an electron spin in a slanted magnetic field induces EDSR through an artificial spin-orbit interaction. It is also possible to reduce the continuous coordinates to discrete sites, down to two, using a double quantum dot. This scheme was first proposed in 2010 for a double quantum dot system with non-collinear ferromagnetic electrodes, using carbon nanotube as an example [22], and then in 2012 for a double quantum dot in a semiconducting heterostructure 2DEG with a micromagnet similar to the one discussed previously [23]. Both schemes are identical and result in the same Hamiltonian and artificial two-site spin-orbit interaction. These schemes have been proposed in the context of hybrid (or mesoscopic) circuit quantum electrodynamics (cQED) to achieve spin-photon coupling and were successfully implemented first in a carbon nanotube device with the demonstration of coherent spin-photon coupling [24] and then in silicon devices with the demonstration of the strong spin-photon coupling [25, 26].

The reasons behind using a double quantum dot are twofold : 1) Since the two dots are separated by few hundreds nanometers (this is much larger than the displacement of the single electron in the previous section, which is of the order of the quantum dot confinement length $\sim 20\,\mathrm{nm}$), there is a large (mesoscopic) electric dipole between the two dots which is given to the spin thanks to the non-collinear magnetizations. The photons of the cavity convey an electrical field which couples to this electric dipole and therefore to the spin. 2) A double quantum dot is a closed system and it is possible to finely tune the internal transition between the levels of the two dots to match the cavity frequency. This results in the cavity photons driving the transition that controls the localization of the electron on one dot or the other, effectively activating the large dipole. This working principle is depicted in Figure 1.4(a). In the proposal with non-collinear ferromagnetic electrodes, the quantization axis in each quantum dot is set by the local non-collinear magnetic fields

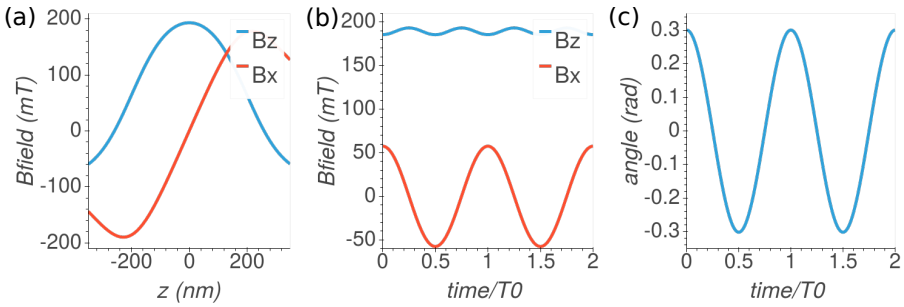

Figure 1.3: (a) Micromagnet magnetic stray fields $B^x_{\rm MM} \equiv B_x$ and $B^z_{\rm MM} \equiv B_z$ as a function of z at the position of a quantum dot, calculated for a micromagnet with a design similar to the one of Figure 1.2(b). (b) Micromagnet magnetic stray fields at the position of a quantum dot as a function of time for a cosine displacement of the quantum dot of amplitude 50 nm centred around $z = 0$ nm and period T_0. In typical experiments, the displacement is of the order of 20 nm, which is the confinement length. (c) Angle of the magnetic field at the quantum dot position as a function of time.

(induced by exchange interaction, see Figure 1.4(b), rather than through the stray field), $\boldsymbol{B}_L$ and $\boldsymbol{B}_R$ with L, R referring to the left and right dots and $\boldsymbol{B}_L \cdot \boldsymbol{B}_R = \cos(\theta)$ with θ the angle between the electrodes. In the proposal with a micromagnet (see Figure 1.4(c,d)), the two specific locations of the quantum dot in space also set two discrete quantization axis for the two quantum dots with $\boldsymbol{B}_\alpha = B^z_{\rm MM}(x_\alpha)\boldsymbol{u}_z + B^x_{\rm MM}(x_\alpha)\boldsymbol{u}_x$ with α in $\{ L, R \}$ and x_α the dot position along the x axis. In the ideal situation of a double quantum dot system exactly in the center of the micromagnet, we have $B^z_{\rm MM}(x_L) = B^z_{\rm MM}(x_R)$ and $B^x_{\rm MM}(x_L) = -B^x_{\rm MM}(x_R)$ giving a similar non-collinear configuration with $\theta = \arctan(2B^x_{\rm MM}/B^z_{\rm MM})$. With both approaches, the term coupling spin and position discussed in the previous section transforms from the continuous to discrete coordinates by projecting the system Hamiltonian onto the two orbitals, on the left and right dots, with spin subspace as

$$b_t \hat{z} \hat{\sigma}_x \longrightarrow B_x \hat{\tau}_z \hat{\sigma}_x, \tag{1.3}$$

with $\hat{\boldsymbol{\tau}}$ the Pauli operators in position (L,R), $\hat{\boldsymbol{\sigma}}$ the Pauli operators in spin and $B_x \equiv B^x_{\rm MM}$. The total Hamiltonian in this subspace is

$$H = \frac{1}{2}\left(\epsilon \hat{\tau}_z \hat{\sigma}_0 + 2t \hat{\tau}_x \hat{\sigma}_0 + g\mu_B B_z \hat{\tau}_0 \hat{\sigma}_z + g\mu_B B_x \hat{\tau}_z \hat{\sigma}_x\right), \tag{1.4}$$

with the subscript 0 used for the identity operator in the corresponding subspace, ϵ the energy detuning, t the tunnel coupling and $B_z = B_{\rm ext} + B^z_{\rm MM}$. It is interesting to include the intrinsic, if present, spin-orbit term (Rashba here) $H_R = \alpha_R(\hat{\sigma}_x \hat{p}_y - \hat{\sigma}_y \hat{p}_x)$ with α_R the Rashba spin-orbit strength and $\hat{\boldsymbol{p}}$ the momentum operator. A similar transformation to (1.3) assuming a Gaussian wave function gives [23]

$$\alpha_R(\hat{\sigma}_x \hat{p}_y - \hat{\sigma}_y \hat{p}_x) \longrightarrow \lambda_x \hat{\tau}_z \hat{\sigma}_x, \tag{1.5}$$

with $\lambda_x = \alpha_R l S/(a^2\sqrt{1-S^2})$, $S = \langle L|R\rangle = \exp[-(l/a)^2]$, a the radius of the single dot ground state Gaussian wave function and l the half distance between the two dots. The two transformed terms of Eqs. (1.3) and (1.5) have the same structure, pinning down the artificial spin-orbit equivalence of the two sites with non-collinear magnetic fields in the qubit reduced subspace. To finalize the discussion on the spin-photon coupling, we can look at the problem in the basis of bonding and antibonding orbitals $n = -, +$ with spin

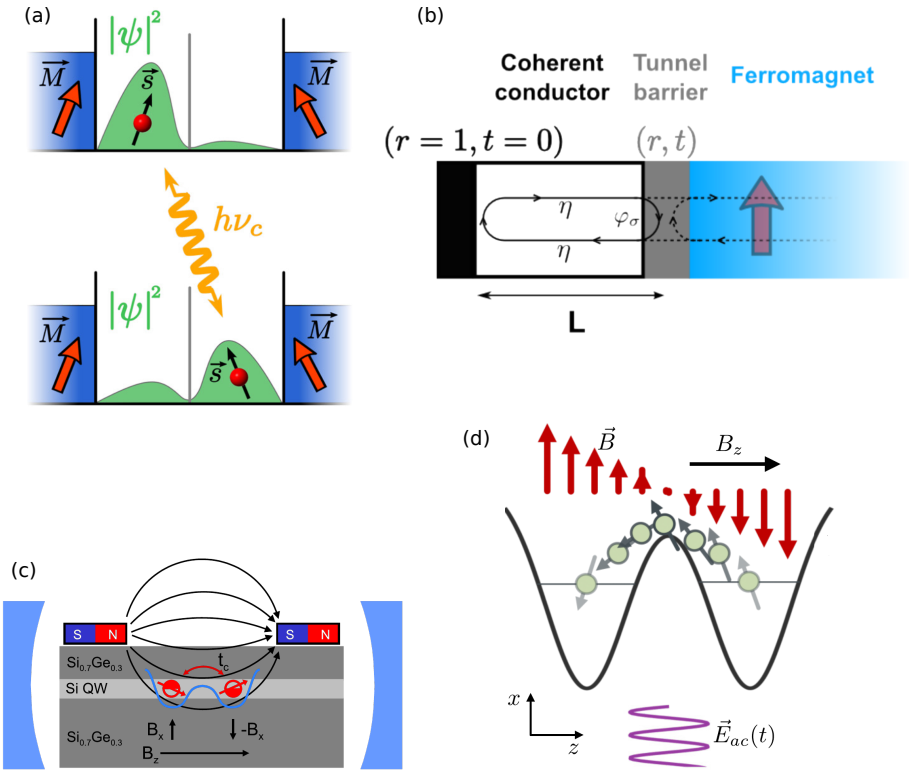

Figure 1.4: (a) General principle of the two-site spin-orbit coupling mechanism with non-collinear ferromagnetic electrodes activated by cavity photons. The proximity of the non-collinear ferromagnets induces a different equilibrium spin orientation if an electron is localized in the left or in the right dot. Photons are coupled to transitions changing the localization of the wave function ψ and hence coupled to transitions changing the spin orientation. (b) Principle of the confinement-induced exchange field arising from tunnel coupling to a ferromagnetic lead. ϕ_σ is a spin-dependent interfacial phase shift and η is the electronic path acquired by the electronic phase when propagating through the coherent conductor over a length L. (c) and (d), principle of the two-site spin-orbit coupling mechanism with a micromagnet slanted magnetic field. Despite the continuous character of the slanted field, the two specific locations of the quantum dots turn it to a discrete two-site spin-orbit coupling with equivalent non-collinear magnetic fields composed by B_x being different for each dot and B_z being the same. Figures are taken and adapted respectively from Refs. [24, 27–29].

$\sigma = \uparrow, \downarrow$ in the z direction, defining the basis $\{ \mid +, \uparrow\rangle, \mid +, \downarrow\rangle, \mid -, \uparrow\rangle, \mid -, \downarrow\rangle \}$. The dipole operator (coupling to the cavity electric field) couples the states $|+, \sigma\rangle$ and $|-, \sigma\rangle$, the field gradient operator (artificial spin-orbit) couples $|n, \sigma\rangle$ and $|\bar{n}, \bar{\sigma}\rangle$ so that the combination of these two effects effectively leads to a coupling between the two spin states on the same orbital $|n, \sigma\rangle$ and $|n, \bar{\sigma}\rangle$, realizing the desired single spin qubit coupled to microwave photons.

1.2 Synthetic spin-orbit interaction with magnetic textures

In this subsection, we will discuss how to induce a synthetic spin-orbit interaction with a spatially periodic magnetic field. We will first consider the case of a quantum dot subject to such a field, similarly to previous sections, and then the ideal case of a infinite conductor. An in-depth overview with all the technical details can be found in the thesis of L. Contamin [17].

As outlined in the introduction of this chapter, spin-orbit coupling is equivalent to a spatially oscillating magnetic field [16]. This can be generated either by localized magnetic moments that order through the Ruderman-Kittel-Kasuya-Yosida (RKKY) mechanism, thanks to their coupling to conduction electrons. This was studied both in atomic chains [30–32] and in ^{13}C carbon nanotubes [33, 34]. Or it can be the stray field of a nearby magnetic material [35–38] (either a ferromagnet with domains, an array of magnets or an array of magnetic tunnel junctions). We chose the latter option, an interesting aspect of this choice being that one can in theory control the magnetic domains and thus the effective spin-orbit interaction, either by applying a magnetic field [6], as will be discussed in chapter 3, or by flowing a current through the ferromagnet.

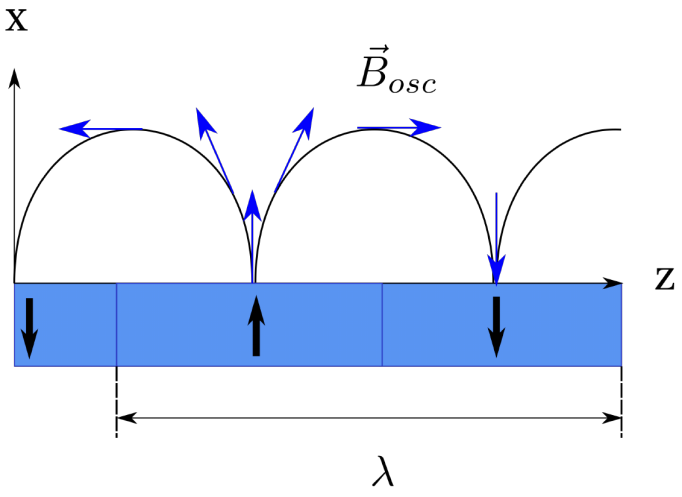

Figure 1.5: Schematics of a magnetic texture's stray field. Oscillating magnetic field considered in the calculation. For a succession of domains (or nanomagnet, drawn in blue), the field lines follow the black curve. At a given altitude x (close to the surface), one can in first approximation consider that the amplitude of the oscillating field B_{osc} is constant along z, with an oscillation of its direction. The period of this oscillation is λ, corresponding to two domains/magnets with opposite magnetization. Figure taken from Ref. [17].

The periodically oscillating magnetic field that we will consider is generated by mag-

netic domains whose magnetization alternately point upward and downward out of the plane, as depicted in Figure 1.5. Before looking at the 1D limit, we will investigate the quantum dot case, in line with the discussion of previous sections. The magnetic texture stray field can be written as

$$\boldsymbol{B}_{\text{osc}} = B_{\text{osc}} \begin{pmatrix} \sin(k_\lambda z) \\ 0 \\ \cos(k_\lambda z) \end{pmatrix}, \tag{1.6}$$

with $k_\lambda = 2\pi/\lambda$, λ being the spatial period of the texture. We consider a quantum dot confined in a 1D conductor, as we will discuss the case of a carbon nanotube in the last chapter. In this case, in the absence of magnetic texture, the wave function corresponding to the n-th orbital of the dot with spin σ is, not taking into account the CNT band structure for a simplified discussion

$$\psi_{n,\sigma} = \sqrt{\frac{2}{L}} \sin(k_{n,\sigma} z), \tag{1.7}$$

with L the length of the dot and $k_{n,\sigma} = n\pi/L$. The eigenenergies are $E_{n,\sigma} = \hbar v_F k_{n,\sigma}$ with v_F the Fermi velocity. We will describe the effect of the oscillating field, using again perturbation theory, considering $\frac{1}{2} g\mu_B B_{\text{osc}} \ll \Delta E$ with $\Delta E = hv_F/2L$ the level spacing of the dot. This time, we have to do perturbation theory of degenerated states as the spin degeneracy is not lifted in the unperturbed Hamiltonian. We thus have

$$\begin{aligned} E^{(2)}_{n,\sigma} =& E^{(0)}_{n,\sigma} + \sum_{\sigma' = \{\sigma, \bar{\sigma}\}} \frac{1}{2} g\mu_B \langle n, \sigma | \boldsymbol{B}_{\text{osc}} \cdot \hat{\boldsymbol{\sigma}} | n, \sigma' \rangle + \\ & \sum_{n' \neq n} \sum_{\sigma', \sigma''} \frac{(\frac{1}{2} g\mu_B)^2 \langle n, \sigma | \boldsymbol{B}_{\text{osc}} \cdot \hat{\boldsymbol{\sigma}} | n', \sigma'' \rangle \langle n', \sigma'' | \frac{1}{2} g\mu_B \boldsymbol{B}_{\text{osc}} \cdot \hat{\boldsymbol{\sigma}} | n, \sigma' \rangle}{E_n - E'_n}. \end{aligned} \tag{1.8}$$

The bracket terms write generically

$$\langle n, \sigma | \boldsymbol{B}_{\text{osc}} \cdot \hat{\boldsymbol{\sigma}} | n, \sigma' \rangle = B^z_{\text{eff}}(n, \sigma, n', \sigma') \langle \sigma | \hat{\sigma}_z | \sigma' \rangle + B^x_{\text{eff}}(n, \sigma, n', \sigma') \langle \sigma | \hat{\sigma}_x | \sigma' \rangle, \tag{1.9}$$

with

$$B^z_{\text{eff}}(n, \sigma, n', \sigma') = \frac{B_{\text{osc}}}{2} \left(\frac{\sin[(k_\lambda - k_n + k_{n'})L]}{(k_\lambda - k_n + k_{n'})L} + \frac{\sin[(k_\lambda + k_n - k_{n'})L]}{(k_\lambda + k_n - k_{n'})L} \right) \tag{1.10}$$

$$B^x_{\text{eff}}(n, \sigma, n', \sigma') = \frac{B_{\text{osc}}}{2} \left(\frac{1 - \cos[(k_\lambda - k_n + k_{n'})L]}{(k_\lambda - k_n + k_{n'})L} + \frac{1 - \cos[(k_\lambda + k_n - k_{n'})L]}{(k_\lambda + k_n - k_{n'})L} \right) \tag{1.11}$$

We see that the first order correction already introduces a mixing of the two spins within the same orbital ($n = n'$) through the $\hat{\sigma}_x$ operator, given $L \neq p\lambda$ with $p \in \mathbb{Z}$, meaning that the size of the dot should not be commensurable with the magnetic texture period to see this correction. Then of course, the second order correction term mixes spins and orbitals through the $\hat{\sigma}_x$ operator again, leading to the synthetic spin-orbit interaction. We note that these terms quickly decrease with the orbital separation (as $\sim 1/(n-n')\Delta E$) and can show resonant condition for $k_\lambda \approx \pm(k_n - k_{n'}) + 2\pi p/L$. The overlap between the electron wave function and the oscillating magnetic field sets the amplitude of the synthetic spin-orbit coupling and is a critical aspect of the phenomenon. High in the electron

band (at high chemical potential), wave functions oscillates fast in space, therefore giving effectively an average of the magnetic texture field with a small evolution from one orbital to the other. On the contrary, low in the electron band, close to the helical gap opened by the magnetic texture (we will shortly come back to this point), it will be possible to have k_n close to k_λ, thus giving an overlap of the electron wave function on one dot with the magnetic field strongly dependent on the orbital, which in turn can yield a potentially strong spin-orbit coupling.

The synthetic spin-orbit nature induced by the magnetic texture is more clearly seen in the limit of an infinite 1D conductor. In this ideal case, a unitary transformation to the rotating frame of the cycloidal magnetic field directly gives a term in the Hamiltonian which has the same structure as Rashba spin-orbit interaction. Indeed, if we consider the 1D Hamiltonian for a free electron [36]

$$H = \left(\frac{\hat{p}_z^2}{2m} - \mu\right)\hat{\gamma}_z + \frac{1}{2}g\mu_B \boldsymbol{B}_{\text{osc}} \cdot \hat{\boldsymbol{\sigma}}, \tag{1.12}$$

with $\hat{\gamma}$ Pauli matrices operating in sublattice space and apply the unitary transformation $\tilde{H} = UHU^\dagger$ with

$$U = e^{i\Phi\hat{\sigma}_{xy}/2}, \qquad \cos(\Phi) = \frac{\boldsymbol{B}_{\text{osc}} \cdot \boldsymbol{u}_z}{B_{\text{osc}}}, \qquad \hat{\sigma}_{xy} = \frac{(\boldsymbol{B}_{\text{osc}} \times \boldsymbol{u}_z) \cdot \boldsymbol{u}_z}{\|\boldsymbol{B}_{\text{osc}} \times \boldsymbol{u}_z\|}$$

,

we find

$$\tilde{H} = \left(\frac{\hat{p}_z^2}{2m} - \mu + \frac{E_{\text{so}}}{2}\right)\hat{\gamma}_z + B_{\text{osc}}\hat{\sigma}_z + \frac{\alpha}{\hbar}\hat{p}_z\hat{\sigma}_y\hat{\gamma}_z. \tag{1.13}$$

We thus see that the oscillating magnetic field is equivalent to both a constant Zeeman effect of amplitude B_{osc} and a synthetic spin-orbit interaction of Rashba form with perpendicular quantization axis. The combination of both terms opens a helical gap in the band structure as recalled in Figure 1.1(c). The spin-orbit coupling strength is $\alpha = \pi h^2/m\lambda$ and the corresponding spin-orbit energy is $E_{\text{so}} = h^2/4m\lambda^2$. The synthetic spin-orbit interaction also shifts the chemical potential to $\tilde{\mu} = \mu - E_{\text{so}}/2$, which in turns shifts the position of the helical gap in energy. It is interesting to note that a similar helical band gap can be found in a finite length wire with a cycloidal magnetic field using scattering formalism (see the supplementary information of Ref. [6] or the thesis of L. Contamin for in-depth analysis [17]), without the Rashba term explicitly showing-up.

Generically, we have seen that an electron moving in an inhomogeneous magnetic field (either within quantum dots or as a free electron) leads to a spin-orbit interaction with more or less direct evidence. It turns out that the two situations of the previous slanted magnetic field section for spin qubits and the periodic magnetic field for helical band gap shaping of this section are very much similar. Indeed, the periodic displacement of the electron in the slanted magnetic field is equivalent to having a free electron in a cycloidal magnetic field with an offset on the z component of the field, as shown in Figure 1.3(b,c). In this situation, the magnetic field vector does not fully rotate by 2π during a period as compared to the ideal cycloidal case (see Figure 1.6), yet still yields an artificial spin-orbit interaction. We note that adding a constant external magnetic field to the cycloidal magnetic field of this section (Figure 1.6(a)) actually gives the same field structure as the slanted field configuration (Figure 1.6(b)) which is the experimental realization that we

will discuss in the last chapter. However it does not seem obvious from the ideal infinite 1D conductor unitary transformation that adding a constant external magnetic field would also provide a synthetic spin-orbit interaction. Indeed, in the rotating frame of the magnetic texture field, the constant external magnetic field becomes rotating. As we experimentally apply an external magnetic field to investigate the effect of the magnetic texture on the electronic excitations, we would need to look deeper into this theoretical aspect. Finally, to close the loop of this chapter back to spin qubits, we should mention that spin qubits can be defined with states lying in a helical gap, which could be engineered, and be coupled to microwave photons [39].

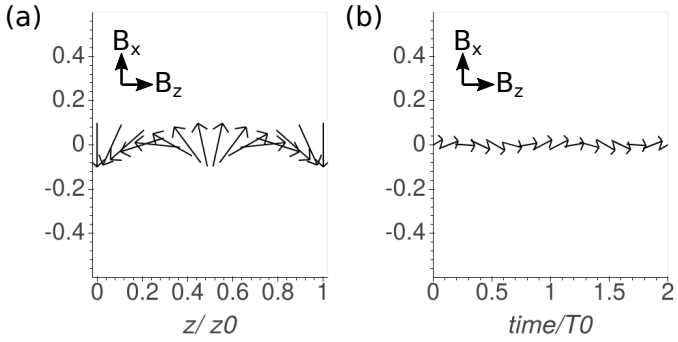

Figure 1.6: Magnetic stray field vector fields as a function of space for the case of (a) the magnetic texture of Figure 1.5 and as a function of time for the case of (b) the micromagnet slanted field with periodic displacement of the quantum dot of Figure 1.3.

Chapter 2

Spin qubits in a nuclear spin bath environment

Electron spin qubits are attractive candidates for manipulating quantum information. One of the primary reason is their supposedly long coherence time due to the weak coupling that spins have to their environment. As discussed in section 1.1, the weak coupling of spins to environment impedes their control and electrical control through spin-electric-coupling schemes have been accordingly devised. These in turn obviously open a breach in the long coherence time origin of spin qubits, by adding a noise source, namely charge noise. Additionally, these spin qubits are not hanging in vacuum but are hosted in a material. The nuclear spins of the host material atoms interact with the electron spin qubit through hyperfine coupling. The spin qubit environment is therefore a bath of fluctuating nuclear spins which plays the role of a magnetic noise source. It turns out that the fluctuating magnetic field generated by nuclear spins, also called the Overhauser field, is the largest source of dephasing for spin qubits. As such, most efforts have been put for years on understanding and fighting it. We should stress here that nuclear spins in semiconductor materials were well investigated and manipulated for decades before the arrival of spin qubits, in particular in the context of nuclear magnetic resonance (NMR) [7]. However, it is only after the seminal theoretical proposal to manipulate quantum information with electron spins [40], and the first experimental hints of their long relaxation times [41] that nuclear spin dephasing of electron spins was theoretically investigated in-depth [42–44].

2.1 Nuclear spins dephasing

2.1.1 Hyperfine coupling

In this section, we will briefly derive the dephasing time T_2^* of an electron spin due to the hyperfine coupling to nuclear spins of the environment, finding an expression that is absent (to our knowledge) from the literature, explicitly showing the nuclear spins concentrations.

In classical electrodynamics, in the limit of zero distance between two magnetic dipoles[1], the dipole-dipole interaction or energy is given by the Fermi contact interaction [45]

$$E_{Fc} = -\frac{2\mu_0}{3}\boldsymbol{m_1}\cdot\boldsymbol{m_2}\delta(\boldsymbol{r_1}-\boldsymbol{r_2}), \tag{2.1}$$

[1]The more "classical" dipole-dipole interaction with a $1/r^3$ dependence is valid only if the distance between the dipoles is much larger than the dipole dimension, which is not the case here.

with $\boldsymbol{m_1}$ and $\boldsymbol{m_2}$ the two dipoles and μ_0 the magnetic permeability. For electrons

$$\boldsymbol{m} = -\gamma_e \hbar \frac{\boldsymbol{\sigma}}{2} = -g_e \frac{e}{2m_e} \hbar \frac{\boldsymbol{\sigma}}{2} = -\frac{g_e}{2} \mu_B \boldsymbol{\sigma}, \tag{2.2}$$

with $\boldsymbol{\sigma}$ is the vector of Pauli matrices. For nuclear spins

$$\boldsymbol{m} = \gamma_n \hbar \mathbf{I}_n = g_n \frac{e}{2m_p} \hbar \mathbf{I}_n. \tag{2.3}$$

The proportionality factor between the electron and the orbital and magnetic moment is the gyromagnetic ratio γ_e, alternatively parametrized by the g-factor g_e, quantifying how the magnetic moment differs from the classical value of $e/2m_e$ with m_e the electron mass. For nuclei, analogous quantities are defined, with the electron mass replaced by the proton mass m_p and $\mathbf{I}$ the vector of nuclear spin operators.

The resulting Hamiltonian follows

$$H_{hf} = \sum_n \tilde{\beta}_n \tilde{\delta}(\boldsymbol{r} - \boldsymbol{r}_n) \mathbf{I}_n \cdot \boldsymbol{\sigma}. \tag{2.4}$$

The sum goes over all nuclear spins, labelled by a discrete index n, which are located at positions $\boldsymbol{r}_n$. The electron position is at $\boldsymbol{r}$, its spin is σ. Sometimes $\boldsymbol{s} = \boldsymbol{\sigma}/2$ is used instead, giving twice larger interaction constants. From Eqs. (2.2) and (2.3) we have

$$\tilde{\beta}_n = \frac{2\mu_0}{3} \frac{g_e}{2} \mu_B \mu_N g_n. \tag{2.5}$$

Two points have to be commented here. First, the g-factor of the electron is the vacuum one, not the band structure one, meaning that it is the same for GaAs, Silicon or Carbon [46]. Second, the position operator in Eq. (2.4) acts on the full wave function of the electron $\Phi(\boldsymbol{r}) = \Psi(\boldsymbol{r})\psi(\boldsymbol{r})$ including its Bloch part $\psi(\boldsymbol{r})$ and its envelope $\Psi(\boldsymbol{r})$. The former is periodic in the crystal lattice, dimensionless and normalized such that the integral over the unit cell of its modulus squared is equal to the volume of the unit cell. The volume integral of $\Phi(\boldsymbol{r})$ is then equal to the volume integral of $\Psi(\boldsymbol{r})$. With this, the matrix elements of any operator smoothly varying on the inter-atomic distances can be calculated ignoring the Bloch part. However here, the delta function in Eq. (2.4) is not smooth and has to be dealt with explicitly. To keep the envelope part, which is convenient, the prefactors change to (removing the tilde)

$$\beta_n = \frac{2\mu_0}{3} \mu_B \mu_N g_n |\psi(\boldsymbol{r}_n)|^2, \tag{2.6}$$

using $g_e = 2$. Thus we have

$$H_{hf} = \sum_n \beta_n \delta(\boldsymbol{r}_n - \boldsymbol{r}) \mathbf{I}_n \cdot \boldsymbol{\sigma}, \tag{2.7}$$

in the microscopic form of the hyperfine interaction, useful for quantum dots. The interaction strengths β_n have dimensions of energy times volume and their values for different isotopes in GaAs, Silicon and Carbon are given in Table 2.1

2.1.2 Matrix elements for quantum dot states

For quantum dots, we are interested in matrix elements of the Hamiltonian Eq. (2.7). Taken as an operator, it connects states with different spin, as well as different orbital. Most often, only the diagonal elements in orbital subspace are of interest (see for example

Nucleus	spin	g-factor	abundance	β_n μeVnm^3	A_n μeV
^{69}Ga	3/2	1.35	60%	1.13	37
^{71}Ga	3/2	1.7	40%	0.89	48
^{75}As	3/2	0.96	100%	1.06	47
^{29}Si	1/2	-1.1	4.7%	-0.05	-2.52
^{13}C	1/2	1.40	1.1%		0.1–0.5

Table 2.1: Table presenting atomic quantities related to the hyperfine contact useful for our purpose. The values are taken from Refs. [44, 46] for GaAs and Si and from Refs. [47, 48] for carbon which are calculated for carbon nanotubes. The values of A_n from Ref. [46] are twice bigger as they use $\boldsymbol{s}$ and not $\boldsymbol{\sigma}$.

Refs. [49, 50] for calculation of off-diagonal elements both in orbital and spin indexes). The expectation value of Eq. (2.7) in the orbital state $\Psi(\boldsymbol{r})$ is

$$\langle H_{hf}\rangle_\Psi \equiv \langle\Psi|\sum_n \beta_n \delta(\boldsymbol{r}_n - \boldsymbol{r})\mathbf{I}_n\cdot\boldsymbol{\sigma}|\Psi\rangle = \sum_n \beta_n |\Psi(\boldsymbol{r}_n)|^2 \mathbf{I}_n\cdot\boldsymbol{\sigma} \tag{2.8}$$

From here it is convenient to multiply and divide by the volume corresponding to one spin because we will later go from the discrete sum to a volume integral using

$$\sum_n f(\boldsymbol{r}_n) = \frac{1}{v_0}\sum_n v_0 f(\boldsymbol{r}_n) \approx \frac{1}{v_0}\int d\boldsymbol{r} f(\boldsymbol{r}), \tag{2.9}$$

valid as long as the function is smooth. The volume v_0 corresponding to one spin is the volume corresponding to one atom, for zinc-blende crystals like GaAs with 8 atoms per cell units, $v_0 = a_0^3/8$ with a_0 the lattice constant. Using $A_n = \beta_n/v_0$ (given in Table 2.1), we get

$$\langle H_{hf}\rangle_\Psi = v_0\sum_n A_n|\Psi(\boldsymbol{r}_n)|^2\mathbf{I}_n\cdot\boldsymbol{\sigma}. \tag{2.10}$$

This form is appealing as A_n have the dimension of energy and the rest together is dimensionless. Now comes the tricky part to properly deal with elements and isotopes. GaAs is easy as all nuclei and their isotopes have a nuclear spin. We can simplify things by averaging over the isotopes to get a single value of $A \approx 45\,\mu\text{eV}$. In silicon or carbon, not all nuclei have a spin, only a proportion p of the isotopes. We can do two things: 1) analogously to GaAs, using the volume v_0 and averaging A_n including the zero-spin isotope, giving $A \equiv pA_n$, which does not corresponding to any atom, or 2) using the "true" A_n of ^{29}Si or ^{13}C and multiplying and dividing by v_0/p instead of v_0. The first choice hides the prefactor p inside A, defining it as pA_n, the second leaves it with v_0, but both give the same result

$$\langle H_{hf}\rangle_\Psi = v_0 p\sum_n A_n|\Psi(\boldsymbol{r}_n)|^2\mathbf{I}_n\cdot\boldsymbol{\sigma}, \tag{2.11}$$

where the 100% nuclear spin isotopes expression is naturally recovered for $p = 1$.

2.1.3 The dephasing time

We now calculate the average value of the modulus of the Overhauser field, defined as the vector multiplying the sigma matrices in Eq. (2.11). The average here is a statistical

average over unpolarized and uncorrelated nuclear spins defined by

$$\langle \mathbf{I}_n^\alpha \rangle = 0, \qquad \langle \mathbf{I}_n^\alpha \mathbf{I}_m^\beta \rangle = \delta_{\alpha\beta}\delta_{nm}\frac{I(I+1)}{3}, \tag{2.12}$$

with n, m atom indexes and α, β Cartesian coordinate indexes. The square of the Overhauser field along an arbitrary axis (z for example) is

$$\Delta^2 = \langle v_0 p \sum_n A_n |\Psi(\boldsymbol{r}_n)|^2 \mathbf{I}_n^z v_0 p \sum_m A_m |\Psi(\boldsymbol{r}_m)|^2 \mathbf{I}_m^z \rangle \tag{2.13}$$

$$= v_0 p^2 \frac{I(I+1)}{3} v_0 \sum_n A_n^2 |\Psi(\boldsymbol{r}_n)|^4. \tag{2.14}$$

Using an averaged A (actually one should calculate an averaged A_n^2, which is very close for GaAs $\langle A_n^2 \rangle \approx \langle A_n \rangle^2$ and the same for silicon or carbon) and Eq. (2.9), we get

$$\Delta^2 = v_0 p^2 A^2 \frac{I(I+1)}{3} \int d\boldsymbol{r} |\Psi(\boldsymbol{r})|^4 = \frac{v_0}{V_D} p^2 A^2 \frac{I(I+1)}{3}, \tag{2.15}$$

with V_D the quantum dot volume, equal to $2\pi l_x l_y l_z$ for a harmonic confinement. Finally, we reach our initial goal, the dephasing rate is obtained as

$$T_2^* = \frac{\hbar}{2\Delta} = \frac{\hbar}{2pA}\sqrt{\frac{3}{I(I+1)}\frac{V_D}{v_0}}. \tag{2.16}$$

This equation is the central result of this section which is surprisingly difficult to find, if present, in the literature. It calls for several important comments. For the following, $N_S = pN = pV_D/v_0$ the total number of nuclear spins within the quantum dot is also a useful quantity to manipulate. The question which drives everyone involved in spin qubits is how to improve the dephasing time T_2^*. We have the following options:

1. The dephasing rate is inversely proportional to A and I so it is wise to choose a material where both are small. Looking at Table 2.1 we see that carbon is better than silicium which is much better than GaAs for both quantities.

2. Fixing the material, hence A, and not changing the isotopic proportions (p is constant), we have $T_2^* \propto \sqrt{V_D}$ or equivalently $T_2^* \propto \sqrt{N_S}$. Larger quantum dots with *more nuclear spins improves the dephasing time*, due to the statistical narrowing of the variance of the Overhauser field, which can be observed through motional motional narrowing for example [51, 52].

3. Now fixing the quantum dot volume V_D and changing p through isotopic purification to change the nuclear spins concentration, we have $T_2^* \propto 1/p$ or equivalently $T_2^* \propto 1/N_S$. Here we find the intuitive result that *less nuclear spins is better for the dephasing time*. Current isotopic purification technologies that remove ^{29}Si or ^{13}C typically reach $p \sim 8 \times 10^{-4}$ (800 ppm).

Dephasing times T_2^* for GaAs, silicon and carbon nanotubes with various isotopic concentrations are presented in Table 2.2. For carbon nanotubes, the number of atoms is calculated using

$$N = \frac{4\pi}{3\sqrt{3}a_{CC}^2} LR, \tag{2.17}$$

with $a_{CC} = 1.42\,\text{Å}$ the lattice constant, $L \approx 200\,\text{nm}$ the length and $R \approx 2\,\text{nm}$ the radius of the CNT. This expression is obtained by combining Eqs. (3.2), (3.7) and (3.9) of Ref. [53]. For isotopically purified materials, the estimated hyperfine induced dephasing times are so large that most often charge noise becomes the dominant dephasing source [4] as will be discussed in subsection 2.3.2. We note also the very large predicted values for CNT (calculated using $A = 0.5\,\mu\text{eV}$) which are far from what has been measured experimentally so far. We will come back to this point in more details in subsection 2.3.3.

Before discussing actual experimental realizations of spin qubits in silicon, purified silicon and carbon nanotubes where the dephasing time should be significantly enhanced compared to GaAs spin qubits, we will first have a look at another important aspect of hyperfine induced dephasing, the dynamics of the nuclear spin bath.

	GaAs	Si natural	Si purified	CNT natural	CNT purified
p	1	0.047	8×10^{-4}	0.011	8×10^{-4}
N	$\sim 2 \times 10^6$	$\sim 10^5$	$\sim 10^5$	$\sim 5 \times 10^4$	$\sim 5 \times 10^4$
T_2^* (µs)	~ 0.01	~ 2	~ 120	~ 25	~ 350

Table 2.2: Table summarizing the dephasing times for quantum dot spin qubits in various materials and with different nuclear spins isotope concentrations.

2.2 Dynamics of the nuclear spins bath

This section mostly discusses results published in Ref. [1] as well as some results published in Refs. [2, 54].

The dephasing time described in the previous section was originally defined in the context of NMR as the source of the observed finite resonance linewidth [7]. As such experiments are usually performed in the steady state and on large ensembles of spins, this dephasing time reflects the system inhomogeneity over a large range both in space and time. The hallmark of the nuclear spin environment is its very slow internal dynamics [55], due to the weakness of nuclear spin-spin interactions [56, 57]. Due to this slowness, the typical total operation time of spin qubits is usually much shorter than the decorrelation time of the noise. This is a very different regime than in NMR where the "infinite" averaging over space or time renders the noise uncorrelated or white. Therefore it is expected that in the correlated noise, or non-ergodic, regime, the dephasing time might be strongly affected.

To briefly give a picture of the decorrelation time of the noise, we can model the dipole-dipole hyperfine noise as being diffusive, and equivalently following a random walk [58]. A warning about this model which is widely used and accepted has to be made however. The diffusiveness of the nuclear spin bath is an assumption with which calculations can be performed but, quoting A. G. Redfield [59] "*In many cases it is difficult, if not impossible, to prove theoretically whether or not such spin diffusion actually occurs, but if we assume that it does, then it is possible in principle to find a unique value for the diffusion coefficient D*"; we see that we should keep in mind that diffusion is only an assumption. As the Overhauser field is bounded in amplitude to $\Delta = \sigma_B(\infty)$, the diffusion cannot spread infinitely, and must be bounded as well. A simple model to account for such boundary effect is the Ornstein-Uhlenbeck process [60]. Assuming that at the beginning of operations,

the Overhauser field is $B(t=0)$, the mean value of B decays exponentially to zero as $\langle B(t)\rangle = B(0)e^{-t/T_0}$, the memory of the initial value also decays exponentially to zero as $\langle B(t)B(0)\rangle = B(0)^2 e^{-t/T_0}$ and the variance grows linearly until it saturates exponentially as $\langle [B(t) - \langle B(t)\rangle]^2\rangle = \sigma_B^2(\infty)(1 - e^{-2t/T_0})$. Within this model, the decorrelation time is $T_0 = 2\sigma_B^2(\infty)/D$ with D the diffusion coefficient of the diffusive process. For GaAs, reported decorrelation times ranges from seconds to hours due to variations in doping, strain and nanostructure confinement. As the measurement of the qubit is of projective nature and one has therefore to average many observations to infer the estimated quantum state probability, sticking to the uncorrelated white noise regime of the Overhauser field would impose to have a repetition rate of several T_0, which is obviously too slow for quantum information manipulation, if not simply impractical. This is the motivation for investigating the nuclear spin bath dynamics and the dephasing time in the non ergodic regime using the spin qubit as a fast and sensitive probe.

The use of a singlet-triplet (ST) qubit [61, 62] is well suited for this purpose as its oscillation frequency is directly subject to the nuclear field fluctuations. ST qubits require two quantum dots, which in this work are the two rightmost dots of a triple quantum dot device shown in Figure 2.1(a). A micromagnet as described in subsection 1.1.1 generates a magnetic field difference ΔB^z_{MM} between the dots[2], setting the average frequency of the qubit $f = |g|\mu_B \Delta B_z/2\pi\hbar$ with $\Delta B_z = \Delta B^z_{\mathrm{MM}} + \Delta B^z_{\mathrm{nuc}}$ and $g = -0.44$ the electron g-factor in GaAs. The leftmost spin qubit is left idle during all operations in this work.

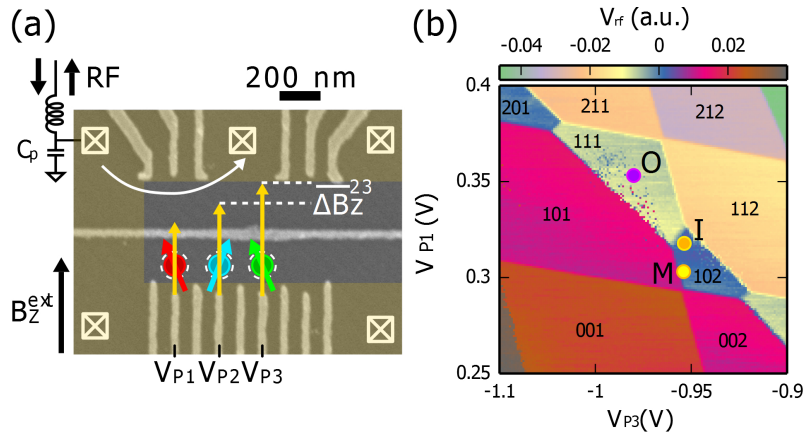

Figure 2.1: (a) SEM micrograph of a similar device to the one measured. Lateral gates defining quantum dots (bottom) and charge sensors (top) are shown in light grey on the dark grey surface of the GaAs substrate. The three leftmost quantum dots are formed and manipulated while the upper left charge sensor, connected to an rf-reflectometry circuit is used. The "C-shaped" light colored area denotes the micromagnet providing inhomogeneous magnetic field. An external magnetic field $B_z^{ext} = 0.7\,\mathrm{T}$ is applied. (b) Charge stability diagram in the plane defined by plunger gates P_1 and P_3. The positions for initialization (I), operation (O) and measurement (M) configurations are denoted.

The qubit dephasing time T_2^* is extracted from the free induction decay of the ST qubit. The measurement scheme is organized such that we can access the evolution of the dephasing as a function of the acquistion time. The basic unit is a "cycle" (index

[2]We do not use EDSR provided by the micromagnet for the ST qubit. Rather, we exploit the gradient of $B^z_{\mathrm{MM}}(y)$ conceived for scalability to generate the inhomogeneous Zeeman field which sets the ST qubit energy.

c) during which the qubit is initialized in the state $|\uparrow, \mathrm{S}(0,2)\rangle$, then quickly moved to the $|\uparrow, \mathrm{S}(1,1)\rangle$ state where it precesses with $|\uparrow, \mathrm{T}_0(1,1)\rangle$ for the qubit evolution time τ_c before undergoing a Pauli spin blockade measurement deep in the (1,0,2) region [63]. The cycle duration is set to 15.192 µs independent of τ_c by adjusting the initialization time. The next level is a "record", which comprises 250 consecutive cycles with qubit evolution times increased by 4 ns steps, restarting each record from zero. A single record takes time $t_{rec} = 3.8\,\mathrm{ms} = 250 \times 15.192\,\mu\mathrm{s}$ to acquire, covering the qubit evolution for $\tau_c \in [0, 996]$ ns. Finally, we form a set $\mathcal{R}$ by selecting $N_{\mathcal{R}}$ records from all measured ones. We extract the projection of the qubit state on the S-T_0 axis of the Bloch sphere, $s(\tau_c)$, by averaging over data in $\mathcal{R}$, using $s(\tau_c) = \langle 2P_S(\tau_c) - 1\rangle_{\mathcal{R}}$ with $P_S \in \{0, 1\}$ the results of projective measurements of the singlet state as shown in Figure 2.2(a) for a particular record. The simplest, and most standard, choice is to take $\mathcal{R}$ as a block of N consecutive records. The time to acquire such data is $\Delta t = N t_{rec}$, referred to as the *acquisition time*, setting it as the natural parameter for dephasing rates. Indeed, even though we are usually interested in the qubit evolution on times of the order of $\tau_c \lesssim T_2^*$, the acquisition time needed to sample the continuous function $s(\tau_c)$ from binary data of projective measurements is typically orders of magnitude larger, as is clear from the above measurement description.

The time evolution of ΔB_z is first extracted over 40000 consecutive records spanning more than two minutes as shown in Figure 2.2(c)]. It fluctuates around a finite value of 30 MHz, set by the micromagnet, by ±20 MHz due to nuclei. With our measurement sequence we can follow the nuclei dynamics down to the time $t_{rec} = 3.8\,\mu\mathrm{s}$. Namely, using a Bayesian estimation algorithm [64, 65] on the data of a single record, we estimate the mean and variance of the qubit frequency as it evolved during that record. As an example, the Bayesian inference algorithm applied to the record of Figure 2.2(a) is presented on Figure 2.2(b), showing how the probability distribution of the qubit frequency during that record is narrowing as more observations are acquired.

The nuclear spin noise correlator $C_{\Delta B}(\Delta t) = \Delta B^z_{\mathrm{nuc}}(t + \Delta t) - \Delta B^z_{\mathrm{nuc}}(t)$, shown in Figure 2.3(a), displays a clear Gaussian probability distribution which broadens as the acquisition time Δt increases. As shown in Figure 2.3(b), its variance grows as $\sigma_B^2(\Delta t) = D(\Delta t)^\alpha$ over more than three orders of magnitude of timespan, with $\alpha = 0.8$ and $D = 0.048\,\mathrm{MHz}^2/\mathrm{ms}^{0.8}$. Though such long times are not reached in the measurement, the growth has to saturate, at $\sigma_B^2(\infty)$, since the fluctuating Overhauser field is bounded. Taking a value $\sigma_B(\infty)$ corresponding to $T_2^* = 10\,\mathrm{ns}$ typical for dots comparable to ours [61], we can roughly estimate the nuclear decorrelation time as $(\sigma_B^2(\infty)/D)^{1/\alpha} \approx 107\,\mathrm{s}$.

Interestingly, the exponent $\alpha < 1$ indicates a sub-diffusive behaviour. This differs from the normal diffusion (corresponding to $\alpha = 1$) that is assumed for dipole-dipole interactions that should dominate at times equal or larger than our t_{rec}, as discussed previously, and super-diffusion expected for electron-mediated interactions which should dominate at much shorter times [66]. Non-Markovian nuclear dynamics could result in such sub-diffusion [67], it would however also imply a non-Gaussian noise correlator [68], at odds with the observations. Since it is difficult to infer the correlator functional form in the time domain from its noise power spectrum [69] if the latter is known only within a limited frequency range, other investigations [70–72] do not necessarily contradict our observation (in these works, the lorentzian shaped power spectral density of a normal diffusion process is fitted). It is to be noted that a behaviour closer to standard diffusion cannot be completely excluded at the shortest times that have been reached where the correlator variance appears to bend slightly towards the $\alpha = 1$ slope. A similar approach to extract

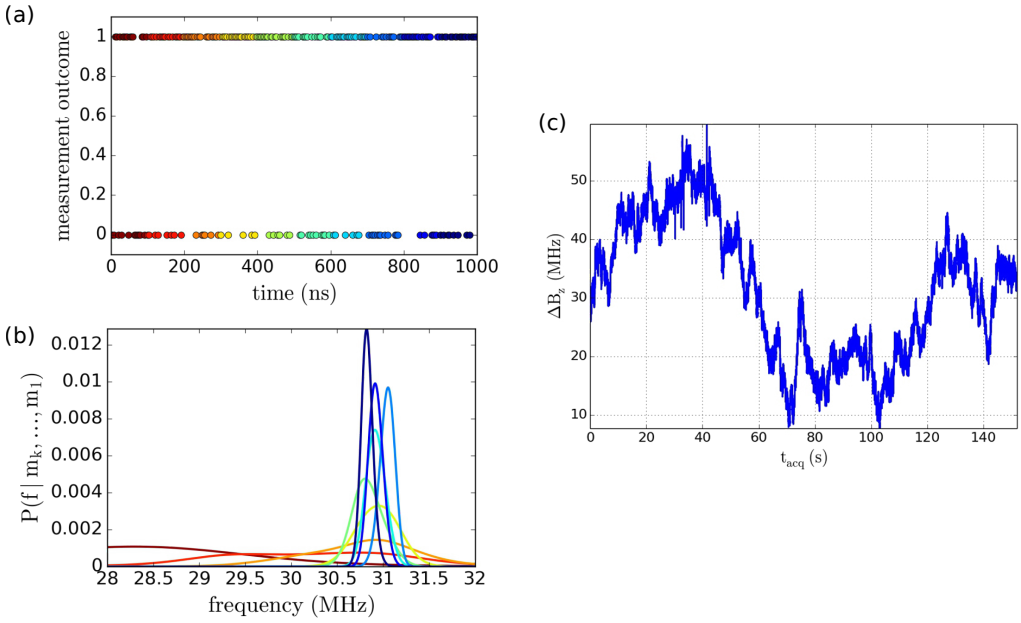

Figure 2.2: (a) Typical record showing the results of the projective measurements P_S of the qubit as a function of the qubit evolution time. (b) Probability distribution of the qubit frequency calculated with Bayesian inference from the record in (a). The color code shows how the probability distribution narrows down as the qubit evolution time increases and more observations are used. (c) Nuclear field gradient $\Delta B_z(t)$ extracted from the qubit frequency as a function of time.

the correlator variance was used also with a ST qubit in GaAs where $\alpha = 1$ is reported for times between ≈ 1 ms and 50 ms [65]. This could indicate that normal diffusion occurs at time scales shorter than anticipated.

The measurement of the Overhauser field variance correlator as a function of acquisition time has been reproduced in two other experiments. In the first one, a ST qubit was also used and manipulated in the same manner (initialization, operation and readout) [54] and in the second one, a different type of qubit was manipulated, a spin-1/2 spin qubit [73]. In both of these two subsequent works, the GaAs wafer is identical but it is different from the one used in the previously described work [1]. The corresponding variance correlators, shown in Figure 2.3 (c) and (d), both exhibit a subdiffuse behaviour with $\alpha = 0.8$ [54] and $\alpha = 0.84$ [73]. The reproducibility of the subdiffusive behaviour with different wafer and type of qubit is encouraging to exclude a material origin or a difference of hyperfine interaction between a singlet-triplet state and a spin-1/2 state. In addition, in the ST qubit case, the frequency fluctuations of the qubit come from the difference of the nuclear spin magnetic field at two different quantum dot locations while for the spin-1/2 qubit, they come from the nuclear spin magnetic field in a single quantum dot. This difference does not appear to have any consequence on the variance correlator of the noise. One difference between this set of experiments and the experiments done by other groups is the presence of the micromagnet which induces magnetic field gradients $\Delta B^z_{\mathrm{MM}}(y)$ and $\Delta B^x_{\mathrm{MM}}(z)$ as described in subsection 1.1.1, with the the x-axis out of plane, the y-axis oriented along the quantum dot alignment and the z-axis in-plane as in Figure 2.1. However, taking the micromagnet field into account would not lift the difficulty to infer the fluctuation mechanism without assuming normal diffusion.

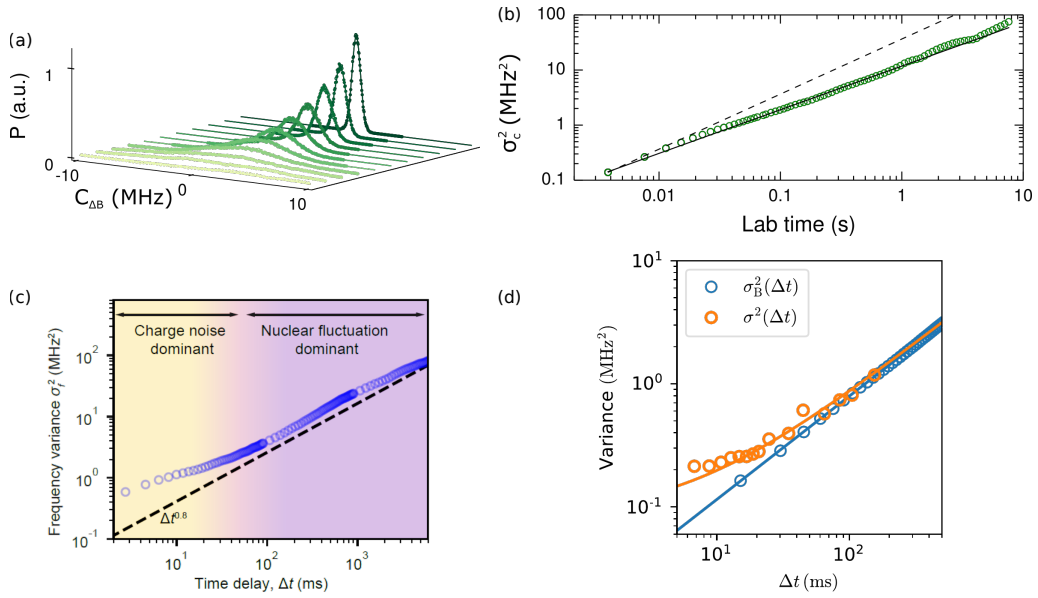

Figure 2.3: (a) The probability distribution of the nuclear field gradient time correlator $C_{\Delta B}(\Delta t)$ for acquisition time Δt from 3.8 ms (dark green) to 7.6 s (yellow). Data (dots) are fitted with a Gaussian distribution (line). Variance of the nuclear field gradient correlator as a function of the acquisition time Δt. The solid line is a fit showing a growth with a power law exponent $\alpha = 0.8$. The dashed line shows a power law behavior with $\alpha = 1$ for comparison. The variance of the nuclear field gradient correlator as a function of the acquisition time Δt measured with a ST spin qubit in a different wafer (c) (taken from the supplementary material of Ref. [54]) and in a different wafer with a spin-1/2 qubit (blue dots, taken from Ref. [2]).

We now turn to the qubit phase stability. The standard way is to fit the qubit state estimation evolution to oscillations with a Gaussian decay

$$s(\tau_c) \xrightarrow{\text{fit}} \cos(2\pi f_0 \tau_c) \exp\left[-\left(\frac{\tau_c}{T_2^*}\right)^2\right], \tag{2.18}$$

and define the dephasing time as the fitted decay parameter. If τ_c is much smaller than the acquisition time, always fulfilled, the frequency change during the time τ_c is negligible and we get

$$s(\tau_c) = \frac{1}{N_{\mathcal{R}}} \sum_{r \in \mathcal{R}} \cos\left(2\pi f_{c,r} \tau_c\right), \tag{2.19}$$

with $f_{c,r}$ the qubit frequency during the c-th cycle of the r-th record. From here it follows that the frequency and dephasing extracted from the fit in Eq. (2.18) are given, respectively, as the average and the variance of the set of frequencies $\{f_{c,r}\}$. These statistical properties in turn depend on how the set $\mathcal{R}$ is chosen.

The standard way is to choose $\mathcal{R}$ as a single block of N consecutive records. Doing so defines $T_{2,\phi}^*$, for which is observed a gradual increase of $T_{2,\phi}^* \sim 120$, 220 and 570 ns upon decreasing N, for respective acquisition times $\Delta t \sim 1.6$, 0.4 and 0.1 s as shown in Figure 2.4(a). Since each of these qubit evolutions results from a particular noise realization, T_2^* becomes a stochastic variable itself. It is possible to extract its probability distribution for various acquisition times, as shown in Figure 2.4(b). It is always well fitted

by a Gamma distribution[3] whose skewness does not significantly change for Δt varying from 38 ms to 7.6 s. The shape parameter of the fitted Gamma distribution is $k = 7.25 \pm 1$ over this range. This robustness can be interpreted as a signature that the nature of the underlying dynamics of nuclei does not change within this timespan. A Simulation of the whole measurement sequence with an Ornstein-Uhlenbeck normal diffusion process at all time scales similarly gives $T^*_{2,\phi}$ distributed according to a Gamma distribution with a larger skewness corresponding to $k = 5.5 \pm 0.6$ over the same time span. The conclusion of this statistical analysis is that a single trace is not sufficient to reliably estimate the phase decay, as the most probable $T^*_{2,\phi}$ is smaller than the mean $\overline{T^*_{2,\phi}}$, whereas occurrences of $T^*_{2,\phi}$ several times larger than $\overline{T^*_{2,\phi}}$ are common.

Is it therefore enough to measure as fast as possible with respect to the decorrelation time of the environment noise to improve the dephasing time? Of course not as the full variance of the noise $\sigma^2_B(\infty)$ is still hidden in the unknown value of the Overhauser field, hence the actual qubit frequency, at the beginning of the qubit operation. Therefore the dephasing time $T^*_{2,\phi}$, although much larger than $T^*_2(\infty) \approx 10$ ns, is useless for quantum information manipulation. For practical quantum computation (QC) the qubit frequency must be known in advance. This can be done using the Bayesian approach described here on a first record before the actual qubit operations. The corresponding dephasing time $T^*_{2,QC}$ is found to increase to ~ 600 ns on average for an acquisition time of a single record ($N = 1$) corresponding to 3.8 ms. While for large N a Gamma distribution similar as the one for $T^*_{2,\phi}$ was observed as expected, statistics of $T^*_{2,QC}$ for acquisition times shorter than 10×3.8 ms could not be estimated due to the lack of total number of records, limited by the physical memory of the digitizer acquisition board. With at least 10 times more records, it could have been possible to obtain statistics at such short time scale. We will now turn in the beginning of the next section to a practical implementation of $T^*_{2,QC}$ with a spin-1/2 spin qubit in GaAs.

2.3 Fighting against nuclear spins dephasing

This section discusses results published in Ref. [2–5].

In the previous two sections we have seen how the nuclear spins environment influences in a detrimental way the dephasing time of the spin qubit and how it can induce non trivial statistics of the dephasing time itself. As the fluctuations we have investigated are slow with respect to the qubit actual operation time, such noise is classified as quasi-static. We have thus seen that operating fast with respect to the noise decorrelation time can in principle significantly improve the dephasing time, according that the environment is monitored just before operation, doing a so-called Hamiltonian estimation. This is discussed in the following subsection. Reducing the number of nuclear spins by changing the host material and performing isotopic purification is the second approach as discussed in section 2.1 which will be the subject of the following subsections. Typically using both approaches, the remaining dominant source of noise becomes charge noise, larger than the high frequency component of the nuclear spin noise.

[3]The Gamma distribution of a variable X is defined by $G_X(x;k,h) = \frac{(2k/h)^k}{2^k\Gamma(k)} x^{k-1} e^{-\frac{k}{h}x}$ with Γ the Euler function, h the mean and k is the shape parameter related to the distribution skewness $\gamma_1 = 2/\sqrt{k}$. Details of the fit procedure can be found in the supplementary material of Ref. [1]

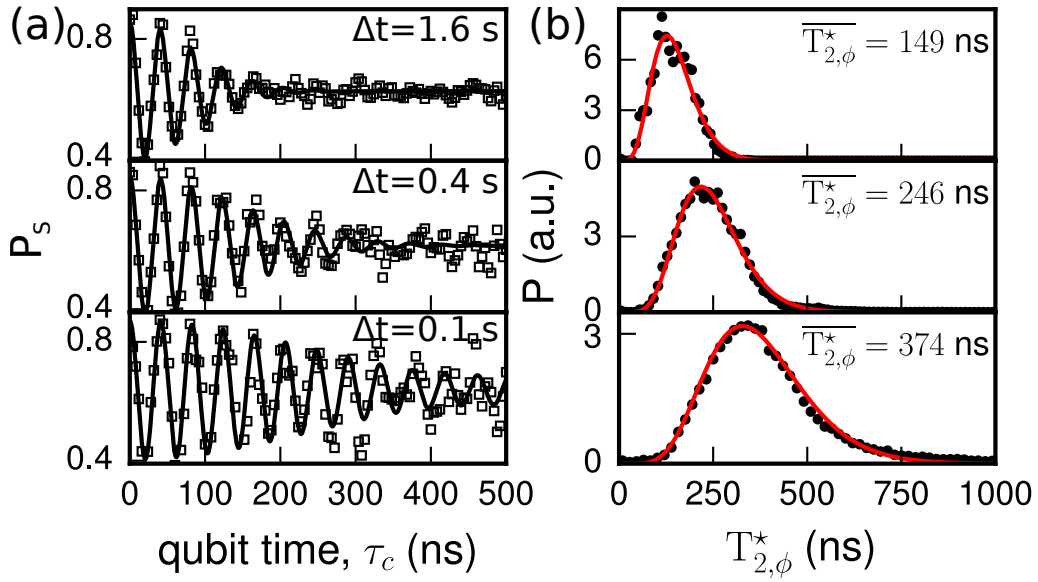

Figure 2.4: (a) Typical qubit evolution traces for different acquisition times. Solid lines are fit to decaying oscillations giving $T^*_{2,\phi} = 120$, 220 and 570 ns respectively. (b) Probability density distributions of $T^*_{2,\phi}$ corresponding to the same acquisition times as for (a). The red solid line is a fit to a Gamma distribution resulting in skewness $\gamma_1 \approx 0.75$, and $\overline{T^*_{2,\phi}} \approx$ as given.

While the improvement of the dephasing time is the primary target, one should not forget that the actual goal is to develop a qubit useful for quantum computation. A good figure of merit to quantify how good a qubit is for this purpose is the qubit quality factor, defined as $Q = 2 f_{\text{Rabi}} T_2^{\text{Rabi}}$ which simply tells how many of the simplest quantum gate (a π-rotation gate) can be done during the dephasing time. Here f_{Rabi} is the Rabi frequency and T_2^{Rabi} is the Rabi dephasing time, usually larger than the free induction decay time T_2^* discussed in the previous section due to the qubit being actively driven [74]. Importantly, the quality factor sets an upper limit on the fidelity $\mathcal{F}$ of the simplest single quantum gate as $\mathcal{F} \leq e^{-1/Q}$. As fault tolerance requires gate fidelities of at least about 99% [75], this imposes a lower bound of 100 on the qubit quality factor for practical quantum computation. Therefore it is also essential to not forget about the qubit frequency. This is why in GaAs and silicon based devices a micromagnet is used to exploit EDSR which enhances single spin-1/2 qubit drive frequencies. GaAs is for once naturally better than silicon due to the presence of an intrinsic not so small spin-orbit interaction which naturally induces larger qubit operational frequencies than in silicon where the spin-orbit interaction is weak. We shall keep those elements of thoughts in mind throughout the rest of this section.

2.3.1 Hamiltonian estimation in GaAs

All figures of this section are taken and adapted from Ref. [2].

The prolongation of the dephasing time by exploiting the low frequency quasi-static noise has been demonstrated with a ST qubit in GaAs, using Hamiltonian estimation as described in the previous section, giving an impressive enhancement of $T_2^* \sim 2\,\mu\text{s}$ [65]. In this work, the Hamiltonian estimation was used to evaluate the stability of the idle qubit frequency through the measurement of T_2^*. Here "idle" means that only the free induction

decay of the qubit is measured with a Ramsey sequence. This was highly instructive on the effective enhancement of the dephasing time using Hamiltonian estimation technique. However, for practical quantum computation, one needs to actively control the qubit, typically performing Rabi control. This is why we implemented a similar approach with a single spin-1/2 qubit. The differences with the work of Ref. [65] are threefold : (1) the feedback protocol has to be changed with respect to ST qubit. (2), the Overhauser field couples differently to the spin qubit, through its local value rather than to its spatial gradient as discussed in the previous section. (3), as the single spin-1/2 qubit will be driven, we will investigate the enhancement of the driven qubit performances through T_2^{Rabi} and be able to access the qubit noise at the Rabi frequencies, orders of magnitude larger than the typical Overhauser field frequency range we have discussed so far.

Regarding point (1), a ST qubit is naturally precessing at the qubit frequency f_{qubit} set by the local gradient of the external magnetic field and the Overhauser field. Estimation of f_{qubit} with Bayesian inference is done by leaving the qubit evolve for a time t_R. For a spin-1/2 qubit, it is necessary to drive the qubit to the Bloch sphere equator where it evolves under the qubit frequency $f_{\mathrm{qubit}} = g\mu_B(B_{\mathrm{ext}} + B_{\mathrm{nuc}})/h$ set by the total external magnetic field B_{ext} plus the Overhauser field B_{nuc}. Therefore, estimating the qubit frequency necessitates to perform a Ramsey measurement, whose protocol and sequence is described in Figure 2.5(b). Ramsey oscillations are measured by doing two $\pi/2$ Rabi pulses separated by a time t_R. The Rabi pulses are done by driving the qubit at f_{qubit} for a time $1/f_{\mathrm{Rabi}}$. To observe Ramsey oscillations at frequency Δ in the qubit rotating frame, it is necessary to actually drive the qubit off resonant at $f_{\mathrm{MW}} = f_{\mathrm{qubit}} + \Delta$. We therefore see how the feedback protocol can be implemented alternating "probe" and "target" steps (see Figure 2.5(c)). In the former, the qubit frequency is probed by sampling 150 qubit measurement outcomes of a Ramsey oscillation with $t_R = 2, 4, \ldots, 300\,\mathrm{ns}$ using $f_{\mathrm{MW}}^{n-1}(\Delta) = f_{\mathrm{qubit}}^{\mathrm{est,n-1}} + \Delta$ at the $(n-1)$ repetition of the feedback sequence. Bayesian inference algorithm is applied in real time using a Field Programmable Gated Array (FPGA) board to estimate $f_{\mathrm{qubit}}^{\mathrm{est,n}}$ setting $f_{\mathrm{MW}}^{n}(\Delta) = f_{\mathrm{qubit}}^{\mathrm{est,n}} + \Delta$. The subsequent "target" step begins afterwards using $f_{\mathrm{MW}}^{n}(\Delta)$ with either keeping $\Delta \neq 0$ to perform again Ramsey oscillations or setting $\Delta = 0$ to perform a Rabi drive of the qubit.

Keeping $\Delta = 50\,\mathrm{MHz}$ for performing Ramsey oscillations allows for validating the suppression of the electron spin qubit dephasing. Time traces of the frequency detuning between the applied qubit frequency f_{qubit} and the estimated qubit frequency $f_{\mathrm{qubit}}^{\mathrm{est}}$ with and without feedback are shown in Figure 2.6(a) demonstrating a clear stabilization with feedback control on. The variance of the nuclear field induced fluctuations falls from $\sigma_{B,\mathrm{off}}^2 = (7.92\,\mathrm{MHz})^2$ to $\sigma_{B,\mathrm{on}}^2 = (0.29\,\mathrm{MHz})^2$. Equivalently, this can be measured by evaluating T_2^* from Ramsey oscillations which increases from $T_{2,\mathrm{off}}^* = 28.4\,\mathrm{ns}$ to $T_{2,\mathrm{on}}^* = 766.7\,\mathrm{ns}$. Interestingly the 27-fold enhancement of T_2^* is in line with the 29-fold enhancement that was measured with the ST qubit [65]. Finally, it seems to be only limited by the feedback hardware as the value of $\sigma_{B,\mathrm{on}}^2$ starts to saturate for short timescales (see Figure 2.3(d)) at a value close to the bin width of the frequency discretization (0.25 MHz) of the Bayesian estimation algorithm.

Setting $\Delta = 0$, Rabi oscillations can be performed, a typical measurement of which is presented in Figure 2.6(c). It shows an exponential decay, which is common for silicon spin qubits [3, 4] but atypical for GaAs [77] as it implies $1/f$ noise (usually charge noise) rather than $1/f^2$ noise associated with nuclear spin "diffusion". $T_2^{\mathrm{Rabi}} \approx 1.5\,\mu\mathrm{s}$ is found for the trace shown. From this point, the quality factor $Q = 2f_{\mathrm{Rabi}}T_2^{\mathrm{Rabi}}$ is optimized, adjusting f_{Rabi} through the microwave drive amplitude as well as the strength of the spin-electric

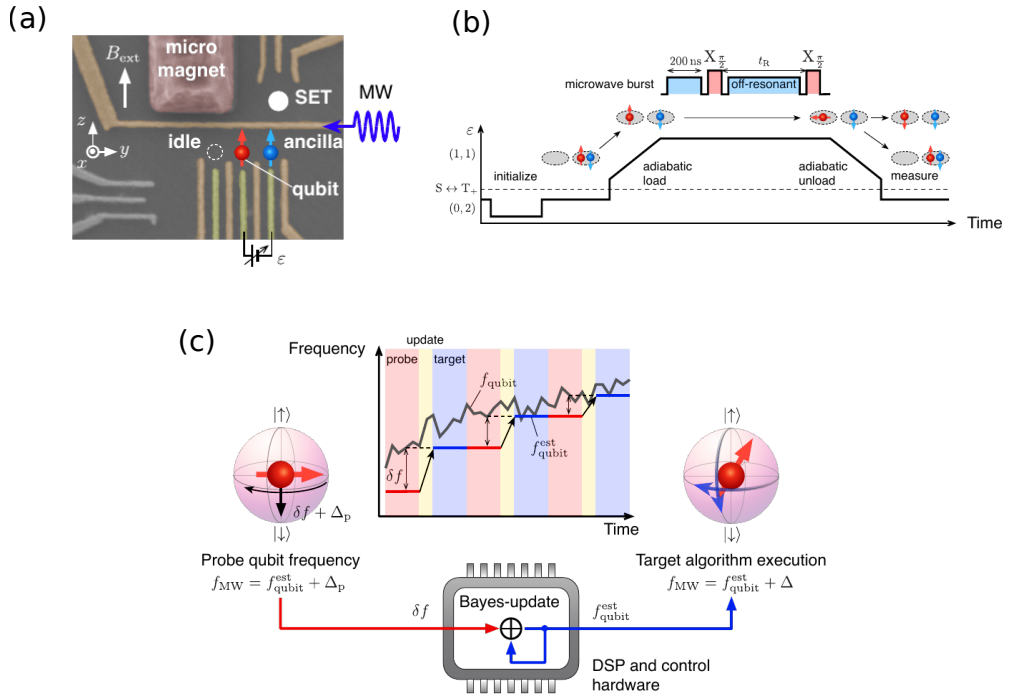

Figure 2.5: (a) False-colored scanning electron micrograph image of the TQD device. An electron spin qubit in the middle QD (red arrow with a circle) is controlled by the EDSR where the spin is coupled to a microwave (MW) electric field via a stray magnetic field of the micromagnet deposited on the wafer surface. The right QD hosts an electron spin (blue arrow with a circle) used as a readout ancilla while the left QD hosts another electron which is unused and decoupled from the two spins. The energy detuning between the middle and the right QDs ϵ is gate-tunable and the QD electron occupancies are probed by a proximal single-electron transistor (SET) [76]. (b) Schematic of the Ramsey measurement. Two electrons (qubit and ancilla) are initialized to a doubly-occupied singlet state in the right QD and an up-spin qubit is prepared by adiabatically loading one of the electrons to the middle QD [20]. Two $\pi/2$ microwave bursts, separated by time t_R, are applied (before and during these, off-resonant microwave bursts are optionally applied). The ancilla-spin state is not affected by the microwave bursts. The final state is read out by unloading an up-spin (anti-parallel to the ancilla) state from the middle QD while a down-spin (parallel to the ancilla) state remains blocked. (c) Schematic of the feedback control loop for a spin qubit. Data of a Ramsey oscillation are processed in a digital signal processing hardware with programmable logic (FPGA) to estimate the frequency detuning $\delta f = f_{\text{qubit}} - f^{\text{est}}_{\text{qubit}}$ between the current qubit frequency fqubit and its previous estimate $f^{\text{est}}_{\text{qubit}}$ ("probe" step). The value of $f^{\text{est}}_{\text{qubit}}$ is updated to $f^{\text{est}}_{\text{qubit}} \to f^{\text{est}}_{\text{qubit}} + \delta f$ ("update" step), after which the target experiment follows ("target"step). In the ideal case, the subsequent qubit algorithms can be executed with a microwave frequency f_{MW} matching fqubit exactly (by choosing $\Delta = 0$).

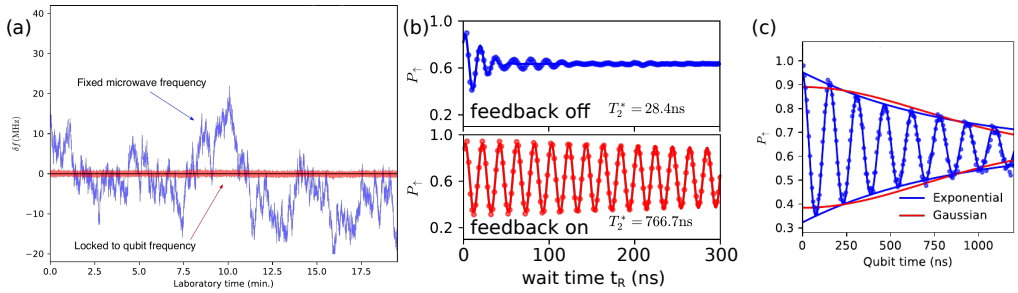

Figure 2.6: (a) Time dependence of the frequency detuning $\delta f = f_{\text{qubit}} - f_{\text{qubit}}^{\text{est}}$ extracted from Ramsey measurements. The blue trace is taken with a fixed f_{MW} (no feedback) and the red trace is taken with a feedback controlled f_{MW}. (b) Up-spin probability $P_\uparrow$ as a function of t_R. The upper panel shows the trace obtained when the feedback is off. The decay envelope gives the dephasing time of $T_2^* = 28.4\,\text{ns}$. The upper panel shows the trace obtained with the feedback on ($\Delta = 50\,\text{MHz}$). The envelope of the oscillation is a Gaussian decay function with $T_2^* = 767\,\text{ns}$. (c) Rabi oscillations obtained at zero detuning upon compensating for the induced shift Δf_{qubit} showing an exponential decay function with $T_2^{\text{Rabi}} \sim 1.5\,\mu\text{s}$.

coupling through the detuning energy between the two neighbouring quantum dots [14]. A highest $Q = 85 \pm 8$ was achieved in this device, setting an upper single qubit gate fidelity $\mathcal{F} \leq 98.8 \pm 0.1\%$. This prediction was tested using randomized benchmarking [78], finding an X_π gate fidelity of $99.04 \pm 0.23\%$ close to the Q-factor limited value, and setting the highest fidelity for single spin qubits in GaAs to date, above the fault tolerant threshold of 99% [75]. The other single qubit gates show a lower fidelity of 97.5% on average, most likely limited by systematic unitary errors due to the microwave setup. We note however that these still fall above the fault tolerance threshold of 95% of new quantum error correction codes, assuming that dephasing noise is significantly larger than relaxation noise [79], which is most probably the case with this type of spin qubits.

Interestingly, the dependence of T_2^{Rabi} with f_{Rabi} offers a direct way to investigate the dephasing noise at frequencies order of magnitude larger than for the quasi-static Overhauser noise. The power spectral density $S(f)$ in the low frequency range is computed by Fourier transform of the data in Figure 2.6(a) while it is calculated from the exponential decay rate of the Rabi oscillations for higher frequencies [80, 81]. Both are plotted on the same graph in Figure 2.7(a). When no feedback is active, the low frequency $S(f)$ shows a $1/f^{1.7}$ dependence, as expected from the noise correlator variance dependence in time, as the exponent of the former is half the exponent of the latter ($\sigma_N^2(t) \propto t^\alpha \leftrightarrow S(f) \propto 1/f^{2\alpha}$) [82]. As the feedback is turned on, the spectral density is significantly suppressed with a flat noise spectrum region suggesting uncorrelated white noise turning to a $1/f$ noise more visible as the spin-electric-coupling is increased (red curve), typical of charge noise [4]. The noise power spectral density extracted from the Rabi measurements at $f \approx 10\,\text{MHz}$ strikingly falls on the same $1/f$ noise line, highly suggestive of a charge noise dominated dephasing of the qubit over 6 orders of magnitude, which was again a first in a 100% nuclear spins material like GaAs. Despite the charge noise character of $S(f)$ at high frequencies, nuclear spins are still lurking around. The noise power spectral density extracted from the Rabi measurements is displayed in Figure 2.7(b). For $f < 20\,\text{MHz}$, $S(f)$ shows three prominent peaks, on top of the $1/f$ baseline, at the nuclear Larmor precession frequencies of ^{75}As, ^{69}Ga and ^{71}Ga. It clearly suggests that such high frequency noise sources indeed

influence the Rabi decay of the spin qubit. The qubit spin quantization axis is defined by the external magnetic field along the z-axis. The Overhauser field aligns along the same z-axis and when nuclear spins precess around it, it remains constant and there is no noise at the Larmor frequencies. In the present device, the stray field of the micromagnet induces field inhomogeneity, making each nuclear spin (indexed by k) at position $\boldsymbol{r}_k$ precess around a local magnetic field vector $\boldsymbol{B}(\boldsymbol{r}_k)$ slightly off the z-axis (see the inset of Figure 2.7(b)). The inhomogeneity of the nuclear spin polarization leads to small but finite residual oscillations of Overhauser field at the nuclear precession frequencies.

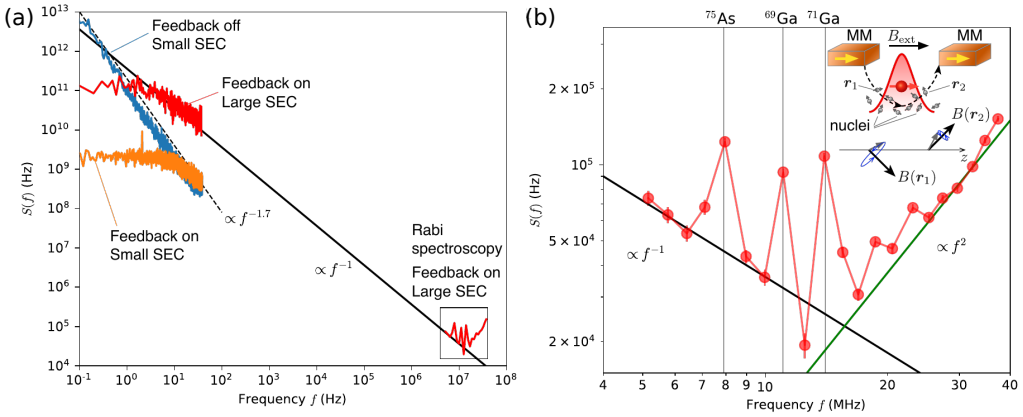

Figure 2.7: (a) Power spectral density $S(f)$ of the longitudinal noise in f_{qubit} from Ramsey measurements of Figure 2.6(a) for $f < 10^3$ Hz and from Rabi measurements for $f > 10^6$ Hz (black boxed red curve). (b) Zoom on the power spectral density $S(f)$ of the longitudinal noise extracted with Rabi drive. Vertical grey lines show Larmor precession frequencies for the three nuclear species, ^{75}As, ^{69}Ga and ^{71}Ga calculated with the micromagnet -induced field component of $B_z^{\text{MM}} = 70\,\text{mT}$. The inset illustrates electron-nuclear spin coupling in an inhomogeneous magnetic field. Each nuclear spin is randomly oriented and precesses around a local magnetic field vector $\boldsymbol{B}(\boldsymbol{r}_k)$, leading to an oscillatory Overhauser field in the z direction.

2.3.2 Natural and isotopically purified silicon

All figures of this section are taken and adapted from Ref. [2–4]

We will now discuss spin qubit dephasing performances as the proportion of nuclear spins is decreased in order to reduce the Overhauser noise, using as host materials natural silicon [3] and isotopically purified silicon [4]. As the qubit operations are similar to the ones already presented and no complex feedback protocol is needed, we will keep the description of the results short and focus on the comparison between the different implementations of spin qubits in regard of the various figure of merits. Previous implementations of single spin qubits in natural silicon had shown a significant improvement over GaAs spin qubits, with $T_2^* \sim 800\,\text{ns}$ [83]. This value is however relatively less than the expected value presented in Table 2.2. This rather large dephasing could be explained by a rather large charge noise in this particular device. In addition, the spin qubit suffered from the presence of the silicon valley degree of freedom whose degeneracy was not lifted enough, impeding the qubit operations. Even though they used a micromagnet to enhance the control frequency of the qubit to $f_{\text{Rabi}} \sim 5\,\text{MHz}$, they could only achieve a quality factor of $Q \sim 9$. This indicated that fully exploiting the potential of the lower concentration of

nuclear spins of silicon is more difficult than anticipated. This amounts principally to a more delicate fabrication process, the quality of the two-dimensional electron gas and the presence of the valley degree of freedom when compared to GaAs. The latter can be lifted simply by designing smaller quantum dots to sets the energy spacing between the two valleys at values much larger than temperature and qubit energy (we should recall however from Eq. (2.16) that smaller dots at constant nuclear spin concentration is detrimental for the dephasing time).

This is what was implemented in our natural, industrial standard, silicon spin qubit in RIKEN (see Figure 2.8(a)) [3], with an emphasis on properly designing the micromagnet to optimize the qubit control frequency [19]. Low charge noise and the absence of the spurious valley degree of freedom allowed for observing dephasing times in line with expectations $T_2^* \sim 2\,\mu s$ (see Figure 2.8(b)), two orders of magnitude larger than in GaAs. Consequently, Rabi decoherence times of $T_2^{\text{Rabi}} \sim 10\,\mu s$ where observed, which coupled to an optimized large control frequency of the qubit $f_{\text{Rabi}} \sim 5\,\text{MHz}$ allowed to reach quality factors of $Q \sim 140$. This in turn allowed for reaching fault tolerance single qubit gates with an average fidelity of 99.59%. Remarkably, this is similar to quality factors ($Q \sim 80-140$) and fidelities ($\mathcal{F} = 99.57\%$) of previously demonstrated single spin qubits in isotopically purified silicon [10, 11]. While the isotopic purification allowed for reaching the expected nuclear spin limited dephasing times of $T_2^* = 120\,\mu s$, these works suffered from low qubit control frequency of $f_{\text{Rabi}} \sim 100\,\text{kHz}$ due to the absence of an efficient spin to charge conversion mechanism. It is therefore natural to use a similarly optimized micromagnet with istopically purified silicon to try to obtain a better qubit than with natural silicon. The isotopically purified silicon wafer was provided by the group of Kohei Itoh from Keio university who also provided previous wafers to New South Wales University [10, 11]. With the micromagnet, we could reach Rabi frequencies about two orders of magnitude larger $f_{\text{Rabi}} \sim 30\,\text{MHz}$. However at these frequencies, the Rabi coherence time degrades (this will be discussed in a few paragraphs) and $f_{\text{Rabi}} \sim 3\,\text{MHz}$ has to be chosen for keeping long coherence times of $T_2^{\text{Rabi}} \sim 110\,\mu s$ giving an optimized qubit quality factor of $Q \sim 888$ and the corresponding single qubit gate fidelities of $\mathcal{F} > 99.9\%$. As a matter of comparison, these record metrics for a single spin qubit compare with Google's superconducting qubits ($Q \sim 1000$, $f_{\text{Qubit}} \sim 20\,\text{MHz}$) with which "quantum supremacy" was demonstrated in 2019 [84].

An interesting aspect of the enhanced spin to charge coupling in the isotopically purified silicon device is that now charge noise dominates at all frequencies as shown in Figure 2.9, effectively completely removing nuclear spin noise. This is first observed in the dephasing time $T_2^* = 20\,\mu s$ extracted from Ramsey measurement (see Figure 2.8(e)) which is well below the expected theoretical value. Varying the total acquisition time of the Ramsey measurement allows to extract the noise power spectrum over two orders of magnitude in the range $0.01 - 1\text{Hz}$, as in the previous sections. Higher frequency spectral noise density is extracted from Carr-Purcell-Meiboom-Gill (CPMG) protocols [71, 85]. Such dynamical decoupling sequences[4] can partially cancel the dephasing effect, with efficacy strongly dependent on the qubit noise spectral density $S(f)$. The CPMG inferred noise spectral density lies in the frequency range $13-320\text{kHz}$ with a $1/f$ dependence which is in line with the low frequency part. This demonstrates a $1/f$ charge noise over seven orders of magnitude and a purely charge noise limited spin qubit.

From the results discussed so far, we can conclude that "simply" removing nuclear

[4]The CPMG two pulses sequence, $n_\pi = 2$, is the Hahn or spin echo sequence.

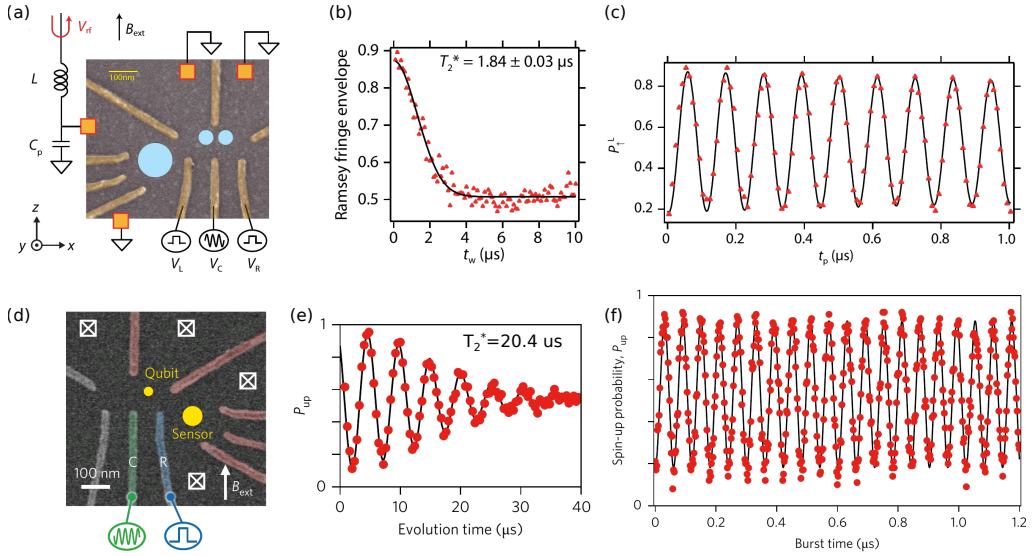

Figure 2.8: (a)–(c) (first row) Natural silicon spin qubit results (from Ref. [3]) and (d)–(f) (second row) isotopically purified silicon spin qubit results (from Ref. [4]). The two devices are very similar, except for the host material, and are presented in (a) and (c) as false colored micrographs. The square boxes in orange (a) or white (b) represent the ohmic contacts. The small circles show the approximate position of the quantum dot spin qubits while the large circles show the approximate position of the sensor quantum dot. (b) Ramsey fringe envelope of the natural silicon spin qubit driven on resonance showing a $T_2^* = 1.84\,\mu s$ Gaussian decay. (e) Ramsey fringe oscillations of the isotopically purified silicon qubit driven off-resonance showing a $T_2^* = 20.4\,\mu s$ Gaussian decay. (c) Rabi oscillations of the natural silicon qubit with $T_2^{\text{Rabi}} \sim 8\,\mu s$ and $f_{\text{Rabi}} \sim 9\,\text{MHz}$. (e) Rabi oscillations of the isotopically purified silicon qubit with T_2^{Rabi} too long ($\gg 100\,\mu s$) to be estimated from the trace and $f_{\text{Rabi}} \sim 16.6\,\text{MHz}$.

spins to enhance the dephasing time is not enough to make a good practical qubit[5]. The qubit operational frequency is also a very important aspect that was somehow eluded in the community despite the crucial importance of the qubit quality factor which sets an elementary upper bound on the quantum gates fidelities. Improving the qubit frequency is done at the expense of the coherence time as it requires to increase the coupling to the qubit by some means. A compromise has to be taken. This is illustrated in Figure 2.10 where the qubit Rabi frequency, Rabi coherence time and quality factors are presented as a function of the drive amplitude for the natural silicon spin qubit [3] and the feedback controlled GaAs spin qubit [2]. For both, f_{Rabi} grows linearly with the drive amplitude as expected, before departing from this behaviour, most probably due to anharmonicity of the confinement potential of the quantum dot [14]. Again for both, the coherence time T_2^{Rabi} shows a non monotonic behaviour with a maximum value before a decrease at large drive amplitude, most probably due to heating. For the natural silicon spin qubit, as the coherence time is still nuclear spin limited, the Rabi coherence time is roughly saturating at small frequencies, in contrast to the clearly increasing charge noise limited Rabi coherence time in the feedback controlled GaAs spin qubit. As such a careful optimization has to be done to reach the highest quality factor and qubit fidelity.

An important point is that in all the three qubits discussed here, the single qubit

[5]Or a good memory as well because a good memory needs to be written and read fast enough also!

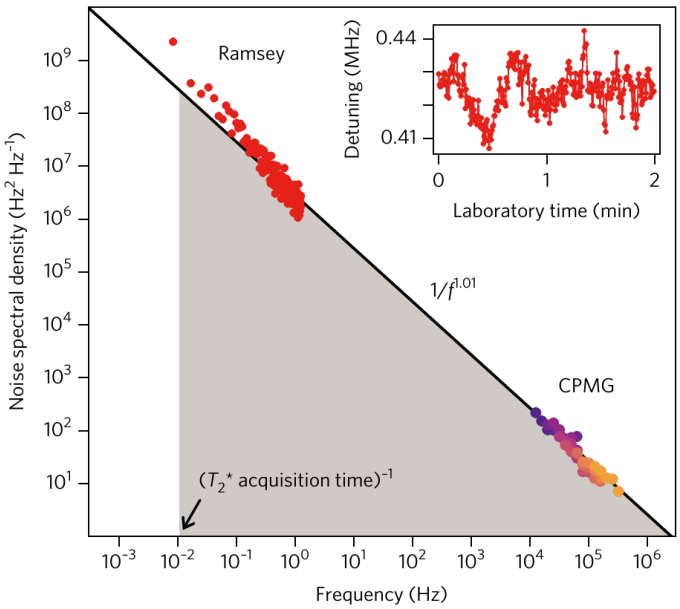

Figure 2.9: Noise power spectral density of the isotopically purified silicon spin qubit. The high frequency data points are extracted from dynamical decoupling sequences and the low frequency points are extracted from Ramsey oscillations measurement over 24 minutes, similarly to the feedback controlled GaAs spin qubit. The solid line corresponds to $S(f) \propto 1/f^{1.01}$. The inset shows typical fluctuations of the qubit frequency detuning over 2 minutes.

fault tolerance threshold $\mathcal{F} \geq 0.99$ based on surface code quantum error correction (QEC) [75] has been demonstrated. QEC relies on scaling errors exponentially with polynomial number of operations (gates). The isotopically purified spin qubit has a quality factor ten times larger than the feedback controlled GaAs spin qubit $Q_{^{28}\mathrm{Si}} \sim 10 Q_{\mathrm{GaAs}}$ so its base error rate is ten times smaller. However, we have also seen that the operation speed of the ^{28}Si spin qubit is ten times smaller $f^{\mathrm{Rabi}}_{\mathrm{GaAs}} = 33\,\mathrm{MHz} \sim 10 f^{\mathrm{Rabi}}_{^{28}\mathrm{Si}}$ with $f^{\mathrm{Rabi}}_{^{28}\mathrm{Si}} = 3\,\mathrm{MHz}$. Therefore it is not completely clear that within the same operation time (including the time needed to perform QEC), the feedback controlled GaAs spin qubit does not reach comparable error rates as the ^{28}Si spin qubit due to the exponential scaling. One could argue that the feedback operation adds complexity but this would probably be at most (and probably less) comparable with the computational requirements of performing QEC. Ultimately, QEC as it is envisioned at the moment cannot be handled with the current classical technology (due to to constrains on the amount of data to be processed on the short coherence times of the qubits). Most probably, it would have to be dealt with on-chip cryogenic CMOS-like components [86]. And as of now, none of the spin qubits discussed so far are actually CMOS compatible, even the silicon ones. Regarding this technological barrier, CMOS silicon spin qubits are promising although their metrics need to be boosted to reach the fault tolerance threshold despite promising qubit operation frequencies of several tens of MHz [87]. We will now put an end to our small venture on the slippery slopes of practical quantum computation and get back to more basic concerns regarding the development of spin qubits with carbon nanotubes.

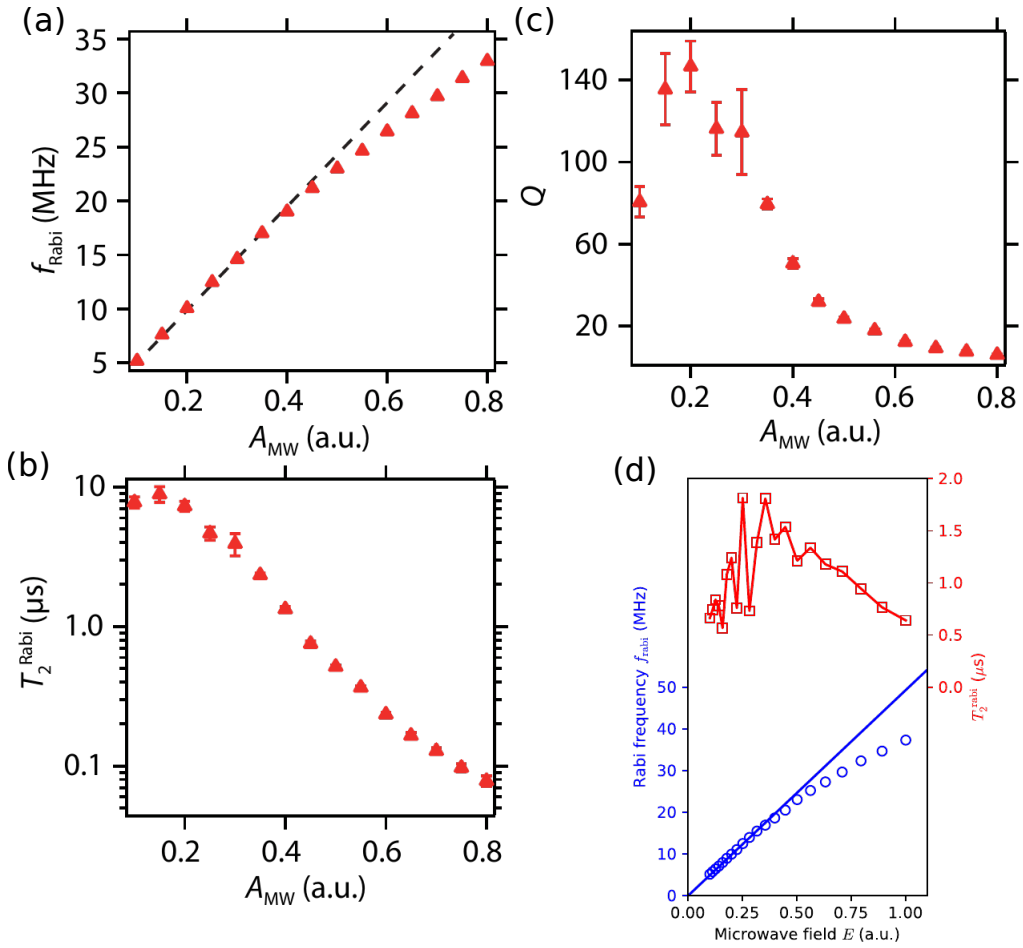

Figure 2.10: Evolution of Rabi frequency f_{Rabi} (a) and dephasing time T_2^{Rabi} (b) as a function of the driven amplitude for the natural silicon spin qubit. In (b), the dashed line is a linear fit to the data a small driving amplitude. (c) Natural silicon spin qubit quality factor showing an optimum at small driving amplitude. (d) Evolution of Rabi frequency f_{Rabi} and dephasing time T_2^{Rabi} as a function of the driven amplitude for the feedback controlled GaAs spin qubit of subsection 2.3.1.

2.3.3 Natural carbon CNT in a microwave cavity

This section discusses results published in Ref. [5]

In section 2.1 we saw that carbon nanotubes (CNT) hold great promises in terms of nuclear spin dephasing, even better than silicon. However, realizations of valley-spin qubits[6] in CNT have revealed surprisingly short dephasing times of the order of ten nanoseconds [88, 89]. The conclusion was that the hyperfine interaction in CNT would be two orders of magnitude larger than what is theoretically expected [47, 48] and what has been measured with fullerenes [90]. One possible explanation for this important dephasing could be large charge noise mediated by the valley degree of freedom, and interdot exchange [89]. However, these qubits showed promising operation frequencies in the range of several tens

[6]These qubits exploit the valley degree of freedom of CNT for spin-to-charge coupling and a bend in the CNT to get effectively two non collinear magnetic field axis, in a similar fashion to the non-collinear ferromagnet leads discussed in subsection 1.1.2

of MHz. It is thus important to develop other types of CNT spin qubits, not based on valley-spin coupling, to try to observe and exploit their potential long coherence times. The approach we take is based on non-collinear ferromagnetic leads double quantum dot, as discussed in subsection 1.1.2, embedded in a microwave cavity [22]. One reason to use a microwave cavity in a circuit quantum electrodynamics (cQED) architecture [91, 92] is because CNTs are inherently one dimensional. While it is possible to build several spin qubit devices in a row on a single CNT, it is quite unrealistic to envision a two-dimensional network built out of CNTs. However, such a two-dimensional array of qubits is required for scalability, both for space occupation and the implementation of QEC codes like the surface code [75]. Another interest of using cavities is that they can enhance qubits lifetime, acting as narrow bandpass filters, through inverse Purcell effect [92, 93]. We will not go into the details of mesoscopic cQED or "mQED" in this short manuscript as it will not be necessary for the coming discussions (there are now several in-depth reviews that describe the field [94, 95]).

Spin qubits in microwave cavities have been demonstrated in various materials, first in CNT [24] with the demonstration of a coherent coupling of the qubit to the cavity photons, then in Si [25, 26, 96] and GaAs [97], all reaching the so-called strong coupling regime where the spin-photon coupling g_s exceeds the qubit and photon loss rates γ and κ respectively. The strong coupling regime consisted in a milestone in the field as it is required to coherently manipulate the qubit with the photons (the slightly weaker coherent coupling of Ref. [24] is actually already enough). The natural (or magnetic) single spin-photon coupling in a cavity is of the order of 10 Hz [98]. As the spin qubit decoherence rate obtained in these architecture is of about 1 MHz, it means that the effective spin-photon coupling has been boosted by five orders of magnitude using spin-electric-coupling as described in section 1.1 (the work of Ref. [97] used another type of qubit, an exchange-only qubit [99], which presents a very large electric dipole and a qubit control purely relying on exchange interaction which does not require local magnetic fields). We will come back in the following to the interplay between the charge and spin character of the qubit in this architecture. Concerning the spin qubit dephasing times in these various implementations, they are found to be significantly smaller in Si devices compared to non cQED architectures, with $T_2^* \sim 60-120$ns when the qubit is resonant with the cavity [25, 26, 96] and $T_2^* \sim 600$ ns when the qubit is off-resonant with the cavity [25]. With the CNT device, $T_2^* \sim 60$ ns with the qubit on resonance with the cavity was observed [24], about an order of magnitude higher than previously reported [88] but still orders of magnitude smaller than expected. The origin of the larger dephasing rate in the cQED architecture compared to non cQED architecture is not understood yet but could arise from the electromagnetic environment of the cavity whose fundamental mode is much larger than the spin qubit device. This is why it is reasonable to think that there is room for improvement for the CNT device as it was not an ultra clean CNT which would have much less defects that could couple to the electromagnetic field of the cavity and induce dephasing.

With this in mind, we developed a high vacuum stapling technique that allows for the realization of ultra-clean CNT devices in microwave cavities during the PhD work of Tino Cubaynes. The development of this *stapling* technique started in the group of Z. Zhong [100], and inspired several other groups in Delft, Basel, Regensburg, Barcelona and at the Weizmann institute. It allows for realizing a priori arbitrary complex circuits with CNTs. The principle of the stapling technique is depicted in Figure 2.11 and follows closely from the technique developed at the Weizmann institute which was the most successful [101].

Contrarily to previous fabrication techniques used in our team, the CNT is deposited on the nanocircuit electrodes at the last step, just before being transferred in the cryostat for measurement as depicted on Figure 2.11. Therefore the CNT is never exposed to any resists nor to any possibly strongly damaging electronic beams during the lithography process. The CNTs are grown on a comb of cantilevers (30 µm wide, 5 µm thick with a pitch of 60 µm). Then they are aligned with the nanocircuit electrodes thanks to micro- and nano-manipulators (piezo-electric actuators) with direct optical access in a high vacuum chamber around 5×10^{-7}mbar. The actual contact between the CNT and the electrodes of the circuit is monitored electrically as the circuit is voltage biased and becomes closed when the CNT is deposited. A "touch-down" contact resistance of $\sim 10\,\mathrm{M\Omega} - 100\,\mathrm{G\Omega}$ is typically observed. Then the CNT is cut on both sides of the electrical circuit by passing a strong current of the order of 10 µA. During this electrical cut step, an annealing of the contact between the CNT and the electrode occurs, which lowers the contact resistance to values of $\sim 100\,\mathrm{k\Omega} - 2\,\mathrm{M\Omega}$ at room temperature, compatible with transport and microwave experiments in the milli-Kelvin range afterwards. We note that by adjusting the relative height of the electrodes and their pitch, it is possible to realize either suspended CNT device which offer high controllability or devices with the CNT lying on the electrodes. The latter choice is typically useful with magnetic gates because it maximizes the magnetic stray field at the CNT location, as will be discussed in the following chapter 3. In the resulting ultra-clean CNT devices, that are now routinely fabricated in the laboratory, we observe much cleaner, closer to ideal, electronic spectrum with a high controllability.

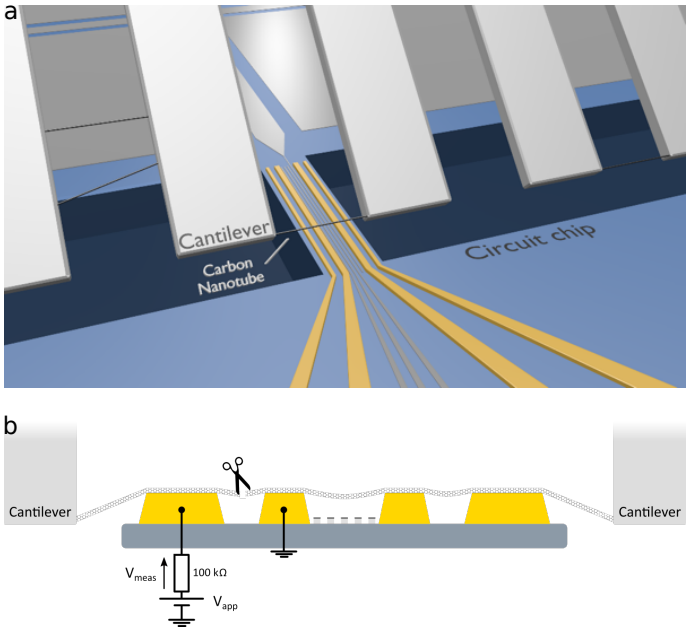

Figure 2.11: (a) Schematics of the stapling technique showing the comb of cantilever with a carbon nanotube approaching the electrodes (yellow) of a circuit embedded in a microwave cavity in coplanar waveguide geometry. A trench in the substrate is etched (dark blue) to allow for bringing down the cantilevers. (b) Side view of the device and the cantilever after CNT "touch-down" with CNT lying on the contact electrodes (yellow) and suspended over the electrostatic gates (grey). The inner contacts are the leads of the circuit and the outer contacts are the cutting electrodes. The electrical setup to cut the CNT between an outer and inner contacts is shown.

A spin qubit device compatible with the CNT stapling technique is presented in Fig-

ure 2.12. Trenches for the cantilever stapling are visible in the cavity ground plane and the non-collinear ferromagnetic electrodes are fabricated as zig-zag to ensure having an angle of about 30 degrees between the two magnetization axis at the quantum dots locations, wherever the CNT is deposited. The working principle of this spin qubit based on artificial two-sites spin-orbit interaction [22] is recalled on Figure 2.12(d,e). The local Zeeman field in each dot (achieved in our case by exchange interaction) lifts the spin degeneracy and the coupling between the two dots orbitals with different spin quantization axis create avoiding crossings giving the spectrum shown in Figure 2.12(d). Each K/K' valley of CNT generates a similar spectrum and we omit the valley index in this spectrum, for clarity. At large detuning energy between the two dots (outside the grey shaded area), the spectrum becomes one of a pure spin transition while it is a pure charge qubit spectrum at zero detuning (in the middle of the grey shaded area). The qubit is then manipulated by cavity photons (on or off resonance) and the qubit state population is read-out through the transmitted cavity field. In the following, only the phase of the cavity field will be measured for this matter. In this work the double quantum dot is operated in a regime of a few electrons occupancy, typically with around 10 electrons. This is to be compared to previously discussed spin qubits which were operated in the single electron regime as is standard. It is widely admitted that the single electron regime is more suitable, in particular because the spectrum is the simplest possible, but we can mention that it was also reported that multi-electron quantum dot spin qubits could be favourable in some particular electron occupancies [102]. While we could not play with the electron number (the reason being that the coupling of the spin qubit to the cavity field was not large enough with other low electron occupancy configurations [94]), it is actually not a problem as it is typically only the last electron added to the nanotube which interacts electrically with the cavity.

The microwave spectroscopy of the ferromagnetic spin qubit is conveniently done by reading out in the dispersive regime the phase of the cavity signal when a second tone is applied through the cavity and its frequency is swept. At large detuning ϵ_δ, the phase is mainly sensitive to the expectation value $\langle\sigma_z\rangle$ of the spin projection along the quantization axis of the left (right) dot. In the dispersive regime, the expression of the phase ϕ reads

$$\phi = \frac{2g_s^2}{\kappa\Delta}\langle\sigma_z\rangle + \phi_0, \tag{2.20}$$

where ϕ_0 is a constant which only depends on the microwave setup, κ is the linewidth of the cavity, g_s is the spin–photon coupling strength and $\Delta = f_{\text{cav}} - f_{\text{spin}}$ is the detuning between the cavity frequency f_{cav} and the spin qubit frequency f_{spin}. Such a measurement is shown in Figure 2.13(a) which displays the phase contrast $\Delta\phi$ as a function of the tone frequency f_{pump} and ϵ_δ. In order to avoid cavity photon back-action on the spin qubit, we used a pulsed microwave spectroscopy : the qubit is first driven for $t = 3\,\mu\text{s}$, then the cavity is filled after 90 ns and finally read-out using a fast data acquisition board for $t = 700\,\text{ns}$. Apart from the frequency independent vertical blue stripe which simply signals the left/right degeneracy line at zero detuning, we observe three resonances which disperse close to zero detuning and saturate at 6.506, 6.530, and 6.540 GHz, respectively. The dispersion of each of these transitions with a minimum at zero detuning and a saturation at large detuning is characteristic of a transition which becomes a pure spin transition in the large detuning limit due to the perfect localization of the electron in one quantum dot (see Figure 2.12(d)). The saturation value is given by the effective Zeeman field felt by the (pure) spin state at large detuning. The fact that we observe several spin transitions can be attributed to the lifting of the K/K' valley degeneracy of the nanotube as well as from the fact that we are not in the single electron regime. A cut along the lowest resonance at

large detuning is shown in Figure 2.13 (b). This measurement, fitted by a Lorentzian, has a full width at half maximum of $\gamma_{\mathrm{FWHM}}/(2\pi) = (498 \pm 80)$kHz which sets an upper bound of the decoherence rate $\gamma_s/(2\pi) \leq \gamma_{\mathrm{FWHM}}/2/(2\pi) = 249\,\mathrm{kHz}$. This is the main result of this work as such a narrow line width is two orders of magnitude lower than what was observed in the previous works with CNT and valley-spin qubit devices as discussed at the beginning of this section. Interestingly, the qubit is here off-resonance from the cavity and the measured spectroscopic line width compares to the ones mentioned in Si spin qubit devices in cavity. This is therefore the first time that a CNT shows its potential as a host for highly coherent spin qubits.

In order to specify the decoherence mechanism explaining the linewidth found for our spin transition, the dependence of the decoherence rate as a function of the detuning ϵ_δ was measured. Such a measurement is displayed in Figure 2.14 (a). The two main decoherence sources for a spin qubit in double quantum dot are again charge noise and nuclear spin noise. The charge noise is related to the fact that the qubit transition frequency may fluctuate if offset charges nearby the device change the detuning. Therefore, it should induce a decoherence rate γ_s proportional to the derivative of the qubit transition frequency with respect to the detuning [22]. For a large detuning ϵ_δ, the nuclear spin bath is on the contrary expected to give a nearly independent contribution as a function of the detuning. The decoherence rate γ_s and the derivative $\partial\omega/\partial\epsilon_\delta$ as a function of detuning ϵ_δ are shown to overlap well provided we add a residual constant of about 500 kHz to the derivative in Figure 2.14(a). The linear behavior of the decoherence rate γ_s as a function of the derivative $\partial\omega/\partial\epsilon_\delta$, displayed in inset, shows that our spin–photon interface is dominated by charge noise at small detuning. Interestingly, it allows us from the slope of the linear behaviour to extract a charge noise detuning variance of about 34 µeV. While this noise is larger than in the previous work in carbon nanotubes [103] and could be in principle easily lowered, it is interesting to see that we can completely reduce its influence by going at large detuning while keeping a large spin–photon coupling strength with respect to γ_s. The shaded gray corresponds to the residual decoherence mechanisms with a decoherence rate in the range $\gamma_s/(2\pi) \approx 500\,\mathrm{kHz}$. Note that this value corresponds to twice as much as the lowest decoherence rate presented in Figure 2.13 (b) (250 kHz), probably because it corresponds to a lower detuning.

This value of residual decoherence rate allows us to estimate the contribution of the nuclear spin noise due to the 1.1% ^{13}C present in CNT and therefore of the hyperfine coupling constant A_n^{CNT}. In Ref. [5], we claimed that this number was for the first time compatible with the tabulated expected value of $A_n^{\mathrm{CNT}} = 0.1 - 0.5$µeV. What is actually correct is that this number is indeed compatible with the tabulated expected value when compared to previous experimental estimations in CNT. What it means is this : the correct formula for the dephasing time that we derived in section 2.1, Eq.(2.16), was not used because "unknown" to all of these works. Therefore the relative comparison between them is correct and we indeed observed a two orders of magnitude improvement of the spin decoherence rate in CNT, as observed from the resonance line width, with respect to previous works [88, 89], therefore reducing by about two orders of magnitude the upper bound on A_n^{CNT}. Let us now recalculate A_n^{CNT} of these works using the correct formulas Eqs. (2.16) and (2.17). We find for Ref. [89], $A_n^{\mathrm{CNT}} = 800\,\mu\mathrm{eV}$ instead of 400 µeV reported[7], and for Ref. [5] $A_n^{\mathrm{CNT}} = 20\,\mu\mathrm{eV}$ instead of 0.1 µeV reported. The two orders of magnitude improvement in dephasing rate does not fully translate to a two orders of

[7]There was also an error in the estimation of the number of atoms which partially compensated for the misuse of Eq.(2.16).

magnitude decrease in the estimation of the hyperfine constant due to the quantum dots not being of the same size, hence not having the same number of atoms, in both works. Looking at Figure 2.14(a) with fresh eyes, we can re-interpret the charge noise saturation by a still slightly decreasing contribution, probably with a quadratic dependence as the dot is in the deep Coulomb blockade regime and co-tunnelling process are dominating. With a tenfold decrease of the charge noise as already realized in the lab [103, 104], we can reasonably expect to obtain a tenfold decrease in the observed nuclear spin noise and consequently the of hyperfine coupling constant.

To finish with the CNT spin qubit, we observed an optimal operation point due to the spin-electric-coupling, as for non cQED spin qubit discussed in the previous sections. The trade-off works as follows; the electron-photon coupling decreases with increasing detuning (and departure from pure charge qubit) as shown in Figure 2.14 (b) while the decoherence rate decreases with increasing detuning as the qubit becomes more spin-like as shown in Figure 2.14 (a). While in this work we could not performe time resolved manipulations of the qubit, Rabi oscillations, we can still characterize the optimal qubit working point. Namely, we look at the cooperativity of the spin-photon interface, defined as $C = (2g_s)^2/(\kappa\gamma_s)$ which tells that the coupling between the two systems (spin and photon) is stronger than the geometric mean of their respective losses[8]. Cooperativity is shown in Figure 2.14(c) as a function of detuning. Clearly, the decoherence rate decreases faster than the spin-photon coupling in the beginning, increasing C until it reaches a maximum at $C = 12.9$ before decreasing, meaning that the enhancement in the coherence time does not compensate for the decrease of the spin-photon coupling. We note here that $C = 12.9$ is the largest cooperativity reported in any spin-photon interface in cQED architecture so far.

2.4 Perspectives

The field of spin qubits in semiconducting host material has reached maturity in the last years, efficiently fighting nuclear spin noise and reaching beyond the fault tolerance threshold in the two most developed materials, GaAs and Si. The next challenge is now the one common to all qubit platforms, scaling-up the demonstrated single or two-qubits devices to many qubits (several tens first, then hundreds, thousands and millions). This task requires the assistance of companies, as is already the case with Google, IBM, Microsoft, Intel and many others already engaged in the race. There is still room for basic research but a significant part of the job has become what is now called “quantum engineering”.

My personal perspectives for the coming years regarding spin qubits are all regarding CNT based spin qubits as CNT is now my main working host material. They can be divided into two directions, which have been discussed in this chapter. First there is the motivation to perform manipulations of spin qubits as described in subsection 2.3.3. With the stapling technique that allows to embed multiple devices in a single cavity and the development of cQED for superconducting qubits, CNT based spin qubits could be a credible alternative to Si based spin qubits with coherence times that are starting to show comparable values. Besides, coupling multiple spins in a cavity through microwave photons opens possibilities to tackle several fundamental problems. Indeed it would enable

[8]Being in the strong coupling regime implies having $C \geq 1$ however it is possible to have $C \geq 1$ without being in the strong coupling regime, for example with a very small photon loss and a large loss of the other system, typical with lasers for example.

to go beyond first neighbour spin-spin coupling and could possibly allow one to investigate spin fluctuations in spin-spin coupling engineered diagrams that could have implication for high-Tc superconductivity for example. With this in mind, the next target is to realize a 3-spin qubit device which would allow for demonstrating the suitability of this architecture and play with quantum information manipulation (3 qubits Toffoli gate for example) and more condensed matter situation of long distance spin-spin coupling.

Second there is the desire to investigate more deeply the nuclear spins in CNT. Obviously the first target is to reduce the charge noise in future devices to measure nuclear spin noise and re-estimate the upper bound on the hyperfine coupling constant in CNT, hoping to reduce it closer to its expected value. Then there is nuclear spins dynamics in CNT. Is it also sub-diffusive as in GaAs? If yes, will it show a similar exponent $\alpha = 0.8$? We can expect it will not be similar as "diffusion" in the CNT should be one dimensional compared to being two dimensional in 2DEG. Then it will be exciting to grow ^{12}C purified CNTs to further increase the dephasing time of spin qubits. A new chemical vapour deposition setup dedicated for isotopically purified carbon CNT growth has been developed in the laboratory and is expected to deliver nuclear spin free CNT in the coming year. The first use of such CNT will of course be for quantum information manipulation with the hope of reaching several tens of microsecond dephasing times similar to Si spin qubits. Another aspect is that with the typical quantum dots size we use and a residual concentration of 800 ppm of ^{13}C, we would get of the order of 20 nuclear spins only interacting with the electron spin qubit (comparatively, in purified ^{28}Si spin qubits, there are still about $100 - 200$ nuclear spins interacting with the electron spin). This limit gets very close to the purely quantum noise regime with typically around 10 nuclear spins [43, 44, 66, 105, 106]. In this limit, it is predicted that the quantum limited coherence time is smaller than the spin echo coherence time because spin echo would also compensate for quantum spin flips [107], which we could directly investigate.

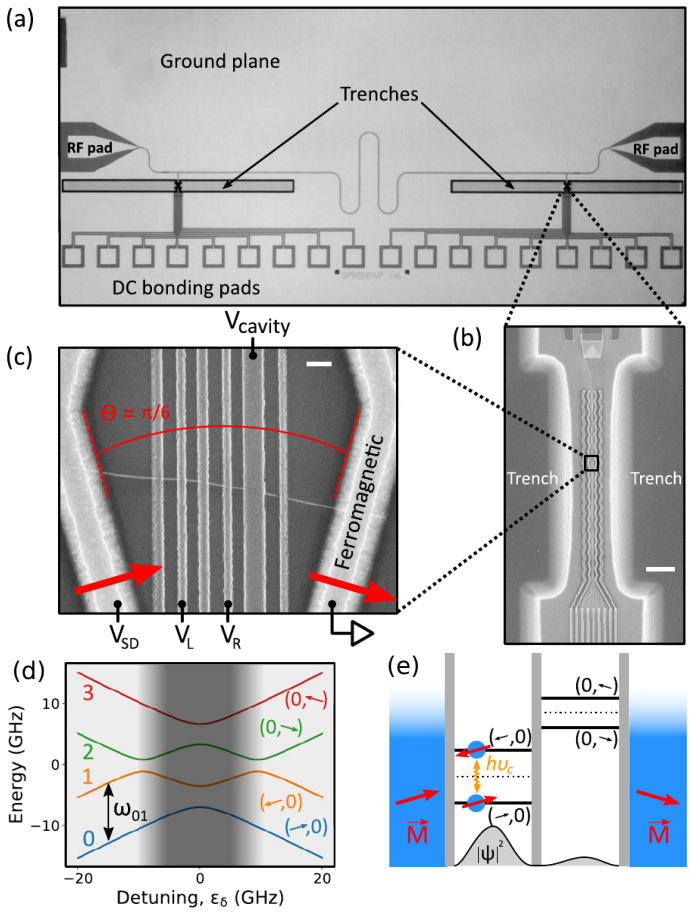

Figure 2.12: (a) Large scale view of the circuit QED setup. Only one of two circuit areas is used. Scale bar: 1 mm. (b) Scanning electron microscope (SEM) image of the pedestal structure on which the device is made with the zig-zag magnetic contacts. Scale bar: 10 µm. (c) Zoom on the device showing the bottom gates and the non-collinear ferromagnetic contacts. Scale bar: 200 nm. (d) Spectrum of our spin quantum bit. The spin transition addressed in this work, the 01 transition, saturates to a value defined by the effective Zeeman splitting of each dot at large detuning. In the shaded gray region, spin and charge are not good quantum numbers anymore. (e) Schematics of our device showing the concept of spin–photon coupling.

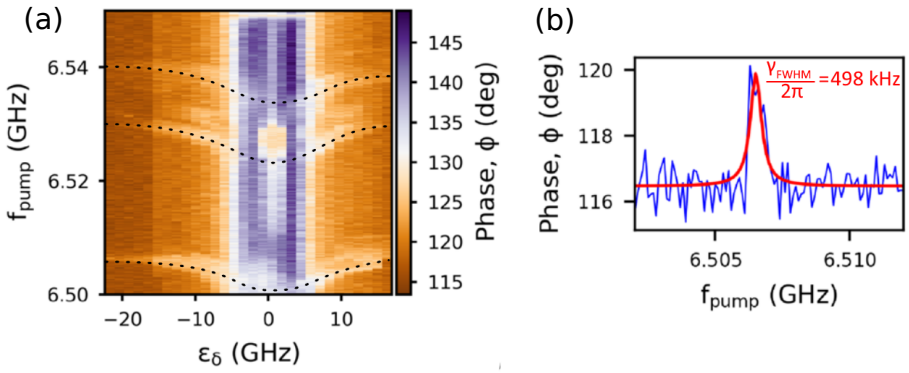

Figure 2.13: (a) Microwave two-tone spectroscopy as a function of the DQD detuning ϵ_δ and pump frequency f_{pump}. The phase of the transmitted microwave signal at the cavity frequency is plotted. (b) Resonance corresponding to the lowest transition of (a) at a large detuning < -21 GHz (blue line). The exact detuning value is unknown due to a gate offset jump which occurred during the measurement. The red line is a Lorentzian fit which allows us to extract γ_{FWHM}.

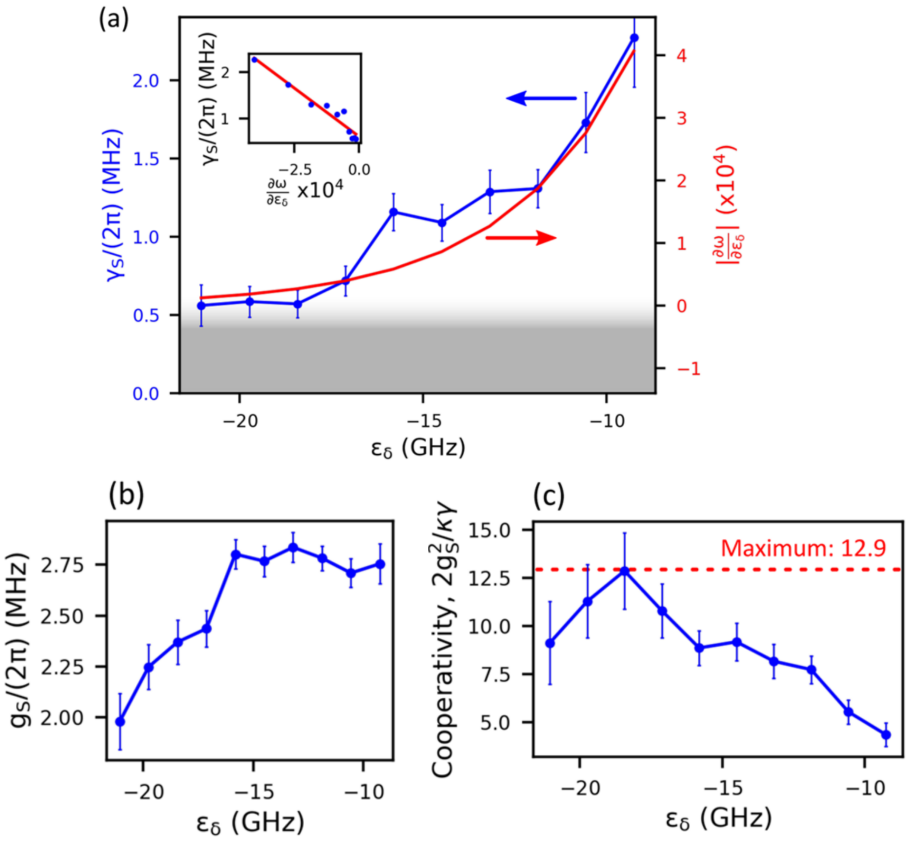

Figure 2.14: (a) Linewidth and derivative of the dispersion relation of the spin transition as a function of detuning (the derivative is obtained by fitting the dispersion relation of Figure 2.13a and calculating the derivative from the fit). A constant corresponding to a decoherence rate of 560 kHz is added to the derivative. Inset: Linewidth as a function of derivative. (b) Spin–photon coupling strength as a function of detuning. (c) Spin–photon cooperativity as a function of detuning. The error bars are the standard deviation extracted from least square fitting of the spin spectroscopic line in Figure 2.13a

Chapter 3

Spin textures for topological excitations

In the current race for building a quantum information processor, there are various types of qubits in condensed matter that are actively developed. We have seen in the previous chapter that electron spin qubits in semiconductors are good candidates, still lacking the demonstration of their potential scalability compared to superconducting qubits which are slightly ahead, with the demonstration of "quantum supremacy" with a 53-qubit chips in 2019 [84]. At this stage, both these implementations are still very far from delivering a full scale quantum processor comprising millions of physical qubits.

One major reason is the need to perform quantum error correction which is very demanding in the number of physical qubits. An alternative approach is to use topologically protected qubits which possess an autonomous exponential protection to errors [108] that would significantly reduce the hardware overhead. These topologically protected qubits rely on the existence of so-called Majorana zero modes (MZM) which are the condensed matter counterparts of Majorana fermions in particle physics [109]. The promises of MZM based topologically protected qubits arise from their intrinsic exotic properties; they are their own antiparticle (they are said to be self-adjoint) and they possess non-abelian exchange statistics[1]. The latter property says that the result of the exchange of two localized particles depends on the path taken during the exchange (either in real space or in phase space) and is named braiding as it is an operation of the braid group [110]. Braiding of MZM, beyond being a resource for topologically protected quantum computation, is a fascinating quantum operation by itself and is worth experimental demonstration on its own.

3.1 Majorana zero modes in 1D

While braiding can only be done with two dimensions (it was first proposed to braid vortices [111] in 2D topological superconductors where MZM should exist at the core of the

[1] A particularity of localized MZM in 1D or 2D systems is their non-abelian exchange statistics. Indeed, while in 3D particles can only follow the bosonic or fermionic statistics (when exchanging two undistinguishable particles, the global wave function stays identical or picks up a minus sign), in 2D a richer behaviour can exist. For example, the wave function can pick up a phase (anyonic statistic). When the ground state is degenerate, particle exchange can lead to a change in the state of the system, represented by a unitary operation on the wave function (non-abelian statistics). The state of a system after several particle exchanges then depends on the order of the exchanges, since the corresponding unitary operations do not necessarily commute.

vortices [112]), these two dimensions do not need to be both, or either, in real space so that a 1D support is also suitable. In 2010, two theoretical proposals found a way to realize a non-trivial topological phase that can host MZM in 1D without relying on exotic materials [113, 114]. While the question of braiding MZM in 1D systems was not clearly settled theoretically at the time, 1D systems had several advantages that put them forward. Indeed the 1D systems envisioned at the time (that are still the main investigated systems as of now) were semiconducting nanowires which benefited from many technological advances in nanodevices fabrication. Indeed, the degree of control of the microscopic systems in semiconducting nanodevices (as the ones of the previous chapter) is unprecedented compared with 2D material science where the strengths lie more in spectroscopy than in manipulation. Still we note here that several experimental implementations of the latter have been recently realized in atomic chains [115–118] or islands [119] where signature of MZM have been observed. The common ground between these implementations is that the non-trivial topological phase hosting the MZM is not intrinsic to an exotic material but rather engineered by combining the right ingredients from more conventional materials.

To understand these ingredients, we should first quickly come back to the origin. The fact that MZM are the counterparts of Majorana fermions arises from the equivalence of the Bogoliubov-De Gennes (BdG) Hamiltonian describing superconductivity with the Dirac equation. The superconducting gap and the particle-hole symmetry of the former are the equivalent of the mass term and the particle-antiparticle symmetry of the latter. Searching for eigenstates of the BdG Hamiltonian satisfying the self-adjointness condition of "Majorana fermions" $\hat{\gamma} = \hat{\gamma}^\dagger$ with $\hat{\gamma}$ the annihilation operator of a MZM, it appears that either p-wave superconductivity is required, as initially envisioned [108, 120], or spin rotation symmetry needs to be broken in a s-wave superconductor [121–124]. p-wave superconductivity, sometimes referred to as topological superconductivity is an exotic type of superconducting pairing that is still difficult to realize experimentally. On the contrary, s-wave superconducting pairing is standard and spin-rotation symmetry can be broken if such pairing correlation is induced in a helical electron fluid. A helical electron fluid is found in systems with Rashba spin-orbit interaction and a Zeeman field perpendicular to it, which can be either realized intrinsically in edge states of topological insulators or in 1D systems with spin-orbit interaction under an external magnetic field (see Figure 1.1). The latter choice, being more simple in terms of material and benefiting from years of nanofabrication techniques development, is the one that was massively adopted by experimentalists. Therefore the recipe to engineer MZM in 1D systems requires the following ingredients to be combined : 1D semiconductor, strong spin-orbit coupling, homogeneous magnetic field perpendicular to it and s-wave superconductivity.

The most advanced devices made for that purpose are those combining superconductors and semiconducting nanowires [125–127] or 2DEGs [128]. In these systems, the engineering of the topological phase is done using the large intrinsic spin-orbit interaction of the nanowires combined with superconductivity under a high magnetic field [108, 113, 114, 129]. Superconductivity is now induced in the nanowire using epitaxial aluminium directly deposited at its surface, which provides hard superconducting gaps [130]. The readout of the emerging excitations is done by conventional transport measurements searching for robust zero bias conductance peaks (ZPCB), a signature of MZMs [125–127]. Manipulation of the MZM is expected to be performed by making 2D networks with nearest neighbour tunnel couplings [128, 129, 131, 132]. This scheme was expected to have bear fruits two

years ago, which shows that this approach is very challenging.

It is important to stress at this point that, as of now, it has become widely accepted in the community that none of the observed ZBCP constitute an irrefutable proof of existence of MZMs in these systems, as they can be attributed to topologically trivial, Andreev-like, states [133–135]. Recently, a ZBCP with quantized conductance (another expected characteristics of MZMs) was observed for the first time [127], but the same team reported shortly after, that such a signature was actually not sufficient as it was not observed on large enough ranges of magnetic field and gate voltages [136]. It was even theoretically shown that quantized ZBCP can be due to trivial Andreev states [137], which now seems to have been confirmed experimentally [138]. More generally, experiments now find ubiquitous ZBCP due to trivial Andreev states mimicking MZM [139] which are well supported by several theoretical works [140, 141]. A well established theory group in the field even states that most, if not all, of the observed ZBCP in superconductor-semiconductor nanowire structures are actually not MZM due to, in particular, large disorder in the devices [142]. Another transport signature of MZM is the splitting oscillation of the ZBCP with magnetic field, wire length or chemical potential [143–145]. The amplitude of the oscillations should increase with increasing magnetic field or decreasing length, but the opposite was systematically observed [146–151]. A possible explanation for this behaviour, compatible with MZM, was found using a spatial step-like spin-orbit interaction in the system [152]. However a recent work shows that such a behaviour arises mostly in a region of the parameter space where the excitations are trivial Andreev states [153]. In addition, the epitaxial superconductor at the surface of the nanowire is now also considered potentially detrimental to the emergence of the topological phase despite the induced superconducting hard gap, because amongst other things, it strongly affects the chemical potential in the nanowire [154–157]. Finally, the latest devices use a quantum dot in the normal state at the end of the 1D topological section to read out the ZBCP (this quantum dot actually forms on the side of the epitaxial superconductor not covering the whole nanowire and is thus a "side effect"). It has recently been theoretically shown that in such systems, the electron g-factor of the quantum dot is strongly renormalized and can decrease exponentially to zero for some orbitals, which would explain why some states appear to be pinned at zero energy in magnetic field [158, 159]. It would therefore always be possible to find an apparently ZBCP robust to magnetic field in this architecture by looking for the right dot orbitals.

The previous paragraph summarizes well the current state of the field in what is now called the "*zero bias peak controversy*". What the debate points to is not that the observed transport signatures are not due to MZM, but that they could as well be due to topologically trivial states. The reasons for doubting the nature of the observed ZBCP seem to arise from the materials and device design as well as from the readout scheme. Disorder in the nanowires which are not 1D enough (typically nanowire devices show of the order of about ten conduction channels) and disorder in the spin-orbit interaction and in the chemical potential which are affected by the epitaxial superconducting material. Ultimately, it appears clearly that transport measurements can hardly distinguish between trivial and non-trivial topological states. This analysis calls for the need of developing alternative platforms that could host MZM as well as using other experimental tools to evidence and manipulate their exotic properties. Carbon nanotubes are good candidates

for the host material as they are near ideal 1D conductors[2] that can be ultra-clean (without defects) as discussed in subsection 2.3.3. Carbon nanotubes have a relatively large spin-orbit interaction due to their curvature, theoretically predicted and measured to be of the order of several hundreds of μeV (see Ref. [160] table. II), with even a few meV value reported [161], one order of magnitude larger than expected. While the spin-orbit strength in CNT is comparable to those found in semiconducting nanowires like InAs or InSb (respectively $0.015 - 0.135$meV and $0.25 - 1$meV [162]), it is not of Rashba type and thus cannot induce a helical fluid in the presence of a perpendicular magnetic field. This is where the proposals to induce a synthetic Rashba spin-orbit interaction with a periodic spatially varying magnetic field [31, 33, 35–37, 163] discussed in section 1.2 becomes very attractive. In addition to the synthetic spin-orbit interaction, the cycloidal magnetic field generated by a magnetic texture also induce autonomously a Zeeman field perpendicular to it. This aspect is particularly interesting as it could allow for MZM to emerge without the use of a global external magnetic field. It would therefore make the devices more compatible with complex geometries (where it is basically impossible to always satisfy the global magnetic field to be perpendicular to the spin-orbit interaction of all topological parts of the device) as well as with superconductivity whose order is destroyed by strong magnetic fields. We will come back to these points in section 3.3. We will now discuss in the coming section the experimental realization and observation of the synthetic spin-orbit interaction in a carbon nanotube.

3.2 Revealing synthetic spin-orbit interaction with magnetic field

This section discusses results published in Ref. [6]

The device that we designed differs in several points from now conventional devices. The device geometry is schematically depicted in Figure 3.1(a) and Figure 3.2(a). As said in the introduction of this chapter, we use a carbon nanotube as it is the closest possible to an ideal 1D conductor. It is deposited on top of a magnetic texture with alternating magnetic domains pointing out of plane to generate a synthetic Rashba spin-orbit interaction in the the conductor. Finally, compared to all current devices implementations for generating MZM, we will induce superconducting correlations from one lead (or both), meaning from the side of the 1D conductor and not along the 1D portion with either epitaxial superconductor [130] or the device deposited on a superconducting layer [115]. This last point is critical as many believe that the spin-orbit region and the superconductor need to spatially overlap in order to induce the topological phase which can host the MZM. However as we have seen from the short literature review above, the "conventional" geometry seems to lead to many parasitic side effects that cast doubts on the actual possibility to induce the topological phase. We therefore investigated theoretically our non-conventional geometry using tight-binding calculations on a Kitaev chain, a portion of which has superconducting correlations and another portion being normal with a spatially varying magnetic field, both being connected through a tunnelling element, as shown in Figure 3.1(b). Calculating the density of states (DOS) along the chain as a function of energy, shown in Figure 3.1(c), we observe that it is possible to find two zero energy modes, localized at both ends of the normal region, with the one at the normal-superconductor interface being more strongly

[2] the Fermi wavelength is of about 10 nm, larger than the typical nanotube radius of about 2 nm so that the transverse confinement leads to only one conduction channel with spin and valley degeneracy.

localized. The Majorana character of these zero energy modes is evidenced by calculating the spin singlet and spin triplet correlations of the DOS independently, which shows that these zero energy modes are mainly triplet-like, as expected for MZM while the higher delocalized modes are mainly singlet-like (details can be found in the supplementary material of Ref. [6] or in the thesis of L. Contamin [17]). One important aspect though is that it is needed to have at least one site of overlap between the oscillating magnetic field and the superconductor to observe the appearance of the localized zero energy modes. We can understand this as the necessity that the rotating field must induce triplet correlations right in the superconductor, at least at the interface. This is experimentally relevant as the stray field of the magnetic texture will extend laterally beyond its edges. These preliminary calculations are thus encouraging that the device geometry we chose is well suitable for the emergence of a topological phase that can host MZM.

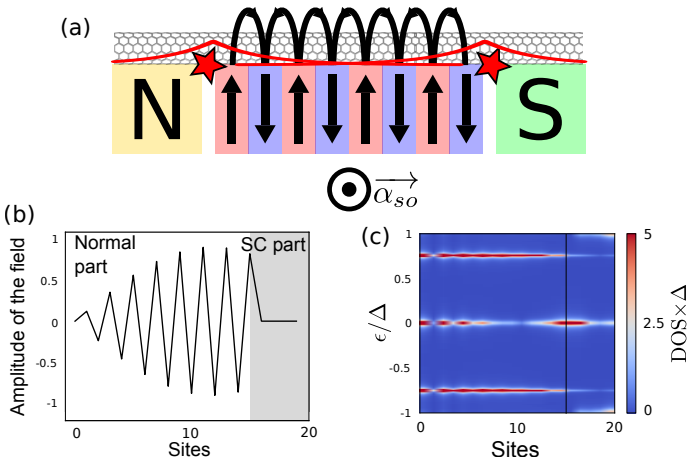

Figure 3.1: (a) Schematic picture of the device measured in Ref. [6] with a CNT contacted by a superconducting lead and a normal lead, lying above a magnetic texture gate. In such a device MZM (red stars) can localize at the boundaries of the region of topological phase generated by the cycloidal magnetic field. (b) Cycloidal magnetic field profile as used for Kitaev chain tight binding simulations, showing the normal and superconducting (SC) parts of the device. The envelope of the oscillations is an artefact due to undersampling because of the small number of sites ($N = 20$). (c) Density of states (DOS) as a function of site position and energy ϵ for the the situation in (b). Two localized MZM at zero energy are observed simultaneously with delocalized Andreev bound states at higher energy. The vertical black line indicates the boundary of the superconducting contact.

The device is shown in Figure 3.2(b) and (e). A single wall nanotube is stamped[3] onto a magnetic Co/Pt bottom gate bottom gate which is capacitively coupled to two gate electrodes, Gate 1 and Gate 2. The Co/Pt is expected to have a small pitch and an out of plane anisotropy, giving rise to several domains over the length of the nanotube, with a strong stray field of about 0.4 T as supported by magnetic characterization and simulations. The Magnetic Force Microscope (MFM) picture shown in Figure 3.2(e) evidences magnetic domains in the bottom gate, which have a typical size of about $100 - 150$nm. An external magnetic field B_{ext} changes the magnetic structure and can therefore reveal the existence of the synthetic spin orbit interaction.

[3]the "stamping" technique is the ancestor of the "stapling" technique discussed in subsection 2.3.3. In the stamping technique, the carbon nanotube is stamped or deposited on the wafer surface after being grown on quartz pillars. It then undergoes nanofabrication techniques like electron beam lithography and

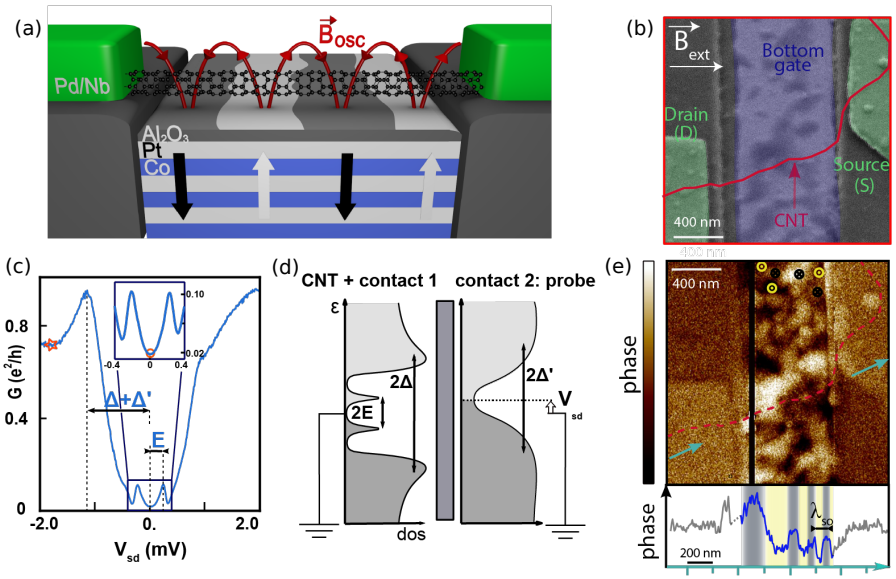

Figure 3.2: Hybrid superconductor-nanotube-magnetic texture setup. (a) Schematic picture of the multilayer magnetic texture with up and down domains (white and black arrows) inducing the rotating magnetic field in space (Bosc, red line) leading to the synthetic spin-orbit interaction. (b) Zoom on the device showing the single wall carbon nanotube (in red). The bottom gate is made from a multilayer of Co/Pt. The source and drain superconducting electrodes are made out of Pd/Nb. (c) Conductance of the device as a function of source-drain bias displaying a well-defined gap with two symmetric ALSs at energy E, shown again in the inset. The "hardness" of the gap is measured by the ratio of the conductance values marked by the star and the circle. (d) Density of states of the probe contact and of the nanotube, with the ALS arising from the coupling between the nanotube and the left superconductor, as fitted by Usadel equations. The right superconductor has a residual density of states at zero bias allowing for a direct spectroscopy of the ALSs. (e) Magnetic Force Microscope (MFM) micrograph of the device showing the magnetic texture of the bottom gate. The cut of the magnetic signal indicating field modulations (yellow and grey) along the nanotube on a scale of about 200 nm is shown at the bottom. Figures taken from Ref. [6].

Superconducting correlations are induced by connecting the nanotube to two Nb/Pd superconducting electrodes. We address the discrete spectrum induced by the superconductor by transport spectroscopy. The typical measurement of the differential conductance G as a function of source-drain bias V_{sd} is shown in figure Figure 3.2(c). The conductance displays a well-defined energy gap of about 550 µeV containing two peaks, symmetric with respect to zero bias. These two peaks signal Andreev-like states (ALS) arising from superconducting correlations. As sketched in Figure 3.2(d), our measurements are equivalent at low energy to conventional tunnel experiments as a consequence of the finite density of states at the Fermi energy in one of the two superconducting contacts (contact 2). Such a residual density of states in the superconducting leads is systematically observed in our devices and has also been reported by other groups (see for example Ref. [164]). This is why the device was sketched with a normal contact and a superconducting one in Figure 3.1(a). The global shape of the conductance curve is well accounted for by the quasi-classical de-

thin film deposition.

scription of superconductivity in the electrodes, based on Usadel equations and reveals that contact 1 displays a well-defined superconducting hard gap. The large subgap slope is shown to arise mainly from a residual pair-breaking in one of the superconductor (contact 2 in Figure 3.2(d)). The ratio between the high bias conductance and the zero bias conductance which measures the "hardness" of the gap is of about 45 which compares favourably with the recently reported figures in semiconducting nanowires [146].

One of the main findings of the experiment is displayed in figure Figure 3.3(c). In this colour scale map of G as a function of V_{sd} and the external magnetic field B_{ext} , we observe the evolution of the ALSs under an external magnetic field. They display oscillations with a period of about 0.6 T ($\pm 10\%$ from one magnetic sweep to another). We can resolve up to three oscillations around the mean energy of 220 µeV, together with the expected slow reduction of the superconducting gap. Such a behaviour is unusual for ALSs and has not been observed in any other system. It stems from the progressive alignment of the magnetic domains with the global magnetic field as depicted in Figure 3.3(a) which shows how the magnetic domains evolve from pointing out of plane with alternate orientations to all aligning in plane at a saturation magnetic field. The evolution of the magnetic texture domains leads inevitably to an evolution of the underlying helical band structure it induces. We can therefore get insights on the observed oscillations of the ALSs from the energy dispersion of electrons subject to a rotating magnetic field, $E(K)$ with K the wave vector, shown in figure Figure 3.3(b). The interference conditions defining the energies of the ALSs are set by the wave vectors difference ΔK between right-moving and left-moving electrons with non-orthogonal spins eigenstates. A variation of the magnetic domains induces a shift k in the wave vectors K. Near the helical gap, where the spin states are not orthogonal, it adds a term $2kL$ to the interference condition :

$$E_{\mathrm{ALS}} \approx \pm E_{\mathrm{ALS},0}\left(1 + a\cos\left[2\Delta K(B_{\mathrm{ext}})L\right]\right), \tag{3.1}$$

with $\Delta K(B_{\mathrm{ext}}) = \Delta K(B_{\mathrm{ext}} = 0) + 2k(Bext)$, $E_{\mathrm{ALS},0}$ the ALS energy at $B_{\mathrm{ext}} = 0\,\mathrm{T}$ and a the relative amplitude of the oscillations. The ALSs magnetic field dependence is well accounted for by this formula, under the assumption that the spin-orbit strength decays linearly as the field increases, up to a saturation field of about 1 T. Such an evolution of the synthetic spin orbit energy is supported by magnetic measurements as well as micromagnetic simulations.

The number of oscillations N sets the range of modulation of $k(B_{\mathrm{ext}})$ and therefore allows us to give a lower bound for the induced spin-orbit energy at zero magnetic field: $E_{\mathrm{so}} > \delta N/2$. From the number of oscillations in Figure 3.3(c) for $B_{\mathrm{ext}} > 0$ ($N \sim 1.5$) and the extracted level spacing $\delta \sim 1.5\,\mathrm{meV}$, we deduce $E_{\mathrm{so}} > 1.1\,\mathrm{meV}$. This is of the order of the simple estimate for a linear spectrum [36, 37] $E_{\mathrm{so}} = hv_F/(2\lambda) = \delta(L/\lambda)$ with $L/\lambda \sim 2$ corresponding to about 5 domains, inferred from the MFM picture in Figure 3.2(e). Strikingly, this spin-orbit energy is larger than the ones found in InSb or InAs nanowires. Moreover, we can reproduce the ALSs oscillations with simulations based on the scattering theory, with δ and $\Delta \sim 0.6\,\mathrm{meV}$ extracted from the data, an amplitude of the stray field B_{osc} of 400 mT extracted from the magnetic simulations and a chemical potential close to the helical regime. These oscillations are robust to disorder in the magnetic texture, as studied numerically in detail in the supplementary material of Ref. [6]. They can also be qualitatively reproduced from the spatial field evolution inferred from the MFM data of Figure 3.2(e). We point out here that the method we employed to estimate the spin-orbit interaction in our system is novel. Previous estimations in semiconducting

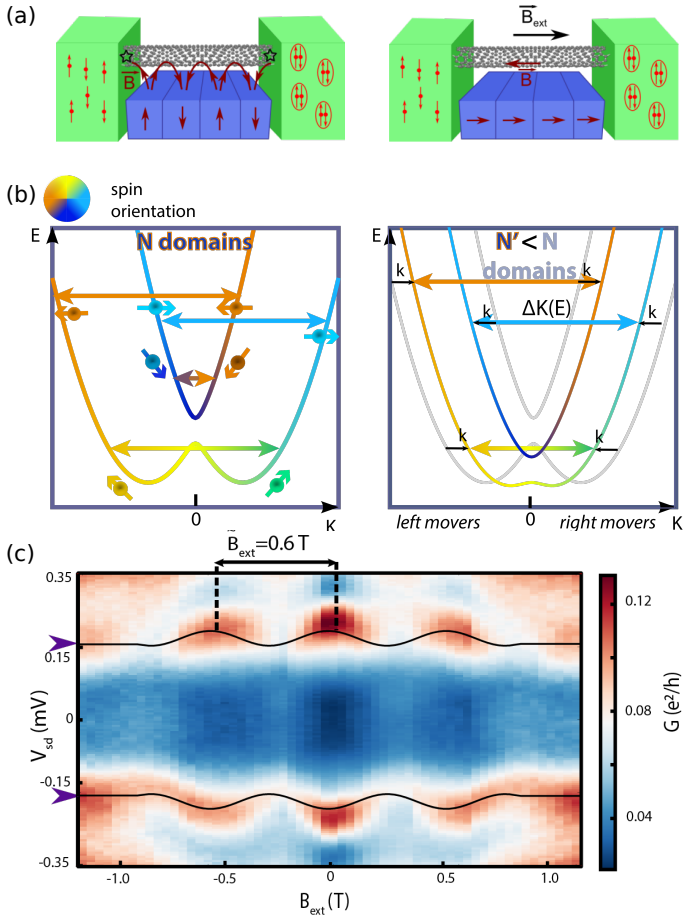

Figure 3.3: Oscillations of the subgap states and synthetic spin-orbit interaction. (a) Magnetic domains of the magnetic texture in the absence of external magnetic field (left) and in the presence of a strong external magnetic field $B_{\text{ext}} \geq B_{\text{sat}}$ with B_{sat} the saturation field of the magnetic texture. (b) Left panel: Band structure arising from the synthetic spin-orbit interaction with N domains. The allowed interferences in the finite length system are represented with arrows. Right panel: Schematics of how the band structure can be tuned by changing the spin-orbit energy, here decreasing (with N' domains, the bands are shifted by k). (c) Low bias differential conductance G map in the $V_{\text{sd}} - B_{\text{ext}}$ plane showing the oscillations of the ALSs (indicated by purple arrows) as a function of the magnetic field. The black lines are the fit to the theory. Figures adapted from Ref. [6].

nanowire devices comprises notably transport measurements, looking for a dip in the conductance as the chemical potential goes through the helical gap [165, 166]. However in these setup, no superconducting correlations are induced in the nanowire and especially no superconductor is epitaxially deposited on the nanowire, which could have detrimental effects for the spin-orbit interaction as reported. Therefore, our new method is the first that can estimate the spin-orbit energy in a nanowire device combining all the ingredients to host the topological phase of MZM.

The large measured value of spin-orbit interaction is an important prerequisite for driving a hybrid device into the topological regime, where zero energy Majorana modes can emerge. In all the devices experimentally investigated so far, this has only been pursued by applying a large external magnetic field, with severe constraints on network designs, Majorana mode lifetimes, and coupling to superconducting quantum circuits. In contrast,

our magnetic texture is equivalent to both a finite and large spin-orbit interaction and an external magnetic field: our device could host Majorana modes without any external magnetic field, thus lifting these constraints. In Figure 3.4, at zero external field, a ZBCP emerges, simply upon tuning Gate 2 at $V_g > 0.5 - 0.6$V. We note that this gate does not affect the ALSs nor the superconducting gap but only the appearance of the ZBCP along with a slight increase of the conductance background. The ZBCP has a width of about 150 µeV as shown in Figure 3.4(b), and a height of about $0.05e^2/h$, comparable to the recent findings in semiconducting nanowires (see e.g. Ref [126]). In addition, in our case the finite slope of the probe contact density of states affects the conductance height which cannot be mapped directly on the spectral weight of the states in the nanotube. In Figure 3.4(d), we measure a large magnetoresistance of 20% for this ZBCP, accompanied by a hysteretic behaviour which is a signature of the effect of the magnetic texture. This strong dependence at small magnetic field could come from local reconfiguration of the magnetic domains, consistent with the expected spatial localization of the state corresponding to a Majorana peak, contrary to the finite energy ALSs which are not affected by a small magnetic field. Finally, Figure 3.4(c) displays a conductance map where the ZBCP is robustly pinned at zero energy at large external magnetic field. These features are compatible with the ZBCP indicating the presence of a MZM, however they most probably still fall in the grey area of the *zero bias peak controversy* and more advanced manipulations of these states are needed to confirm their nature.

As a conclusion, we have demonstrated a device with a synthetic spin-orbit interaction induced by a proximal ferromagnetic multilayer producing an inhomogeneous local magnetic field. This spin-orbit interaction deeply modifies the superconducting correlations induced by superconducting contacts and allows us to observe a zero bias peak suggestive of a Majorana mode without any external magnetic field. By relaxing the constraint of an external magnetic field, our setup is suitable for advanced experiments that would unambiguously characterize Majorana modes with the tools of cQED circuits [167–171]. The use of a magnetic texture also enables obtaining Majorana modes in any conductor, such as CNTs but also graphene, Si/SiGe 2DEG... The built-in 2D pattern of our magnetic textures could also be interesting for braiding schemes [172] which could require networks of Majorana modes with local and autonomous generation of topological superconductivity.

3.3 Perspectives

As outlined throughout the previous section, the next move in the community should be to go to more advanced experiments. The motivation to realize topologically protected qubits inevitably requires to achieve manipulation of individual MZM, which in turn seems now to be the only way to unambiguously determine if the observed ZBCP signatures are indeed due to MZM. My perspectives in this field are therefore to exploit the synthetic spin-orbit interaction and device geometry discussed in the previous section to go beyond transport experiment to reveal the existence and exotic properties of MZM. As outlined, one of the advantages of the magnetic texture is that it induces autonomously both a spin-orbit interaction and a perpendicular Zeeman field which makes it possible to enter the topological phase at zero external magnetic field. The magnetic texture technology is thus fully compatible with conventional superconductor microwave resonators with which I plan to use the tools of cQED to probe and manipulate MZMs (current experiments with MZM devices in cavities were limited to zero external magnetic field and the investigation of trivial Andreev bound states [173]).

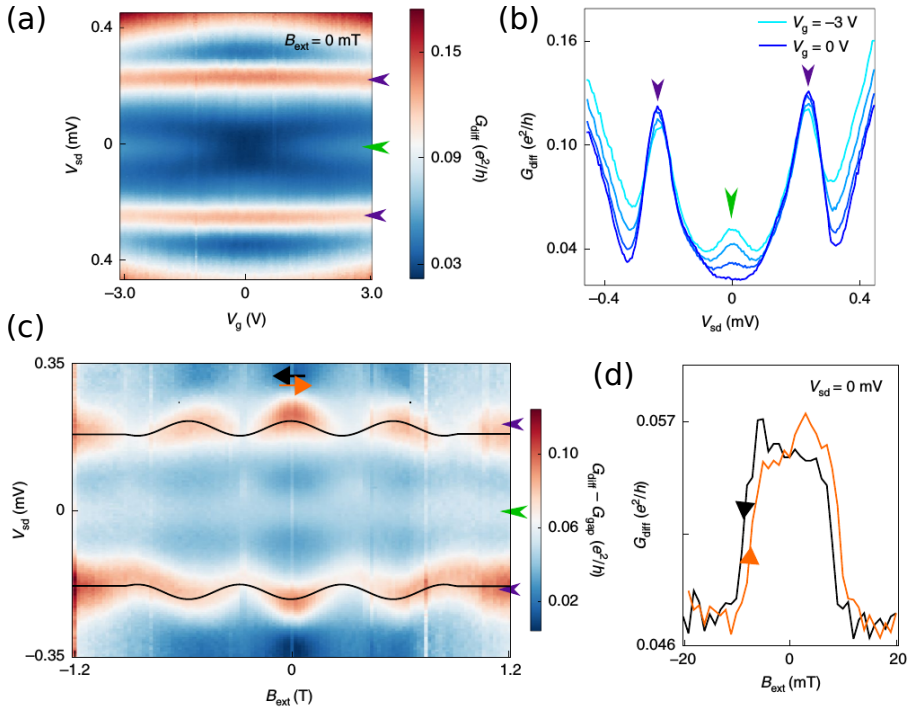

Figure 3.4: (a) Map of G in the $V_{sd} - V_g$ plane showing the appearance of a ZBCP when gate G is tuned. The ZBCP position is indicated by a green arrow and the ALSs by purple arrows. (b) G profiles for $V_g = 0, -1, -2, -3\,V$. (c) Map of G at $V_g = -3\,V$ in the $V_{sd} - B_{ext}$ plane showing the evolution of the ZBCP as a function of the in-plane magnetic field. The overall background G_{gap} arising from the superconducting gap has been subtracted for clarity. The black lines correspond to the same fit as Figure 3.3(c). The orange and black arrows indicate the magnetic field range of panel d. (d) Low magnetic field conductance G_{diff} profile map in the $V_{sd} - B_{ext}$ plane for $V_g = -3\,V$ displaying the large magnetoresistance of the zero-bias peak. The orange and black arrows represent the direction of the magnetic field sweep. Figures taken from Ref. [6].

The first objective will be to evidence the self-adjoint character of MZM. The self-adjoint property $\gamma = \gamma^\dagger$ with γ the Majorana fermionic operator of a MZM induces a non standard longitudinal coupling of the MZM pair to the cavity mode [167]. Such a longitudinal coupling has been considered as a hindrance or at best an indirect way to detect the self-adjointness of MZM [170]. I propose to directly exploit the longitudinal coupling to read out the state of the MZM topological qubit, a scheme recently proposed in cQED with superconducting qubits [174] and with spin qubits [175]. As this protocol only works with systems longitudinally coupled to the microwave photons, it will unambiguously reveal the self-adjointness, hence the non-trivial character, of the MZM. This is in contrast to the more common, and widely used in the cQED community, transverse coupling readout scheme which will be established for trivial excitations only, typically Andreev-like states. In short, a MZM pair $\hat{\gamma}_1\hat{\gamma}_2$, possibly realized in the experiment of the previous section, would be coupled to the microwave field of a cavity with a coupling g. This coupling is then modulated at the cavity frequency (using a local radio-frequency electrostatic gate, the coupling g being proportional to the overlap of the MZM electronic wave functions) to turn on the longitudinal readout [174]. It actually performs a parity measurement $\langle \hat{P}_{12} \rangle = \langle i\hat{\gamma}_1\hat{\gamma}_2 \rangle = \pm 1$ of the MZM pair, directly measurable as a displacement of the

coherent field of the cavity.

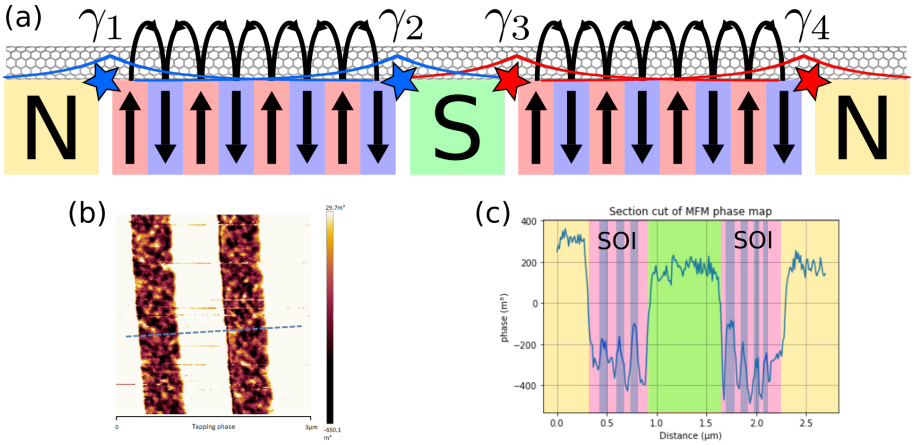

Figure 3.5: (a) Schematics of a device that can host four MZM in a carbon nanotube contacted by two normal conductors (N), one central superconducting lead (S) and above two magnetic textures inducing synthetic spin-orbit. The two MZM pairs are indicated by red and blue stars. (b) Magnetic force microscope image of two magnetic texture gates as required for (a). (c) Cut along the dashed line in (b) showing the modulation of the magnetic field. The color code is the same as in (a) to illustrate the feasibility of the device.

The longitudinal readout scheme therefore essentially realizes a parity measurement of a MZM pair, which is at the heart of measurement-only manipulation of MZM. It relies on a sequence of parity projective measurements instead of actually physically displacing the MZM around each others [176]. Such a protocol is sometimes referred to as "braiding without braiding" or braiding with quantum teleportation. A technically very challenging implementation of this protocol, based on tunneling transport measurement, was recently proposed [132]. In the longer run I plan to exploit the longitudinal coupling scheme to perform the successive projective parity measurements in a device hosting four MZM. The extension of number of MZM can readily be done by adding a second magnetic texture to a device similar to the one previously described. A schematics representation of this proposed device is shown in Figure 3.5 (a) with the expected localization of the four MZM γ_i for $i \in \{1, 2, 3, 4\}$. We have already started to develop this geometry in the lab with two magnetic textures on the side of a central electrode as shown in Figure 3.5(b,c). We actually embedded such a device, with a tunnel barrier instead of the central superconducting lead thus forming a double quantum dot, inside a microwave cavity. The double quantum dot geometry allowed us to probe the internal transitions between orbitals of the two dots. The magnetic textures induce a spin texture to each dot subject to their rotational stray field. This in turn give the double quantum dot transitions a non-trivial spin component that can be probed with the microwave field, in a similar manner to the two-site artificial spin-orbit coupling scheme of subsection 1.1.2 and subsection 2.3.3. The microwave signal of one of these transitions as a function of the energy detuning ϵ between the two dots and an external longitudinal magnetic field is shown in Figure 3.6(a) and (b). We observed a non monotonous dispersion of the transition with slopes corresponding to a electron g-factor of up to 60. It is important to stress that what is measured along the detuning axis is the difference in energy between the energy levels of the two orbitals. Therefore a naive interpretation of the dispersion slope is that it corresponds to the difference of g-factors of each dot, thus implying that one or both g-factors are actually larger than 60.

The naive model consists in a spin qubit with non-collinear magnetization as discussed in previous chapters, only with significantly stronger electron g-factors, dependent on the orbital due to the overlap of the electron wave function with the magnetic texture field. We see in Figure 3.6(c) and (d) that with this model we can quantitatively account for the shape of the transition dispersion and qualitatively for the contrast of the signal. This model however does not yield a microscopic understanding and we still need to investigate how the synthetic spin-orbit interaction induced in each dot can lead to such large g-factors. An important follow-up experiment with this device is to reach in one (or ideally both) dot the helical gap by tuning the chemical potential. There we would get more insights on how the magnetic texture shapes the spin component of the dot levels. This preliminary experiment combined with the experimental results of previous section as well as the theoretical calculations showing that our geometry can in principle host MZMs is thus encouraging that we can couple a MZM pair to a microwave cavity and probe their self-adjoint character.

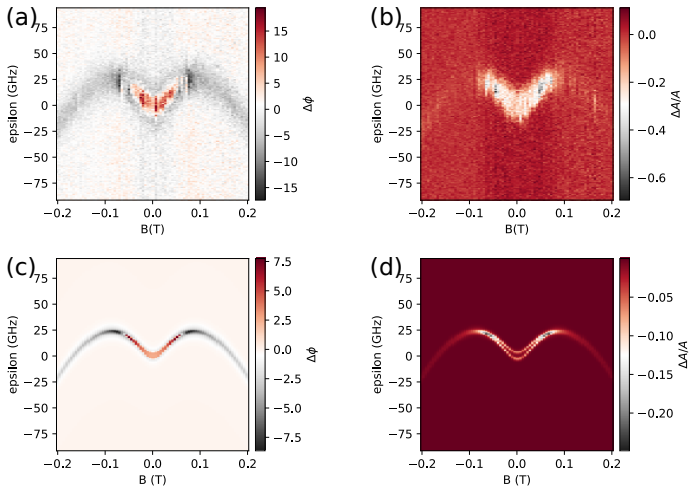

Figure 3.6: Cavity signal of the dispersion of the double magnetic texture quantum dot for one set of dots orbitals in the detuning ϵ and magnetic field B_{ext} plane. Experimental phase variation $\Delta\phi$ (a) and amplitude relative variation $\Delta A/A$ (b). Reciprocal simulations in (c) and (d) using a simple spin qubit model with non collinear magnetization similar to the one discussed in subsection 1.1.2 and subsection 2.3.3.

Finally, another perspective is to go back upstream and investigate devices with less combined ingredients. Indeed, in the experimental work presented in this chapter, we found a way to probe the synthetic spin-orbit interaction in a carbon nanotube device induced by a magnetic texture in the presence of superconductivity. This was absolutely relevant by itself and the observation of a ZBCP at zero magnetic field, however controversial it might be or appear, confirmed that this new device geometry is promising. Nevertheless, adding all those ingredients together can make it difficult to finely understand the role of each. This is why we devised the device previously mentioned with magnetic textures but no superconductivity. As we use an external magnetic field to probe the spin-orbit interaction from the oscillations of Andreev-like states, it would be very instructive to perform the same measurements on a device without a magnetic texture. This would probably be more than just a control experiment. Indeed, Andreev states in 1D systems are mostly *not* investigated with magnetic field but rather by controlling the superconducting phase, the chemical potential of the normal region where they exist or temperature (see for example Refs. [177–183]). In this kind of experiments a magnetic field is typically applied to destroy

superconductivity and perform a control measurement. To our knowledge, only few works reported on the evolution of Andreev states outside the topological phase under continuous tuning of an external magnetic field, in InAs nanowires with Al contacts [179] and InSb nanowires with Al or NbTiN contacts [164]. The conclusion of both experiments is that great care should be taken when interpreting MZM experiments. There can be a ZBCP without topological superconductivity due to a competition with the Kondo effect [179] and the tunnelling probe can be more complex than anticipated because of confined quantum states adjacent to the nanowire section [164]. Carbon nanotubes being much closer to ideal 1D conductors than semiconducting nanowires, and being also potentially much cleaner, are therefore very attractive to investigate the behaviour of Andreev states with magnetic field. Will such a simple and clean system without topological superconductivity yield the simple expected behaviour of oscillating Andreev states with magnetic field on a period larger than the level spacing as theoretically predicted [6]? Or will we find more complex signatures than expected that would impact the interpretations of MZM experiments? Any way, it is clear that we still lack such kind of experimental investigations in lower complexity devices that are crucial to properly understand the features observed in more complex MZM devices.

Conclusion

We have seen through the studies presented in this manuscript that the quantum property of the spin, although relatively simple in essence, still brings many attractive prospects in "modern" condensed matter, despite being one of the first quantum property discovered a century ago. Manipulation of a single spin or the shaping of the spin texture of electronic bands can be efficiently achieved with spin-orbit coupling. While nature can provide spin-orbit coupling intrinsically in materials, it is not always of the right form or of magnitude large enough. Hybrid circuits which combine materials of various dimensionalities and with different electronic degrees of freedom make it possible to engineer the desired Hamiltonian with the right spin-orbit coupling term. This is clearly far more a starting point than the final achievement.

The realization of good spin qubits reaching the fault tolerance threshold could only be done by actively fighting against the nuclear spin noise of the environment, either by exploiting the slowness of its fluctuations or by removing the nuclear spins, in combination with a strong spin-electric coupling. This is the first milestone on the road to quantum computation as it proves that these qubits are viable. The next move is to deal with the challenging task of scalability, which requires more man power and technological efforts. Or it can also be "insert a coin and play again", trying to find yet another alternative platform with promising properties. This is the way I want to pursue as it suits more my personal approach to experimental physics. Spin qubits in carbon nanotubes are quite close in essence to the semiconductor spin qubits aforementioned, with possibly better performances in terms of coherence time. And of course there remains many fundamental aspects to explore, in particular with regards to nuclear spins.

The other path is the one of topologically protected qubits based on Majorana zero modes for which spin-orbit interaction is a key ingredient and which are still far from the fault tolerance threshold milestone. Indeed, demonstration of a qubit is still missing, let alone if its fidelity can hold to the promise. At this stage, as underlined with the "zero bias peak controversy", it even remains to be experimentally demonstrated if all the ingredients of the 1D Majorana recipe are actually combining well in the devices, in the sense of understanding if they survive and behave as expected. In this respect, we demonstrated the first observation of strong enough a spin-orbit interaction in a device combining all the ingredients. The helical gap remains elusive though, and the behaviour of non topological states with external parameters such as magnetic field or chemical potential seems more complex than anticipated and thus would require some more in-depth investigations. However, it is also important to try to directly evidence the existence of the topological and exotic nature of MZMs, with probes other than transport measurements. Coupling pairs of MZMs (forming a qubit) to the photon field of a microwave cavity seems a promising way of testing their self-adjoint character and even perform braiding. While eminently

challenging technologically, we already showed preliminary results hinting at the possibility to realize the required devices and measurements.

Finally, an important message from chapter 2 is that for a qubit to have long coherence times is not necessarily enough to make it a good practical qubit. There needs also to be a good controllability with sufficiently large operation speed to reach the fault tolerance threshold. While the first step for a qubit to prove its viability is obviously to reach this stage, it arises right after the question of the operational frequency of the future quantum processor on which will run quantum error correction codes. We briefly outlined that the apparently worst of the qubits having reached fault tolerance could turn out to be better than the others depending on how quantum error correction codes are actually implemented. Until practical implementations are realized, it would therefore seem unreasonable to discard any qubit that could meet the fault tolerance threshold. As of now, superconducting qubits look to be quite ahead of other types of qubits but I honestly think that looking at the entire quantum computer road, almost all implementations are somehow at the same point. We are at an interesting stage where both quantum technology is developing fast to reach the holy grail and there is still plenty of room for fundamental condensed matter physics phenomena to explore. Both are important and needs one another.

Bibliography

[1] M. R. Delbecq, T. Nakajima, P. Stano, T. Otsuka, S. Amaha, J. Yoneda, K. Takeda, G. Allison, A. Ludwig, A. D. Wieck, and S. Tarucha, "Quantum Dephasing in a Gated GaAs Triple Quantum Dot due to Nonergodic Noise", Physical Review Letters **116**, 046802 (2016).

[2] T. Nakajima, A. Noiri, K. Kawasaki, J. Yoneda, P. Stano, S. Amaha, T. Otsuka, K. Takeda, M. R. Delbecq, G. Allison, A. Ludwig, A. D. Wieck, D. Loss, and S. Tarucha, "Coherence of a Driven Electron Spin Qubit Actively Decoupled from Quasistatic Noise", Physical Review X **10**, 011060 (2020).

[3] K. Takeda, J. Kamioka, T. Otsuka, J. Yoneda, T. Nakajima, M. R. Delbecq, S. Amaha, G. Allison, T. Kodera, S. Oda, and S. Tarucha, "A fault-tolerant addressable spin qubit in a natural silicon quantum dot", Science Advances **2**, e1600694–e1600694 (2016).

[4] J. Yoneda, K. Takeda, T. Otsuka, T. Nakajima, M. R. Delbecq, G. Allison, T. Honda, T. Kodera, S. Oda, Y. Hoshi, N. Usami, K. M. Itoh, and S. Tarucha, "A quantum-dot spin qubit with coherence limited by charge noise and fidelity higher than 99.9%", Nature Nanotechnology **13**, 102–106 (2018).

[5] T. Cubaynes, M. R. Delbecq, M. C. Dartiailh, R. Assouly, M. M. Desjardins, L. C. Contamin, L. E. Bruhat, Z. Leghtas, F. Mallet, A. Cottet, and T. Kontos, "Highly coherent spin states in carbon nanotubes coupled to cavity photons", npj Quantum Information **5**, 47 (2019).

[6] M. M. Desjardins, L. C. Contamin, M. R. Delbecq, M. C. Dartiailh, L. E. Bruhat, T. Cubaynes, J. J. Viennot, F. Mallet, S. Rohart, A. Thiaville, A. Cottet, and T. Kontos, "Synthetic spin–orbit interaction for Majorana devices", Nature Materials **18**, 1060–1064 (2019).

[7] A. Abragam, *The Principles of Nuclear Magnetism* (Oxford University Press, 1961), p. 618.

[8] I. Žutić, J. Fabian, and S. Das Sarma, "Spintronics: Fundamentals and applications", Reviews of Modern Physics **76**, 323–410 (2004).

[9] F. H. L. Koppens, C. Buizert, K. J. Tielrooij, I. T. Vink, K. C. Nowack, T. Meunier, L. P. Kouwenhoven, and L. M. K. Vandersypen, "Driven coherent oscillations of a single electron spin in a quantum dot.", Nature **442**, 766–71 (2006).

[10] M. Veldhorst, J. C. C. Hwang, C. H. Yang, a. W. Leenstra, B. de Ronde, J. P. Dehollain, J. T. Muhonen, F. E. Hudson, K. M. Itoh, A. Morello, and a. S. Dzurak, "An addressable quantum dot qubit with fault-tolerant control-fidelity", Nature Nanotechnology **9**, 981–985 (2014).

[11] M. Veldhorst, C. H. Yang, J. C. C. Hwang, W. Huang, J. P. Dehollain, J. T. Muhonen, S. Simmons, A. Laucht, F. E. Hudson, K. M. Itoh, A. Morello, and A. S. Dzurak, "A two-qubit logic gate in silicon", Nature **526**, 410–414 (2015).

[12] L. Petit, H. G. J. Eenink, M. Russ, W. I. L. Lawrie, N. W. Hendrickx, S. G. J. Philips, J. S. Clarke, L. M. K. Vandersypen, and M. Veldhorst, "Universal quantum logic in hot silicon qubits", Nature **580**, 355–359 (2020).

[13] C. H. Yang, R. C. C. Leon, J. C. C. Hwang, A. Saraiva, T. Tanttu, W. Huang, J. Camirand Lemyre, K. W. Chan, K. Y. Tan, F. E. Hudson, K. M. Itoh, A. Morello, M. Pioro-Ladrière, A. Laucht, and A. S. Dzurak, "Operation of a silicon quantum processor unit cell above one kelvin", Nature **580**, 350–354 (2020).

[14] Y. Tokura, W. van der Wiel, T. Obata, and S. Tarucha, "Coherent Single Electron Spin Control in a Slanting Zeeman Field", Physical Review Letters **96**, 047202 (2006).

[15] M. Combescot, S.-Y. Shiau, and V. Voliotis, "Spin-orbit coupling: Atom versus semiconductor crystal", Physical Review B **99**, 245202 (2019).

[16] B. Braunecker, G. I. Japaridze, J. Klinovaja, and D. Loss, "Spin-selective Peierls transition in interacting one-dimensional conductors with spin-orbit interaction", Physical Review B **82**, 045127 (2010).

[17] L. C. Contamin, "Mise en évidence de textures de spin synthétiques par des mesures de transport et de champ microonde", PhD thesis (2019).

[18] M. Pioro-Ladrière, T. Obata, Y. Tokura, Y.-S. Shin, T. Kubo, K. Yoshida, T. Taniyama, and S. Tarucha, "Electrically driven single-electron spin resonance in a slanting Zeeman field", Nature Physics **4**, 776–779 (2008).

[19] J. Yoneda, T. Otsuka, T. Takakura, M. Pioro-Ladrière, R. Brunner, H. Lu, T. Nakajima, T. Obata, A. Noiri, C. J. Palmstrøm, A. C. Gossard, and S. Tarucha, "Robust micromagnet design for fast electrical manipulations of single spins in quantum dots", Applied Physics Express **8**, 084401 (2015).

[20] A. Noiri, J. Yoneda, T. Nakajima, T. Otsuka, M. R. Delbecq, K. Takeda, S. Amaha, G. Allison, A. Ludwig, A. D. Wieck, and S. Tarucha, "Coherent electron-spin-resonance manipulation of three individual spins in a triple quantum dot", Applied Physics Letters **108**, 153101 (2016).

[21] T. Ito, T. Otsuka, T. Nakajima, M. R. Delbecq, S. Amaha, J. Yoneda, K. Takeda, A. Noiri, G. Allison, A. Ludwig, A. D. Wieck, and S. Tarucha, "Four single-spin Rabi oscillations in a quadruple quantum dot", Applied Physics Letters **113**, 093102 (2018).

[22] A. Cottet and T. Kontos, "Spin Quantum Bit with Ferromagnetic Contacts for Circuit QED", Physical Review Letters **105**, 160502 (2010).

[23] X. Hu, Y.-x. Liu, and F. Nori, "Strong coupling of a spin qubit to a superconducting stripline cavity", Physical Review B **86**, 035314 (2012).

[24] J. J. Viennot, M. C. Dartiailh, A. Cottet, and T. Kontos, "Coherent coupling of a single spin to microwave cavity photons", Science **349**, 408–411 (2015).

[25] X. Mi, M. Benito, S. Putz, D. M. Zajac, J. M. Taylor, G. Burkard, and J. R. Petta, "A coherent spin–photon interface in silicon", Nature **555**, 599–603 (2018).

[26] N. Samkharadze, G. Zheng, N. Kalhor, D. Brousse, A. Sammak, U. C. Mendes, A. Blais, G. Scappucci, and L. M. K. Vandersypen, "Strong spin-photon coupling in silicon", Science **359**, 1123–1127 (2018).

[27] J. Viennot, "Charge and spin dynamics in a hybrid circuit quantum electrodynamics architecture", Theses (Ecole Normale Supérieure de Paris - ENS Paris, June 2014).

[28] M. Benito, X. Mi, J. M. Taylor, J. R. Petta, and G. Burkard, "Input-output theory for spin-photon coupling in Si double quantum dots", Physical Review B **96**, 235434 (2017).

[29] M. Benito, X. Croot, C. Adelsberger, S. Putz, X. Mi, J. R. Petta, and G. Burkard, "Electric-field control and noise protection of the flopping-mode spin qubit", Physical Review B **100**, 125430 (2019).

[30] S. Nadj-Perge, I. K. Drozdov, B. A. Bernevig, and A. Yazdani, "Proposal for realizing Majorana fermions in chains of magnetic atoms on a superconductor", Physical Review B - Condensed Matter and Materials Physics **88**, 1–5 (2013).

[31] J. Klinovaja, P. Stano, A. Yazdani, and D. Loss, "Topological Superconductivity and Majorana Fermions in RKKY Systems", Physical Review Letters **111**, 186805 (2013).

[32] F. Pientka, L. I. Glazman, and F. Von Oppen, "Topological superconducting phase in helical Shiba chains", Physical Review B - Condensed Matter and Materials Physics **88**, 1–13 (2013).

[33] B. Braunecker, P. Simon, and D. Loss, "Nuclear magnetism and electronic order in C13 nanotubes", Physical Review Letters **102**, 6–9 (2009).

[34] C.-H. Hsu, P. Stano, J. Klinovaja, and D. Loss, "Antiferromagnetic nuclear spin helix and topological superconductivity in ¡math¿ ¡mmultiscripts¿ ¡mtext¿C¡/mtext¿ ¡mprescripts/¿ ¡none/¿ ¡mn¿13¡/mn¿ ¡/mmultiscripts¿ ¡/math¿ nanotubes", Physical Review B **92**, 235435 (2015).

[35] J. Klinovaja, P. Stano, and D. Loss, "Transition from Fractional to Majorana Fermions in Rashba Nanowires", Physical Review Letters **109**, 236801 (2012).

[36] M. Kjaergaard, K. Wölms, and K. Flensberg, "Majorana fermions in superconducting nanowires without spin-orbit coupling", Physical Review B **85**, 020503 (2012).

[37] R. Egger and K. Flensberg, "Emerging Dirac and Majorana fermions for carbon nanotubes with proximity-induced pairing and spiral magnetic field", Physical Review B **85**, 235462 (2012).

[38] A. Matos-Abiague, J. Shabani, A. D. Kent, G. L. Fatin, B. Scharf, and I. Žutić, "Tunable magnetic textures: From Majorana bound states to braiding", Solid State Communications **262**, 1–6 (2017).

[39] C. Kloeffel, M. Trif, P. Stano, and D. Loss, "Circuit QED with hole-spin qubits in Ge/Si nanowire quantum dots", Physical Review B **88**, 241405 (2013).

[40] D. Loss and D. P. DiVincenzo, "Quantum computation with quantum dots", Physical Review A **57**, 120–126 (1998).

[41] J. M. Kikkawa and D. D. Awschalom, "Resonant spin amplification in n-type GaAs", Physical Review Letters **80**, 4313–4316 (1998).

[42] I. A. Merkulov, A. L. Efros, and M. Rosen, "Electron spin relaxation by nuclei in semiconductor quantum dots", Physical Review B **65**, 205309 (2002).

[43] A. V. Khaetskii, D. Loss, and L. Glazman, "Electron spin decoherence in quantum dots due to interaction with nuclei.", Physical review letters **88**, 186802 (2002).

[44] J. Schliemann, A. Khaetskii, and D. Loss, "Electron spin dynamics in quantum dots and related nanostructures due to hyperfine interaction with nuclei", en, Journal of Physics: Condensed Matter **15**, 26 (2003).

[45] J. Jackson, *Classical electrodynamics* (John Wiley & Sons, 1975).

[46] W. A. Coish and J. Baugh, "Nuclear spins in nanostructures", physica status solidi (b) **246**, 2203–2215 (2009).

[47] O. V. Yazyev, "Hyperfine Interactions in Graphene and Related Carbon Nanostructures", Nano Letters **8**, 1011–1015 (2008).

[48] D. V. Bulaev, B. Trauzettel, and D. Loss, "Spin-orbit interaction and anomalous spin relaxation in carbon nanotube quantum dots", Physical Review B **77**, 235301 (2008).

[49] S. I. Erlingsson and Y. V. Nazarov, "Hyperfine-mediated transitions between a Zeeman split doublet in GaAs quantum dots: The role of the internal field", Physical Review B **66**, 155327 (2002).

[50] L. C. Camenzind, L. Yu, P. Stano, J. D. Zimmerman, A. C. Gossard, D. Loss, and D. M. Zumbühl, "Hyperfine-phonon spin relaxation in a single-electron GaAs quantum dot", Nature Communications **9**, 1–6 (2018).

[51] N. Bloembergen, E. M. Purcell, and R. V. Pound, "Relaxation Effects in Nuclear Magnetic Resonance Absorption", Physical Review **73**, 679–712 (1948).

[52] H. Flentje, P.-A. Mortemousque, R. Thalineau, A. Ludwig, A. D. Wieck, C. Bäuerle, and T. Meunier, "Coherent long-distance displacement of individual electron spins", Nature Communications **8**, 501 (2017).

[53] R. Saito, G. Dresselhaus, and M. D. Dresselhaus, *Physical properties of carbon nanotubes* (Imperial College Press, 1998).

[54] A. Noiri, T. Nakajima, J. Yoneda, M. R. Delbecq, P. Stano, T. Otsuka, K. Takeda, S. Amaha, G. Allison, K. Kawasaki, Y. Kojima, A. Ludwig, A. D. Wieck, D. Loss, and S. Tarucha, "A fast quantum interface between different spin qubit encodings", Nature Communications **9**, 5066 (2018).

[55] B. Urbaszek, X. Marie, T. Amand, O. Krebs, P. Voisin, P. Maletinsky, A. Högele, and A. Imamoglu, "Nuclear spin physics in quantum dots: An optical investigation", Reviews of Modern Physics **85**, 79–133 (2013).

[56] D. Paget, G. Lampel, B. Sapoval, and V. I. Safarov, "Low field electron-nuclear spin coupling in gallium arsenide under optical pumping conditions", Physical Review B **15**, 5780–5796 (1977).

[57] P. Maletinsky, A. Badolato, and A. Imamoglu, "Dynamics of Quantum Dot Nuclear Spin Polarization Controlled by a Single Electron", Physical Review Letters **99**, 056804 (2007).

[58] M. C. Wang and G. E. Uhlenbeck, "On the Theory of the Brownian Motion II", Reviews of Modern Physics **17**, 323–342 (1945).

[59] A. G. Redfield, "Spatial Diffusion of Spin Energy", Physical Review **116**, 315–316 (1959).

[60] G. E. Uhlenbeck and L. S. Ornstein, "On the Theory of the Brownian Motion", Physical Review **36**, 823–841 (1930).

[61] J. R. Petta, A. C. Johnson, J. M. Taylor, E. a. Laird, A. Yacoby, M. D. Lukin, C. M. Marcus, M. P. Hanson, and A. C. Gossard, "Coherent manipulation of coupled electron spins in semiconductor quantum dots.", Science (New York, N.Y.) **309**, 2180–2184 (2005).

[62] R. Hanson, L. P. Kouwenhoven, J. R. Petta, S. Tarucha, and L. M. K. Vandersypen, "Spins in few-electron quantum dots", Reviews of Modern Physics **79**, 1217–1265 (2007).

[63] C. Barthel, J. Medford, H. Bluhm, A. Yacoby, C. M. Marcus, M. P. Hanson, and a. C. Gossard, "Relaxation and readout visibility of a singlet-triplet qubit in an Overhauser field gradient", Physical Review B **85**, 035306 (2012).

[64] A. Sergeevich, A. Chandran, J. Combes, S. D. Bartlett, and H. M. Wiseman, "Characterization of a qubit Hamiltonian using adaptive measurements in a fixed basis", Physical Review A **84**, 052315 (2011).

[65] M. D. Shulman, S. P. Harvey, J. M. Nichol, S. D. Bartlett, A. C. Doherty, V. Umansky, and A. Yacoby, "Suppressing qubit dephasing using real-time Hamiltonian estimation", Nature Communications **5**, 5156 (2014).

[66] D. Klauser, W. A. Coish, and D. Loss, "Nuclear spin dynamics and Zeno effect in quantum dots and defect centers", Phys. Rev. B **78**, 205301 (2008).

[67] J.-P. Bouchaud and A. Georges, "Anomalous diffusion in disordered media: Statistical mechanisms, models and physical applications", Phys. Rep. **195**, 127–293 (1990).

[68] R. Metzler and J. Klafter, "The random walk's guide to anomalous diffusion: a fractional dynamics approach", Phys. Rep. **339**, 1–77 (2000).

[69] Y. Li, N. Sinitsyn, D. L. Smith, D. Reuter, A. D. Wieck, D. R. Yakovlev, M. Bayer, and S. A. Crooker, "Intrinsic Spin Fluctuations Reveal the Dynamical Response Function of Holes Coupled to Nuclear Spin Baths in (In,Ga)As Quantum Dots", Phys. Rev. Lett. **108**, 186603 (2012).

[70] D. J. Reilly, J. M. Taylor, E. A. Laird, J. R. Petta, C. M. Marcus, M. P. Hanson, and A. C. Gossard, "Measurement of Temporal Correlations of the Overhauser Field in a Double Quantum Dot", Phys. Rev. Lett. **101**, 236803 (2008).

[71] J. Medford, A. Cywiński, C. Barthel, C. M. Marcus, M. P. Hanson, and A. C. Gossard, "Scaling of dynamical decoupling for spin qubits", Phys. Rev. Lett. **108**, 086802 (2012).

[72] F. K. Malinowski, F. Martins, Ł. Cywi ński, M. S. Rudner, P. D. Nissen, S. Fallahi, G. C. Gardner, M. J. Manfra, C. M. Marcus, and F. Kuemmeth, "Spectrum of the nuclear environment for gaas spin qubits", Phys. Rev. Lett. **118**, 177702 (2017).

[73] T. Nakajima, A. Noiri, J. Yoneda, M. R. Delbecq, P. Stano, T. Otsuka, K. Takeda, S. Amaha, G. Allison, K. Kawasaki, A. Ludwig, A. D. Wieck, D. Loss, and S. Tarucha, "Quantum non-demolition measurement of an electron spin qubit", Nature Nanotechnology **14**, 555–560 (2019).

[74] G. Ithier, E. Collin, P. Joyez, P. J. Meeson, D. Vion, D. Esteve, F. Chiarello, A. Shnirman, Y. Makhlin, J. Schriefl, and G. Schön, "Decoherence in a superconducting quantum bit circuit", Physical Review B **72**, 134519 (2005).

[75] A. G. Fowler, A. M. Stephens, and P. Groszkowski, "High-threshold universal quantum computation on the surface code", Physical Review A **80**, 052312 (2009).

[76] C. Barthel, M. Kjærgaard, J. Medford, M. Stopa, C. M. Marcus, M. P. Hanson, and A. C. Gossard, "Fast sensing of double-dot charge arrangement and spin state with a radio-frequency sensor quantum dot", Physical Review B **81**, 161308 (2010).

[77] J. Yoneda, T. Otsuka, T. Nakajima, T. Takakura, T. Obata, M. Pioro-Ladrière, H. Lu, C. J. Palmstrøm, A. C. Gossard, and S. Tarucha, "Fast Electrical Control of Single Electron Spins in Quantum Dots with Vanishing Influence from Nuclear Spins", Physical Review Letters **113**, 267601 (2014).

[78] J. T. Muhonen, A. Laucht, S. Simmons, J. P. Dehollain, R. Kalra, F. E. Hudson, S. Freer, K. M. Itoh, D. N. Jamieson, J. C. McCallum, A. S. Dzurak, and A. Morello, "Quantifying the quantum gate fidelity of single-atom spin qubits in silicon by randomized benchmarking", Journal of Physics: Condensed Matter **27**, 154205 (2015).

[79] D. K. Tuckett, S. D. Bartlett, S. T. Flammia, and B. J. Brown, "Fault-tolerant thresholds for the surface code in excess of 5% under biased noise", 1–6 (2019).

[80] F. Yan, S. Gustavsson, J. Bylander, X. Jin, F. Yoshihara, D. G. Cory, Y. Nakamura, T. P. Orlando, and W. D. Oliver, "Rotating-frame relaxation as a noise spectrum analyser of a superconducting qubit undergoing driven evolution", Nature Communications **4**, 2337 (2013).

[81] F. Yoshihara, Y. Nakamura, F. Yan, S. Gustavsson, J. Bylander, W. D. Oliver, and J.-S. Tsai, "Flux qubit noise spectroscopy using Rabi oscillations under strong driving conditions", Physical Review B **89**, 020503 (2014).

[82] D. Allan, "Statistics of atomic frequency standards", Proceedings of the IEEE **54**, 221–230 (1966).

[83] E. Kawakami, P. Scarlino, D. R. Ward, F. R. Braakman, D. E. Savage, M. G. Lagally, M. Friesen, S. N. Coppersmith, M. A. Eriksson, and L. M. K. Vandersypen, "Electrical control of a long-lived spin qubit in a Si/SiGe quantum dot", Nature Nanotechnology **9**, 666–670 (2014).

[84] F. Arute, K. Arya, R. Babbush, D. Bacon, J. C. Bardin, R. Barends, R. Biswas, S. Boixo, F. G. S. L. Brandao, D. A. Buell, B. Burkett, Y. Chen, Z. Chen, B. Chiaro, R. Collins, W. Courtney, A. Dunsworth, E. Farhi, B. Foxen, A. Fowler, C. Gidney, M. Giustina, R. Graff, K. Guerin, S. Habegger, M. P. Harrigan, M. J. Hartmann, A. Ho, M. Hoffmann, T. Huang, T. S. Humble, S. V. Isakov, E. Jeffrey, Z. Jiang, D. Kafri, K. Kechedzhi, J. Kelly, P. V. Klimov, S. Knysh, A. Korotkov, F. Kostritsa, D. Landhuis, M. Lindmark, E. Lucero, D. Lyakh, S. Mandrà, J. R. McClean, M. McEwen, A. Megrant, X. Mi, K. Michielsen, M. Mohseni, J. Mutus, O. Naaman, M. Neeley, C. Neill, M. Y. Niu, E. Ostby, A. Petukhov, J. C. Platt, C. Quintana, E. G. Rieffel, P. Roushan, N. C. Rubin, D. Sank, K. J. Satzinger, V. Smelyanskiy, K. J. Sung, M. D. Trevithick, A. Vainsencher, B. Villalonga, T. White, Z. J. Yao, P. Yeh, A. Zalcman, H. Neven, and J. M. Martinis, "Quantum supremacy using a programmable superconducting processor", Nature **574**, 505–510 (2019).

[85] Ł. Cywiński, R. M. Lutchyn, C. P. Nave, and S. Das Sarma, "How to enhance dephasing time in superconducting qubits", Physical Review B **77**, 174509 (2008).

[86] H. Bohuslavskyi, S. Barraud, M. Casse, V. Barrai, B. Bertrand, L. Hutin, F. Arnaud, P. Galy, M. Sanquer, S. De Franceschi, and M. Vinet, "28nm Fully-depleted SOI technology: Cryogenic control electronics for quantum computing", in 2017 silicon nanoelectronics workshop (snw), Vol. 2017-Janua (June 2017), pp. 143–144.

[87] R. Maurand, X. Jehl, D. Kotekar-Patil, A. Corna, H. Bohuslavskyi, R. Laviéville, L. Hutin, S. Barraud, M. Vinet, M. Sanquer, and S. De Franceschi, "A CMOS silicon spin qubit", Nature Communications **7**, 13575 (2016).

[88] E. A. Laird, F. Pei, and L. P. Kouwenhoven, "A valley–spin qubit in a carbon nanotube", Nature Nanotechnology **8**, 565–568 (2013).

[89] T. Pei, A. Pályi, M. Mergenthaler, N. Ares, A. Mavalankar, J. H. Warner, G. A. D. Briggs, and E. A. Laird, "Hyperfine and Spin-Orbit Coupling Effects on Decay of Spin-Valley States in a Carbon Nanotube", Physical Review Letters **118**, 177701 (2017).

[90] C. H. Pennington and V. A. Stenger, "Nuclear magnetic resonance of C_{60} and fulleride superconductors", Rev. Mod. Phys. **68**, 855–910 (1996).

[91] A. Wallraff, D. I. Schuster, A. Blais, L. Frunzio, J. Majer, S. Kumar, S. M. Girvin, and R. J. Schoelkopf, "Strong coupling of a single photon to a superconducting qubit using circuit quantum electrodynamics", Nature **431**, 162–167 (2004).

[92] A. Blais, R.-S. Huang, A. Wallraff, S. M. Girvin, and R. J. Schoelkopf, "Cavity quantum electrodynamics for superconducting electrical circuits: An architecture for quantum computation", Physical Review A **69**, 062320 (2004).

[93] P. Goy, J. M. Raimond, M. Gross, and S. Haroche, "Observation of Cavity-Enhanced Single-Atom Spontaneous Emission", Physical Review Letters **50**, 1903–1906 (1983).

[94] A. Cottet, M. C. Dartiailh, M. M. Desjardins, T. Cubaynes, L. C. Contamin, M. Delbecq, J. J. Viennot, L. E. Bruhat, B. Douçot, and T. Kontos, "Cavity QED with hybrid nanocircuits: from atomic-like physics to condensed matter phenomena", Journal of Physics: Condensed Matter **29**, 433002 (2017).

[95] G. Burkard, M. J. Gullans, X. Mi, and J. R. Petta, "Superconductor–semiconductor hybrid-circuit quantum electrodynamics", Nature Reviews Physics (2020) 10.1038/s42254-019-0135-2.

[96] F. Borjans, X. G. Croot, X. Mi, M. J. Gullans, and J. R. Petta, "Resonant microwave-mediated interactions between distant electron spins", Nature **577**, 195–198 (2020).

[97] A. J. Landig, J. V. Koski, P. Scarlino, U. C. Mendes, A. Blais, C. Reichl, W. Wegscheider, A. Wallraff, K. Ensslin, and T. Ihn, "Coherent spin–photon coupling using a resonant exchange qubit", Nature **560**, 179–184 (2018).

[98] Y. Kubo, F. R. Ong, P. Bertet, D. Vion, V. Jacques, D. Zheng, A. Dréau, J.-F. Roch, A. Auffeves, F. Jelezko, J. Wrachtrup, M. F. Barthe, P. Bergonzo, and D. Esteve, "Strong Coupling of a Spin Ensemble to a Superconducting Resonator", Physical Review Letters **105**, 140502 (2010).

[99] J. Medford, J. Beil, J. M. Taylor, S. D. Bartlett, a. C. Doherty, E. I. Rashba, D. P. Divincenzo, H. Lu, A. C. Gossard, and C. M. Marcus, "Self-consistent measurement and state tomography of an exchange-only spin qubit.", Nature nanotechnology **8**, 654–9 (2013).

[100] C. C. Wu, C. H. Liu, and Z. Zhong, "One-Step Direct Transfer of Pristine Single-Walled Carbon Nanotubes for Functional Nanoelectronics", Nano Letters **10**, 1032–1036 (2010).

[101] J. Waissman, M. Honig, S. Pecker, A. Benyamini, A. Hamo, and S. Ilani, "Realization of pristine and locally tunable one-dimensional electron systems in carbon nanotubes", Nature Nanotechnology **8**, 569–574 (2013).

[102] A. P. Higginbotham, F. Kuemmeth, M. P. Hanson, A. C. Gossard, and C. M. Marcus, "Coherent Operations and Screening in Multielectron Spin Qubits", Physical Review Letters **112**, 026801 (2014).

[103] J. J. Viennot, M. R. Delbecq, M. C. Dartiailh, A. Cottet, and T. Kontos, "Out-of-equilibrium charge dynamics in a hybrid circuit quantum electrodynamics architecture", Physical Review B **89**, 165404 (2014).

[104] L. E. Bruhat, T. Cubaynes, J. J. Viennot, M. C. Dartiailh, M. M. Desjardins, A. Cottet, and T. Kontos, "Circuit QED with a quantum-dot charge qubit dressed by Cooper pairs", Physical Review B **98**, 155313 (2018).

[105] W. A. Coish and D. Loss, "Hyperfine interaction in a quantum dot: Non-Markovian electron spin dynamics", Physical Review B **70**, 195340 (2004).

[106] C. Deng and X. Hu, "Analytical solution of electron spin decoherence through hyperfine interaction in a quantum dot", Physical Review B **73**, 241303 (2006).

[107] W. Yao, R.-B. Liu, and L. J. Sham, "Theory of electron spin decoherence by interacting nuclear spins in a quantum dot", Physical Review B **74**, 195301 (2006).

[108] A. Y. Kitaev, "Unpaired Majorana fermions in quantum wires", Physics-Uspekhi **44**, 131–136 (2001).

[109] E. Majorana, "Teoria simmetrica dell'elettrone e del positrone", Il Nuovo Cimento **14**, 171–184 (1937).

[110] C. Nayak, S. H. Simon, A. Stern, M. Freedman, and S. Das Sarma, "Non-Abelian anyons and topological quantum computation", Reviews of Modern Physics **80**, 1083–1159 (2008).

[111] D. A. Ivanov, "Non-abelian statistics of half-quantum vortices in p-wave superconductors", Phys. Rev. Lett. **86**, 268–271 (2001).

[112] G. Moore and N. Read, "Nonabelions in the fractional quantum hall effect", Nuclear Physics B **360**, 362–396 (1991).

[113] Y. Oreg, G. Refael, and F. von Oppen, "Helical Liquids and Majorana Bound States in Quantum Wires", Physical Review Letters **105**, 177002 (2010).

[114] R. M. Lutchyn, J. D. Sau, and S. Das Sarma, "Majorana Fermions and a Topological Phase Transition in Semiconductor-Superconductor Heterostructures", Physical Review Letters **105**, 077001 (2010).

[115] S. Nadj-Perge, I. K. Drozdov, J. Li, H. Chen, S. Jeon, J. Seo, A. H. MacDonald, B. A. Bernevig, and A. Yazdani, "Observation of Majorana fermions in ferromagnetic atomic chains on a superconductor", Science **346**, 602–607 (2014).

[116] R. Pawlak, M. Kisiel, J. Klinovaja, T. Meier, S. Kawai, T. Glatzel, D. Loss, and E. Meyer, "Probing atomic structure and Majorana wavefunctions in mono-atomic Fe chains on superconducting Pb surface", npj Quantum Information **2**, 16035 (2016).

[117] S. Jeon, Y. Xie, J. Li, Z. Wang, B. A. Bernevig, and A. Yazdani, "Distinguishing a Majorana zero mode using spin-resolved measurements", Science **358**, 772–776 (2017).

[118] B. Jäck, Y. Xie, J. Li, S. Jeon, B. A. Bernevig, and A. Yazdani, "Observation of a Majorana zero mode in a topologically protected edge channel", Science **364**, 1255–1259 (2019).

[119] G. C. Ménard, S. Guissart, C. Brun, R. T. Leriche, M. Trif, F. Debontridder, D. Demaille, D. Roditchev, P. Simon, and T. Cren, "Two-dimensional topological superconductivity in Pb/Co/Si(111)", Nature Communications **8**, 2040 (2017).

[120] N. Read and D. Green, "Paired states of fermions in two dimensions with breaking of parity and time-reversal symmetries and the fractional quantum Hall effect", Physical Review B **61**, 10267–10297 (2000).

[121] L. Fu and C. L. Kane, "Superconducting Proximity Effect and Majorana Fermions at the Surface of a Topological Insulator", Physical Review Letters **100**, 096407 (2008).

[122] M. Sato, Y. Takahashi, and S. Fujimoto, "Non-Abelian Topological Order in ¡math display="inline"¿ ¡mi¿s¡/mi¿ ¡/math¿ -Wave Superfluids of Ultracold Fermionic Atoms", Physical Review Letters **103**, 020401 (2009).

[123] J. D. Sau, R. M. Lutchyn, S. Tewari, and S. Das Sarma, "Generic New Platform for Topological Quantum Computation Using Semiconductor Heterostructures", Physical Review Letters **104**, 040502 (2010).

[124] J. Alicea, "Majorana fermions in a tunable semiconductor device", Physical Review B **81**, 125318 (2010).

[125] V. Mourik, K. Zuo, S. M. Frolov, S. R. Plissard, E. P. A. M. Bakkers, and L. P. Kouwenhoven, "Signatures of Majorana Fermions in Hybrid Superconductor-Semiconductor Nanowire Devices", Science **336**, 1003–1007 (2012).

[126] M. T. Deng, S. Vaitiekėnas, E. B. Hansen, J. Danon, M. Leijnse, K. Flensberg, J. Nygård, P. Krogstrup, and C. M. Marcus, "Majorana bound state in a coupled quantum-dot hybrid-nanowire system", Science **354**, 1557–1562 (2016).

[127] H. Zhang, C.-X. Liu, S. Gazibegovic, D. Xu, J. A. Logan, G. Wang, N. van Loo, J. D. S. Bommer, M. W. A. de Moor, D. Car, R. L. M. Op het Veld, P. J. van Veldhoven, S. Koelling, M. A. Verheijen, M. Pendharkar, D. J. Pennachio, B. Shojaei, J. S. Lee, C. J. Palmstrøm, E. P. A. M. Bakkers, S. D. Sarma, and L. P. Kouwenhoven, "Quantized Majorana conductance", Nature **556**, 74–79 (2018).

[128] H. J. Suominen, M. Kjaergaard, A. R. Hamilton, J. Shabani, C. J. Palmstrøm, C. M. Marcus, and F. Nichele, "Zero-Energy Modes from Coalescing Andreev States in a Two-Dimensional Semiconductor-Superconductor Hybrid Platform", Physical Review Letters **119**, 176805 (2017).

[129] R. M. Lutchyn, E. P. A. M. Bakkers, L. P. Kouwenhoven, P. Krogstrup, C. M. Marcus, and Y. Oreg, "Majorana zero modes in superconductor–semiconductor heterostructures", Nature Reviews Materials **3**, 52–68 (2018).

[130] A. P. Higginbotham, S. M. Albrecht, G. Kiršanskas, W. Chang, F. Kuemmeth, P. Krogstrup, T. S. Jespersen, J. Nygård, K. Flensberg, and C. M. Marcus, "Parity lifetime of bound states in a proximitized semiconductor nanowire", Nature Physics, 1–6 (2015).

[131] D. Aasen, M. Hell, R. V. Mishmash, A. Higginbotham, J. Danon, M. Leijnse, T. S. Jespersen, J. A. Folk, C. M. Marcus, K. Flensberg, and J. Alicea, "Milestones Toward Majorana-Based Quantum Computing", Physical Review X **6**, 031016 (2016).

[132] S. Vijay and L. Fu, "Teleportation-based quantum information processing with Majorana zero modes", Physical Review B **94**, 235446 (2016).

[133] J. Liu, A. C. Potter, K. T. Law, and P. A. Lee, "Zero-Bias Peaks in the Tunneling Conductance of Spin-Orbit-Coupled Superconducting Wires with and without Majorana End-States", Physical Review Letters **109**, 267002 (2012).

[134] E. J. H. Lee, X. Jiang, R. Aguado, G. Katsaros, C. M. Lieber, and S. De Franceschi, "Zero-Bias Anomaly in a Nanowire Quantum Dot Coupled to Superconductors", Physical Review Letters **109**, 186802 (2012).

[135] D. Rainis, L. Trifunovic, J. Klinovaja, and D. Loss, "Towards a realistic transport modeling in a superconducting nanowire with Majorana fermions", Physical Review B **87**, 024515 (2013).

[136] M. W. A. de Moor, J. D. S. Bommer, D. Xu, G. W. Winkler, A. E. Antipov, A. Bargerbos, G. Wang, N. van Loo, R. L. M. Op het Veld, S. Gazibegovic, D. Car, J. A. Logan, M. Pendharkar, J. S. Lee, E. P. A. M Bakkers, C. J. Palmstrøm, R. M. Lutchyn, L. P. Kouwenhoven, and H. Zhang, "Electric field tunable superconductor-semiconductor coupling in Majorana nanowires", New Journal of Physics **20**, 103049 (2018).

[137] C. Moore, C. Zeng, T. D. Stanescu, and S. Tewari, "Quantized zero-bias conductance plateau in semiconductor-superconductor heterostructures without topological Majorana zero modes", Physical Review B **98**, 155314 (2018).

[138] P. Yu, J. Chen, M. Gomanko, G. Badawy, E. P. A. M. Bakkers, K. Zuo, V. Mourik, and S. M. Frolov, "Non-Majorana states yield nearly quantized conductance in superconductor-semiconductor nanowire devices", 1–20 (2020).

[139] J. Chen, B. D. Woods, P. Yu, M. Hocevar, D. Car, S. R. Plissard, E. P. A. M. Bakkers, T. D. Stanescu, and S. M. Frolov, "Ubiquitous Non-Majorana Zero-Bias Conductance Peaks in Nanowire Devices", Physical Review Letters **123**, 107703 (2019).

[140] B. D. Woods, J. Chen, S. M. Frolov, and T. D. Stanescu, "Zero-energy pinning of topologically trivial bound states in multiband semiconductor-superconductor nanowires", Physical Review B **100**, 125407 (2019).

[141] H. Pan and S. D. Sarma, "Zero-bias conductance peaks in Majorana nanowires: the good, the bad, and the ugly", 1–32 (2019).

[142] H. Pan, W. S. Cole, J. D. Sau, and S. Das Sarma, "Generic quantized zero-bias conductance peaks in superconductor-semiconductor hybrid structures", Physical Review B **101**, 1–6 (2020).

[143] M. Cheng, R. M. Lutchyn, V. Galitski, and S. Das Sarma, "Splitting of Majorana-Fermion Modes due to Intervortex Tunneling in a p_x+ip_y Superconductor", Physical Review Letters **103**, 107001 (2009).

[144] S. Das Sarma, J. D. Sau, and T. D. Stanescu, "Splitting of the zero-bias conductance peak as smoking gun evidence for the existence of the Majorana mode in a superconductor-semiconductor nanowire", Physical Review B **86**, 220506 (2012).

[145] C.-H. Lin, J. D. Sau, and S. Das Sarma, "Zero-bias conductance peak in Majorana wires made of semiconductor/superconductor hybrid structures", Physical Review B **86**, 224511 (2012).

[146] S. M. Albrecht, A. P. Higginbotham, M. Madsen, F. Kuemmeth, T. S. Jespersen, J. Nygård, P. Krogstrup, and C. M. Marcus, "Exponential protection of zero modes in Majorana islands", Nature **531**, 206–209 (2016).

[147] S. M. Albrecht, E. B. Hansen, A. P. Higginbotham, F. Kuemmeth, T. S. Jespersen, J. Nygård, P. Krogstrup, J. Danon, K. Flensberg, and C. M. Marcus, "Transport Signatures of Quasiparticle Poisoning in a Majorana Island", Physical Review Letters **118**, 1–6 (2017).

[148] D. Sherman, J. S. Yodh, S. M. Albrecht, J. Nygård, P. Krogstrup, and C. M. Marcus, "Normal, superconducting and topological regimes of hybrid double quantum dots", Nature Nanotechnology **12**, 212–217 (2017).

[149] E. C. O'Farrell, A. C. Drachmann, M. Hell, A. Fornieri, A. M. Whiticar, E. B. Hansen, S. Gronin, G. C. Gardner, C. Thomas, M. J. Manfra, K. Flensberg, C. M. Marcus, and F. Nichele, "Hybridization of Subgap States in One-Dimensional Superconductor-Semiconductor Coulomb Islands", Physical Review Letters **121**, 256803 (2018).

[150] J. Shen, S. Heedt, F. Borsoi, B. van Heck, S. Gazibegovic, R. L. M. Op het Veld, D. Car, J. A. Logan, M. Pendharkar, S. J. J. Ramakers, G. Wang, D. Xu, D. Bouman, A. Geresdi, C. J. Palmstrøm, E. P. A. M. Bakkers, and L. P. Kouwenhoven, "Parity transitions in the superconducting ground state of hybrid InSb–Al Coulomb islands", Nature Communications **9**, 4801 (2018).

[151] S. Vaitiekėnas, A. M. Whiticar, M.-T. Deng, F. Krizek, J. E. Sestoft, C. J. Palmstrøm, S. Marti-Sanchez, J. Arbiol, P. Krogstrup, L. Casparis, and C. M. Marcus, "Selective-Area-Grown Semiconductor-Superconductor Hybrids: A Basis for Topological Networks", Physical Review Letters **121**, 147701 (2018).

[152] Z. Cao, H. Zhang, H.-F. Lü, W.-X. He, H.-Z. Lu, and X. C. Xie, "Decays of Majorana or Andreev Oscillations Induced by Steplike Spin-Orbit Coupling", Physical Review Letters **122**, 147701 (2019).

[153] G. Sharma, C. Zeng, T. D. Stanescu, and S. Tewari, "Majorana versus Andreev bound state energy oscillations in a 1D semiconductor-superconductor heterostructure", **175005**, 1–12 (2020).

[154] C. Reeg, D. Loss, and J. Klinovaja, "Metallization of a Rashba wire by a superconducting layer in the strong-proximity regime", Physical Review B **97**, 165425 (2018).

[155] B. D. Woods, T. D. Stanescu, and S. Das Sarma, "Effective theory approach to the Schrödinger-Poisson problem in semiconductor Majorana devices", Physical Review B **98**, 035428 (2018).

[156] A. E. G. Mikkelsen, P. Kotetes, P. Krogstrup, and K. Flensberg, "Hybridization at Superconductor-Semiconductor Interfaces", Physical Review X **8**, 031040 (2018).

[157] A. E. Antipov, A. Bargerbos, G. W. Winkler, B. Bauer, E. Rossi, and R. M. Lutchyn, "Effects of Gate-Induced Electric Fields on Semiconductor Majorana Nanowires", Physical Review X **8**, 031041 (2018).

[158] O. Dmytruk, D. Chevallier, D. Loss, and J. Klinovaja, "Renormalization of the quantum dot g -factor in superconducting Rashba nanowires", Physical Review B **98**, 1–12 (2018).

[159] C. Jünger, R. Delagrange, D. Chevallier, S. Lehmann, K. A. Dick, C. Thelander, J. Klinovaja, D. Loss, A. Baumgartner, and C. Schönenberger, "Magnetic field independent sub-gap states in hybrid Rashba nanowires", 1–8 (2020).

[160] E. A. Laird, F. Kuemmeth, G. A. Steele, K. Grove-Rasmussen, J. Nygård, K. Flensberg, and L. P. Kouwenhoven, "Quantum transport in carbon nanotubes", Reviews of Modern Physics **87**, 703–764 (2015).

[161] G. Steele, F. Pei, E. Laird, J. Jol, H. Meerwaldt, and L. Kouwenhoven, "Large spin-orbit coupling in carbon nanotubes", Nature Communications **4**, 1573 (2013).

[162] T. Yokoyama, M. Eto, and Y. V. Nazarov, "Josephson Current through Semiconductor Nanowire with Spin–Orbit Interaction in Magnetic Field", Journal of the Physical Society of Japan **82**, 054703 (2013).

[163] J. Klinovaja and D. Loss, "Giant Spin-Orbit Interaction Due to Rotating Magnetic Fields in Graphene Nanoribbons", Physical Review X **3**, 011008 (2013).

[164] Z. Su, A. Zarassi, J.-F. Hsu, P. San-Jose, E. Prada, R. Aguado, E. J. H. Lee, S. Gazibegovic, R. L. M. Op het Veld, D. Car, S. R. Plissard, M. Hocevar, M. Pendharkar, J. S. Lee, J. A. Logan, C. J. Palmstrøm, E. P. A. M. Bakkers, and S. M. Frolov, "Mirage Andreev Spectra Generated by Mesoscopic Leads in Nanowire Quantum Dots", Physical Review Letters **121**, 127705 (2018).

[165] J. Kammhuber, M. C. Cassidy, F. Pei, M. P. Nowak, A. Vuik, Ö. Gül, D. Car, S. R. Plissard, E. P. A. M. Bakkers, M. Wimmer, and L. P. Kouwenhoven, "Conductance through a helical state in an Indium antimonide nanowire", Nature Communications **8**, 478 (2017).

[166] J. Sun, R. S. Deacon, R. Wang, J. Yao, C. M. Lieber, and K. Ishibashi, "Helical Hole State in Multiple Conduction Modes in Ge/Si Core/Shell Nanowire", Nano Letters **18**, 6144–6149 (2018).

[167] A. Cottet, T. Kontos, and B. Douçot, "Squeezing light with Majorana fermions", Physical Review B **88**, 195415 (2013).

[168] P. Virtanen and P. Recher, "Microwave spectroscopy of Josephson junctions in topological superconductors", Physical Review B - Condensed Matter and Materials Physics **88**, 1–8 (2013).

[169] C. Müller, J. Bourassa, and A. Blais, "Detection and manipulation of Majorana fermions in circuit QED", Physical Review B **88**, 235401 (2013).

[170] M. C. Dartiailh, T. Kontos, B. Douçot, and A. Cottet, "Direct Cavity Detection of Majorana Pairs", Physical Review Letters **118**, 126803 (2017).

[171] J. I. Väyrynen, G. Rastelli, W. Belzig, and L. I. Glazman, "Microwave signatures of Majorana states in a topological Josephson junction", Physical Review B **92**, 134508 (2015).

[172] G. L. Fatin, A. Matos-Abiague, B. Scharf, and I. Žutić, "Wireless Majorana Bound States: From Magnetic Tunability to Braiding", Physical Review Letters **117**, 077002 (2016).

[173] M. Hays, G. de Lange, K. Serniak, D. J. van Woerkom, D. Bouman, P. Krogstrup, J. Nygård, A. Geresdi, and M. H. Devoret, "Direct Microwave Measurement of Andreev-Bound-State Dynamics in a Semiconductor-Nanowire Josephson Junction", Physical Review Letters **121**, 047001 (2018).

[174] N. Didier, J. Bourassa, and A. Blais, "Fast Quantum Nondemolition Readout by Parametric Modulation of Longitudinal Qubit-Oscillator Interaction", Physical Review Letters **115**, 203601 (2015).

[175] N. Lambert, M. Cirio, M. Delbecq, G. Allison, M. Marx, S. Tarucha, and F. Nori, "Amplified and tunable transverse and longitudinal spin-photon coupling in hybrid circuit-QED", Physical Review B **97**, 125429 (2018).

[176] P. Bonderson, M. Freedman, and C. Nayak, "Measurement-Only Topological Quantum Computation", Physical Review Letters **101**, 010501 (2008).

[177] S. De Franceschi, L. Kouwenhoven, C. Schönenberger, and W. Wernsdorfer, "Hybrid superconductor–quantum dot devices", Nature Nanotechnology **5**, 703–711 (2010).

[178] J.-D. Pillet, C. H. L. Quay, P. Morfin, C. Bena, A. L. Yeyati, and P. Joyez, "Andreev bound states in supercurrent-carrying carbon nanotubes revealed", Nature Physics **6**, 965–969 (2010).

[179] E. J. H. Lee, X. Jiang, M. Houzet, R. Aguado, C. M. Lieber, and S. De Franceschi, "Spin-resolved Andreev levels and parity crossings in hybrid superconductor–semiconductor nanostructures", Nature Nanotechnology **9**, 79–84 (2014).

[180] A. Kumar, M. Gaim, D. Steininger, A. L. Yeyati, A. Martín-Rodero, A. K. Hüttel, and C. Strunk, "Temperature dependence of Andreev spectra in a superconducting carbon nanotube quantum dot", Physical Review B **89**, 075428 (2014).

[181] J. Gramich, A. Baumgartner, and C. Schönenberger, "Resonant and Inelastic Andreev Tunneling Observed on a Carbon Nanotube Quantum Dot", Physical Review Letters **115**, 216801 (2015).

[182] J. Gramich, A. Baumgartner, and C. Schönenberger, "Andreev bound states probed in three-terminal quantum dots", Physical Review B **96**, 195418 (2017).

[183] A. Murani, B. Dassonneville, A. Kasumov, J. Basset, M. Ferrier, R. Deblock, S. Guéron, and H. Bouchiat, "Microwave Signature of Topological Andreev level Crossings in a Bismuth-based Josephson Junction", Physical Review Letters **122**, 076802 (2019).